Paula Martínez Pérez

Development and optimisation of experimental biosensing protocols using porous optical transducers

Thesis submitted for the degree of Philosophiae Doctor

Supervisors:

Jaime García Rupérez

Biophotonics Group

Nanophotonics Technology Center of Valencia

Javier Martí Sendra

Nanophotonics Technology Center of Valencia

Tutor:

María José Bañuls Polo

Universitat Politècnica de València

Department of Chemistry

July , 2021

Acknowledgements

I would not be here writing this PhD Thesis without the support of all the people who have walked next to me for four years.

First of all, I would like to deeply thank my supervisors, Professor Javier Martí Sendra and Dr Jaime García Rupérez, as well as my academic tutor Dr Mª José Bañuls Polo, for the opportunity they gave me to get involved in the world of biophotonics and biosensors. Specially to Jaime, who guided me along this way and supported me whenever I needed. Thank you for all the opportunities you gave me to gain experience and experiences in this scientific and academic world.

I would also like to thank all the wonderful people I found at NTC. In particular, the Biophotonics group members for making things easier: Ángela, Raffaele, Xisco, Salva, Antonio, Luis, David, Jad and Maribel. I would like to extend my gratitude to those that shared with me every day and made me feel at home: Kike, Miguel, Giuseppe, Gustavo, Javi, Manel, Fran, Jose, Laura, Yoannet, Evelyn, Roberto, Javi, Jose, Dora, Cristina, Juan, Sergio, Álex, Jaime... And special mention to David and Carles, simply thanks for becoming my friends.

One of the most exciting experiences during these four years was my stay at INL. Thanks to Dr Martín López-García for giving me the opportunity of being part of NAPS group and your great hospitality, which can be also extended to Johannes, Miguel and Will. Thank you all for teaching me so many things in such a fun way. I would also like to thank Dr Laura Rodríguez Lorenzo for sharing with me her knowledge. And of course, I cannot forget Rafa, Bejoys, Fernando and Joanna. Thanks for all the laughs and moments we shared despite Covid restrictions, making it so hard for me leaving Braga. Atè breve!

Last but not least, thanks to my mother and my sister for your support always. This would not have been possible without you. And you, David, thanks for staying next to me in this adventure from minute zero.

Contents

Abstract

Biosensors are analytical devices with application in diverse fields and with several advantages relative to other conventional methods, such as the use of small volumes of sample and reagents, their sensitivity and their fast response, without the need of the sample pretreatment, expensive equipments or specialised technicians. Nevertheless, this is a relatively new research field in which there is a long way to go yet.

This doctoral Thesis aims at doing its bit to this field of knowledge by studying the potential of different porous materials as transducers for the development of real-time and label-free optical biosensors. The proposed materials range from those artificially synthesised, such as porous silicon (pSi), polymeric nanofibres (NFs) or commercial polymeric membranes, to natural materials with photonic properties that had not been exploited for sensing yet, such as biosilica exoskeletons of diatoms. All of them have in common its simple production, avoiding expensive and laborious nanofabrication processes. For their study, their optical response will be analysed and, in those cases in which such optical response allows performing detection experiments, strategies for their biofunctionalisation and their implementation in biosensing experiments will be developed as well.

Regarding pSi and NFs, the fabrication parameters were optimised to get a suitable optical response for their interrogation. Afterwards, their surface functionalisation was carried out by covalent and non-covalent methods, as well as different bioreceptors (DNA aptamers and antibodies), to study their potential and their constraints as biosensors. Concerning commercial membranes and the biosilica exoskeleton of diatoms, their optical response was characterised and refractive index sensing experiments were carried out to study their sensitivity. Additionally, a biofunctionalisation method for the surface of the diatoms exoskeleton was developed based on the use of cationic polyelectrolytes.

As a result, it was demonstrated the potential of NFs for the development of biosensors, as well as the potential of commercial membranes for developing sensors for an application that does not require a high sensitivity but a low cost. Furthermore, the great potential of biosilica exoskeleton of diatoms for the development of sensors based on their optical response has been revealed. By contrast, the constraints found in the development of pSi illustrate the importance of an accurate study and optimisation of porous materials structure before using them for (bio)sensing.

Resumen

Los biosensores son dispositivos analíticos con aplicabilidad en diferentes campos y con numerosas ventajas frente a otros métodos analíticos convencionales, como son el uso de pequeños volúmenes de muestra y reactivos, su sensibilidad y su rápida respuesta, sin necesidad de pretratamiento de la muestra, equipos caros o personal especializado. Sin embargo, se trata de un campo de investigación relativamente nuevo en el que todavía queda mucho camino por andar.

Esta Tesis doctoral pretende aportar un granito de arena a este campo de conocimiento mediante el estudio del potencial de diferentes materiales porosos como transductores para el desarrollo de biosensores ópticos con respuesta en tiempo real y sin marcajes. Los materiales propuestos van desde aquellos artificialmente sintetizados, como silicio poroso (SiP), nanofibras (NFs) poliméricas o membranas poliméricas comerciales, hasta materiales naturales con propiedades fotónicas que todavía no habían sido explotadas para el sensado, como son los exoesqueletos de biosílice de diatomeas. Todos ellos tienen en común la simplicidad en su obtención, evitando costosos y laboriosos procesos de nanofabricación. Para su estudio, se analizará su respuesta óptica y, en aquellos casos en los que ésta permita llevar a cabo experimentos de detección, se desarrollarán estrategias para su biofuncionalización y su implementación en experimentos de biosensado.

En el caso del SiP y las NFs se han optimizado los parámetros de fabricación para obtener una respuesta óptica adecuada que permita su interrogación. A continuación, se ha llevado a cabo su biofuncionalización empleando métodos covalentes y no covalentes, así como diferentes bioreceptores (aptámeros de ADN y anticuerpos) para estudiar su potencial y sus limitaciones como biosensores. En el caso de las membranas comerciales y el exoesqueleto de sílice de diatomeas, se ha caracterizado su respuesta óptica y se han llevado a cabo experimentos de sensado de índice de refracción para estudiar su sensibilidad. Así mismo, se ha desarrollado un método de funcionalización de la superficie del exoesqueleto de diatomeas basado en el uso de polielectrolitos catiónicos.

Como resultado, se ha demostrado el potencial tanto de NFs para el desarrollo de biosensores, como el de membranas comerciales para sensores cuya aplicación no requiera una elevada sensibilidad pero sí un bajo coste. Además, se ha puesto de manifiesto el gran potencial del exoesqueleto de diatomeas para el desarrollo de sensores basados en su respuesta óptica. Por el contrario, las limitaciones encontradas en el desarrollo de biosensores basados en SiP han evidenciado la necesidad de un estudio riguroso y la optimización de la estructura de materiales porosos previamente a ser usados en (bio)sensado.

Resum

Els biosensors són dispositius analítics amb aplicabilitat en diferents camps i amb nombrosos avantatges enfront d'altres mètodes analítics convencionals, com són l'ús de xicotets volums de mostra i reactius, la seua sensibilitat i la seua ràpida resposta, sense necessitat de pretractament de la mostra, equips cars o personal especialitzat. No obstant això, es tracta d'un camp d'investigació relativament nou en el qual encara queda molt camí per fer.

Aquesta Tesi doctoral pretén aportar el seu òbol a aquest camp de coneixement mitjançant l'estudi del potencial de diferents materials porosos com a transductors per al desenvolupament de biosensors òptics amb resposta en temps real i sense marcatges. Els materials proposats van des d'aquells artificialment sintetitzats, com a silici porós (SiP), nanofibras (NFs) polimèriques o membranes polimèriques comercials, fins a materials naturals amb propietats fotòniques que encara no havien sigut explotades per al sensat, com són els exoesquelets de biosílice de diatomees. Tots ells tenen en comú la simplicitat en la seua obtenció, evitant costosos i laboriosos processos de nanofabricació. Per al seu estudi, s'analitzarà la seua resposta òptica i, en aquells casos en els quals aquesta permeta dur a terme experiments de detecció, es desenvoluparan estratègies per a la seua biofuncionalització i la seua implementació en experiments de biosensat.

En el cas del SiP i les NFs s'han optimitzat els paràmetres de fabricació per a obtenir una resposta òptica adequada que permeta la seua interrogació. A continuació, s'ha dut a terme la seua biofuncionalització emprant mètodes covalents i no covalents, així com diferents bioreceptors (aptàmers d'ADN i anticossos) per a estudiar el seu potencial i les seues limitacions com a biosensors. En el cas de les membranes comercials i l'exoesquelet de sílice de diatomees, s'ha caracteritzat la seua resposta òptica i s'han dut a terme experiments de sensat d'índex de refracció per a estudiar la seua sensibilitat. Així mateix, s'ha desenvolupat un mètode de funcionalització de la superfície de l'exoesquelet de diatomees basat en l'ús de polielectròlits catiònics.

Com a resultat, s'ha demostrat el potencial tant de NFs per al desenvolupament de biosensors, com el de membranes comercials per a sensors amb una aplicació que no requerisca una elevada sensibilitat però sí un baix cost. A més, s'ha posat de manifest el gran potencial de l'exoesquelet de diatomees per al desenvolupament de sensors basats en la seua resposta òptica. Per contra, les limitacions trobades en el desenvolupament de biosensors basats en SiP han evidenciat la necessitat d'un estudi rigorós i l'optimització de l'estructura dels materials porosos prèviament a ser usats en (bio)sensat.

Acronyms

αBSA ..... Anti-BSA antibody

APTES ..... (3-aminopropyl)triethoxysilane

ATR ..... Attenuated total reflection

BSA ..... Bovine serum albumin

CBRN ..... Chemical, biological, radiological and nuclear

DI ..... Deionised water

DLS ..... Dynamic Light Scattering

DMF ..... Dimethyl formamide

DMSO ..... Dimethyl sulfoxide

EOT ..... Effective optical thickness

Fab ..... Antigen binding region

Fc ..... Constant fragment

FESEM ..... Field emission scanning electron microscope

FFT ..... Fast Fourier transform

FP ..... Fabry-Pérot

FTIR ..... Fourier transform infrared

HF ..... Hydrofluoric acid

IPA ..... Isopropyl alcohol

LOD ..... Limit of detection

MIR ..... Mid-infrared

NFs ..... Nanofibres

NHS ..... N-hydroxysuccinimide

NIR ..... Near-infrared

PA6 ..... Polyamide 6

PAH ..... Poly(allylamine hydrochloride)

PBG ..... Photonic bandgap

PBS ..... Phosphate Buffer Saline

PDDA ..... Poly(diallyldimethylammonium chloride)

PhC ..... Photonic crystal

PMMA ..... Polymethylmethacrylate

pSi ..... Porous silicon

SEM ..... Scanning electron microscope

SERS ..... Surface-enhanced Raman spectroscopy

SNR ..... Signal-to-noise-ratio

sPhC ..... Slab photonic crystal

TBA ..... Thrombin binding aptamer

TEM ..... Track-etched membrane

Chapter 1

Introduction

1.1 Biosensors

Biosensors are compact analytical devices that allow the selective and specific detection and/or quantification of a certain molecule or element of interest, referred as analyte, by means of biological recognition events. For such aim, biosensors have a relatively easy structure composed of three main elements: the bioreceptors, the transducer and the signal processing system (see Figure 1.1). Bioreceptors provide the specificity and selectivity of the biosensor, and thus, condition the final application. This is due to the capability of some biomolecules to specifically and selectively recognise and interact with other molecules or particles. Such interaction results in the formation of a complex (in affinity biosensors) or a product (in metabolic or catalytic biosensors) that provokes a physicochemical change that the transducer, in contact with the bioreceptors, can detect and transform into an easily measurable signal by the signal processor [1].

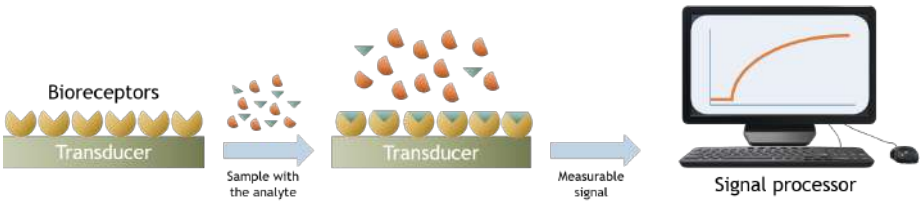

Figure 1.1. Scheme of a biosensor system consisting of a transducer with the bioreceptors and a signal processor. When a sample containing the analyte to detect is in contact with the biosensor, bioreceptors specifically and selectively bind the analyte molecules. This interaction is transformed into a measurable signal by the transducer that can be translated into intelligible data by a signal processor.

The main aim of biosensors research is overcoming the main limitations of traditional analytical methods requiring expensive reagents, time-consuming sample pre-treatment, expensive equipment and highly-qualified technicians. Biosensors aim at being more sensitive, cost-effective, rapid, easy to operate and portable to perform the analysis in situ. Eventually, the miniaturisation of biosensors for the development of simple, quick and affordable point-of-care (POC) testing devices is pursued. This sort of device is a portable "sample-in-answer-out" system that avoids complex laboratory equipment and allow multiplexing –the simultaneous detection of several analytes at the same time–

emulating traditional analytical instruments. Such ambitious goal requires technologies and knowledge from different fields such as physics, chemistry and biology, what makes biosensors development a highly multidisciplinary field. Nevertheless, this is a newly-born field and most of the already developed biosensors still require expensive equipment and allow only the detection of a single analyte.

It was in 1954 when the first biosensor was developed by Leland C. Clark: an oxygen electrode for oxygen detection [2]. This breakthrough paved the path for his following development, together with Champ Lyons: the first amperometric enzyme electrode for the detection of glucose in 1962 [3]. Since then, the evolution of biosensors skyrocketed and the first commercial glucose biosensor, developed by Yellow Spring Instruments (YSI), was available in 1975 [4]. Therefore, biosensors research is a relatively new field. However, in less than 50 years since the appearance of the first commercial biosensor a great progress has been made (see Figure 1.2). Initially the main application field of biosensors was medicine. Soon the potential of such devices was spotted and new application fields were explored. In food safety and agriculture, a field with a huge impact in both the economy and health of society, different biosensors for the tracking of foodborne hazards from farm to fork have been developed. Different microorganisms, pesticides, drugs, metals or allergens, among others, have been the analytes to detect by this sort of device [5]. Biosensors also raised expectations for bioterrorism applications in which a rapid, specific and sensitive response against unexpected attacks that can threaten public health is required [6]. Finally, another important application field of biosensors is environmental monitoring, also directly related to public health, for the detection of pollutants, pathogens and toxic compounds [7]. To create such a vast and diverse number of biosensors to date, different types of bioreceptors [4] and transducers have been employed.

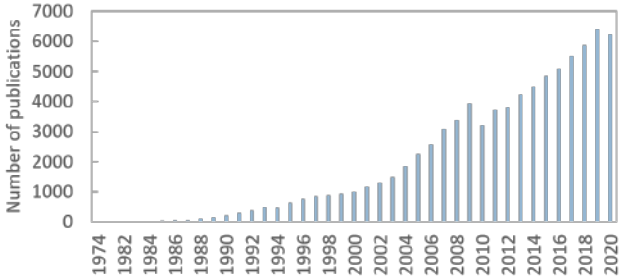

Figure 1.2. Evolution of the number of publications where "biosensor" term appears. Data provided by Web of Science by searching keyword "biosensor" in the topic.

The suitability of a biosensor for any of these applications is defined by a set of parameters [1, 8]. As previously explained, a biosensor must be able to detect undoubtedly the presence of an analyte in a sample in which other different

molecules or particles can be found and interfere. The ability to do it is known as selectivity and biosensors must demonstrate they are selective. Additionally, since the concentration of the analytes is usually minimal in most application fields, it is also important knowing the minimum concentration of the target analyte that the biosensor can detect with an acceptable signal-to-noise ratio, i.e. the limit of detection (LOD), and the minimum concentration of the target analyte that can be accurately and precisely quantified, i.e. the limit of quantification (LOQ). It is also important knowing the linearity of the biosensor, the range of analyte concentrations in which the biosensor shows a linear response with the concentration, and the minimum change of the signal per unit of concentration, i.e. the sensitivity. The latter is tightly related to the resolution of the biosensor, that is the minimum concentration change that can be detected. Moreover, the recognition must be immune to environmental changes whilst performing a detection assay, that is showing a good stability, and the response to a certain analyte concentration must be equal in all equally-fabricated biosensors, that is showing a high reproducibility.

Another important parameter is the response time, which defines the time required to achieve a constant response of the biosensor when a certain analyte concentration is flowed. It depends on the analyte concentration and the physicochemical basis of the biorecognition system employed. Two parameters related to the response time can be distinguished: steady state, the time employed to reach 95% of the steady state response, and transient response time, the first derivative of the response of the biosensor to reach its maximum.

1.1.1 Bioreceptors

Since the development of the first biosensor, different biomolecules were proposed as bioreceptors (see Figure 1.6).

Enzymes were the first bioreceptors to be proposed. They are proteins able to specifically bind a substrate and catalyse a chemical reaction to give rise to a product. For the development of a biosensor, both the enzyme-substrate biorecognition or the product formation can be monitored, being the latter specially interesting, since the product formation is a progressive process that can amplify the biosensor response. An advantage of using enzymes in biosensors is that after the reaction, the enzyme is not consumed, being ready for a new biosensing assay and allowing the biosensor to be reused. However, the adhesion of enzymes to the transducer can reduce their activity, conditioning the biosensor performance [9]. In recent years, nanotechnology has led to the development of artificial enzymes known as nanozymes. They can be metal and metal oxide nanoparticles, metal nanoclusters, dots, nanotubes, nanowires and metal-organic frameworks. Regarding their features, if compared with natural enzymes, nanozymes show outstanding catalytic activity at a lower production cost, a higher robustness and self-life and allow their easy modification [10].

After enzymes, antibodies are the second most-used bioreceptors for the development of biosensors [9]. The resulting immunosensors have been praised for being extremely sensitive and versatile, showing extremely low detection

limits and being suitable for a vast number of applications [11–13]. Antibodies, or immunoglobulins, are glycoproteins produced by animals as a response to antigens, foreign agents that might be a threat to a healthy organism. To neutralise the antigen, antibodies recognise an specific region of the antigen (the epitope) and bind it by their antigen binding region (Fab). Depending on the antibodies production method, they can be classified as polyclonal or monoclonal. Polyclonal antibodies are produced by clones of several immune cells (B cells) and can recognise several epitopes of the same antigen, making them highly sensitive. On the other hand, monoclonal antibodies are produced by clones of a certain B cell and they can only recognise a particular epitope of the antigen, making them highly specific.

In recent years, nucleic acids have been also exploited as bioreceptors. They are polymers of monomeric units known as nucleotides. Depending on their function, composition and structure, they can be referred as deoxyribonucleic acids (DNA) or ribonucleic acids (RNA). Regarding their role in nature, they are mainly related to the storage of genetic information and, in case of RNA, regulation of gene expression as well [14]. For the development of biosensors it is exploited the ability of nucleic acids to hybridise with other complementary nucleic acid sequences to form specific and robust complexes. Unlike proteins or antibodies, the main advantage of nucleic acids is their easy synthesis, reducing costs and development time. Additionally, they can be easily regenerated maintaining their functionality after a biosensing experiment, allowing the biosensor to be employed in sequential experiments [15].

A special sort of nucleic acid employed as bioreceptor is aptamers. They are artificially-synthesised single-stranded DNA or RNA sequences with a certain tertiary structure that provides them with a great stability and high affinity and specificity towards target molecules or elements as diverse as nanoparticles, proteins or live cells [16]. For their synthesis, the systematic evolution of ligands by exponential enrichment (SELEX) method is carried out. It consists of alternating steps of selection and amplification of randomly-synthesised sequences. During the selection step, the sequences are exposed to the target molecule which they are expected to be specific to. In the amplification step, only those sequences capable of binding the analyte are amplified by the polymerase chain reaction (PCR), the rest are discarded. After several selection and amplification steps, an enriched pool of oligonucleotide sequences able to bind the analyte is obtained and their sequence and affinity is studied. Once characterised, the resulting aptamers can be easily synthesised at a lower cost and with higher purity than antibodies or enzymes [17]. This reduces time and costs of the development of the final biosensor (commonly referred as aptasensors). Additionally, the smaller size of aptamers, if compared with enzymes or antibodies, leads to a usually higher density of bioreceptors on the aptasensor surface, resulting in better sensitivity.

However, not only single molecules but also whole cells can be used as bioreceptors. They endow the final biosensor with a higher stability and higher resistivity to harsh environments than single biomolecules and a higher versatility, since their behaviour can be modified by genetic engineering. Additionally, they

can provide extra information related to physiology and biochemical aspects in which the analyte can be involved [18].

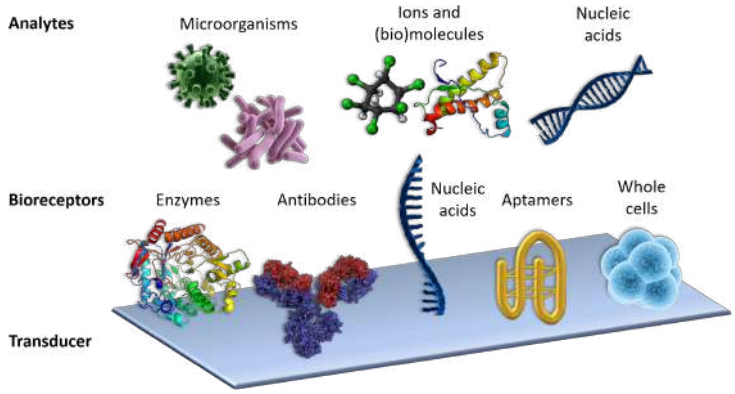

Figure 1.3. Summary of the mainly employed bioreceptors for the development of biosensors, as well as several of the analytes typically biodetected.

1.1.2 Transducers

As previously stated, the transducer transforms the physicochemical changes produced by the biorecognition events into a measurable signal. Depending on the transducer, the nature of the signal changes and, according to that, the biosensor can be mainly classified as electrochemical, piezoelectric, calorimetric or optical [19].

For the development of the first biosensor in 1954, an electrochemical transducer was employed. This sort of transducer allows the detection of the analyte by producing a measurable electrical signal when a chemical reaction in which the analyte is involved occurs. They typically consist of an electrode with the bioreceptors bound to its surface and a reference electrode separated by an electrolyte. According to the parameter measured, there are three main types of electrochemical transducers: potentiometric –potential changes are measured–, amperometric –current changes are measured– and impedimetric –impedance changes are measured [20]. One of the advantages of such sort of transducer is that the resulting electrochemical biosensors require a simple and low cost setup and have the potential for miniaturisation [19].

Less than 20 years later, in 1972, Alan Shons *et al.* developed the first piezoelectric biosensor for the determination of antibody activity in solution [21]. The working principle of piezoelectric transducers is based on the piezoelectric effect. When a mechanical stress is applied on the transducer surface, i.e. by increasing the mass over it during the biorecognition event, its fundamental resonant frequency changes, provoking the generation of a voltage. The main advantages of these transducers are their low cost and their simplicity [22].

Two years later, in 1974, the first calorimetric biosensors were published [23]. Calorimetric transducers measure temperature variations provoked by the biorecognition of the analyte or a chemical reaction in which it is involved. They usually use enzymes as bioreceptors, since they catalyse chemical processes in which an enthalpy change occurs [24]. Nevertheless, the magnitude of these enthalpy changes is not specific – many reactions can provoke the same change – which results in a lack of specificity of the final biosensor [25].

Nevertheless, the most widely explored biosensors are optical biosensors. They measure variations of the optical properties of propagated light (i.e., absorption, polarisation, intensity, wavelength, dispersion or refractive index) when the interaction between the bioreceptor and the analyte occurs. Their prevalence can be explained by the unique features they show such as immunity to electromagnetic interferences, the possibility of real-time and rapid detection of the analyte and the capability to be miniaturised and integrated at a high cost-effectiveness [26]. The first optical biosensors were mostly label-based and relied on the use of fluorescent probes. This was due to the advent of the first chemically-synthesised fluorescent labels in 1980s. Some of them were specific for an analyte and could change their fluorescent properties upon ligand binding, such as quinoline that can be quenched by chloride. However, the chemical synthesis of labels is not trivial for the detection of a certain molecule and the biorecognition and hence the sensitivity are conditioned by the efficiency of the label conjugation to biomolecules.

To overcome the limitations of fluorescence-based optical biosensors, label-free optical biodetection became more popular at the beginning of XXI century. Label-free methods do not require the addition of labels, simplifying and accelerating the detection assay and eliminating the interferences that labels could provoke in the measurement. Additionally, they allow real-time detection of biorecognition processes, which can provide kinetic data of such processes, and the detection at the same time of several analytes, which is known as multiplexing [27, 28]. Label-free optical biodetection is specially challenging when the concentration and size of the analyte are very small, but different optical methods have been developed for this aim.

The most employed technology for the development of label-free optical biosensors is surface plasmon resonance (SPR). In these biosensors, a metal layer is placed over a semiconductor layer. When the metal layer is illuminated with a light beam at a proper angle from the semiconductor layer, an evanescent field of light in the interface of both materials is created and can excite plasmons present in the metal surface. This excitation implies a loss of photons and hence, a reflectivity drop. This phenomenon only occurs at certain angles (or wavelengths), depending on the refractive index of the material over metal surface. When the recognition of the analyte by the bioreceptor occurs in the metal surface the refractive index changes and the angle (or wavelength) at which the SPR happens changes as well. By monitoring such changes, the biodetection process can be followed [29].

The SPR effect is also exploited for the development of another biosensing optical method: Surface-Enhanced Raman Spectroscopy (SERS). It aims at

enhancing Raman scattering signal of the analyte by adsorbing or approaching it to metal surfaces. Raman scattering is an inelastic process where the vibrational or rotational motion of a molecule changes by gaining or losing energy from incident photons, generating a specific fingerprint of each molecule. However, the ratio of photons that experiment this inelastic process is too low and the Raman signal is weak. To amplify it, the molecules are placed close to metal nanostructures where a localised surface plasmon resonance (LSPR) is created, enhancing the electric field intensity in the vicinity of the metal surface and hence, the electric field experienced by the molecule [30]. Since the Raman signal is characteristic of each molecule, the specificity of this technique is very high.

A drawback of SPR-based biosensors is they require expensive settings, which hardens the miniaturisation of the system. Nevertheless, other technologies aim at solving this issue.

One example are optical resonators, closed optical paths in which only resonant frequencies can propagate without suffering big losses. When a biorecognition event occurs, the effective optical length changes and the resonance frequency shifts. The monitoring of such shift allows to perform biosensing experiments. This sort of biosensor can be classified as Fabry-Pérot (FP) cavity interferometers, whispering gallery mode (WGM) resonators, asymmetric resonant cavities, and photonic crystal (PhC) cavities [31].

Recent developments in telecommunications field have led to the development of optical fibres, which have been also used for biosensing purposes. An optical fibre confines and guides light while an evanescent field is propagated on its surface, interacting with the biomolecules present there. The main advantages of optical fibres are their capability to bear extreme temperatures and environments and their small and flexible shape that allows in situ sensing. The wider employed configurations are fibre Bragg grattings, long-period gratting, optical fibre-based interferometers and evanescence wave absorption [32].

The same physical principle of optical fibres works for optical waveguides. However, the latter have demonstrated a higher sensitivity and allow the use of a wider range of materials for their fabrication. By employing optical waveguides, different optical structures can be achieved. One of the most used waveguide structures are interferometers. Their working principle consists in splitting the light into two arms (two different optical paths) and its subsequent recombination to create an interference pattern if a phase shift occurs between both optical paths. For biosensing purposes, the interaction of light with the bioreceptor-analyte complex occurs in one of the arms, whilst the other is a reference. The wider used interferometric configurations are Mach-Zehnder and Young interferometers, although other possible configurations are employed such as birefringent or bimodal waveguide interferometers. Alternative structures based on waveguides are grating optical waveguides, slot waveguides or ring resonators [33].

Other interesting optical structures for label-free optical biosensing are PhCs, consisting in a periodical arrangement of different dielectric constants in space. This avoids a range of frequencies to propagate in the medium, which constitute the photonic bandgap (PBG). Defects can be also introduced into the structure

to break the periodicity and create localised photonic states. The wavelength position of the PBG is conditioned by the effective refractive index of the PhC and that is the principle employed for biosensing purposes. When the analyte is recognised, a change in the effective refractive index occurs and a shift of the PBG position can be monitored [34].

In any of these label-free biosensors, a high surface-to-volume ratio has been demonstrated to be related with an increase in the sensitivity of the final biosensor, since a higher number of bioreceptors can be loaded in the transducer. This high surface-to-volume ratio can be achieved using porous materials for the fabrication of the transducer, instead of bulk materials. Specially in the case of label-free optical biosensors, a porous structure can mean an advantage, since the solution containing the analyte can fill the whole structure and interact with the whole optical field in some configurations, which lately will increase the sensitivity.

Probably the widest employed porous material for the development of optical biosensors is porous silicon (pSi), consisting in a closed array of nanopores. Its optical response, which can be tuned by varying its fabrication parameters, as it will be seen in next chapter, has allowed its use for the detection with a high sensitivity of insulin [35, 36], bacteria by their surface biomolecules [37, 38] or biomarkers [39], among other interesting targets (see Figure 1.4.a). Also approaches flowing through the pores have been developed, demonstrating that a 6-fold improvement in sensor response time can be achieved [40] (see Figure 1.4.b).

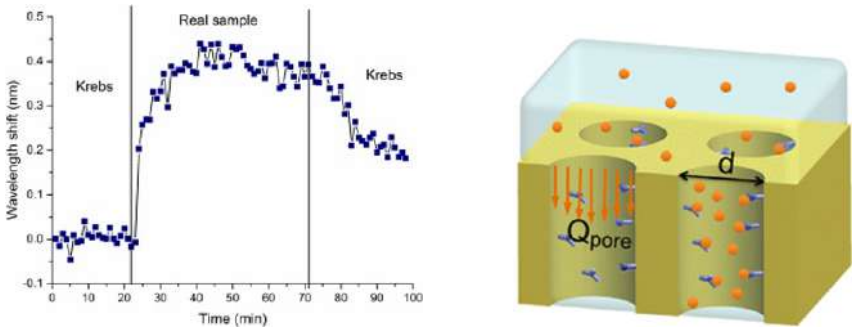

Figure 1.4. (a) Experimental results of the detection of insulin secreted from glucose stimulated human islets using a pSi biosensor. Reprinted from [36]. (b) Sketch of the flowing-through configuration proposed to increase the response time of pSi biosensors. Reprinted from [40].

pSi has been also employed as a substrate for the fabrication of ring resonators, in order to improve their Q-factor and hence, enhance their sensitivity if compared with the same structure created in a bulk material [41, 42] (see Figure 1.5.a), and waveguides-based photonic structures with outstanding performance parameters [43, 44] (see Figure 1.5.b).

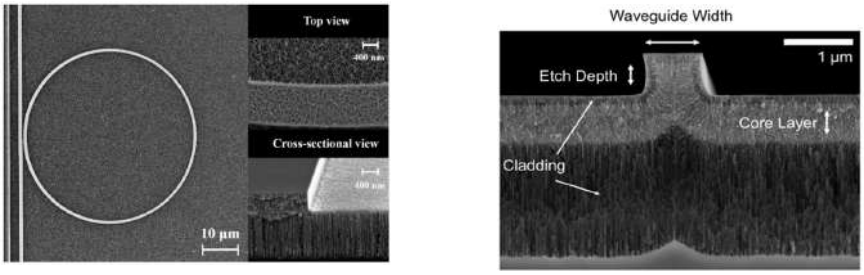

(a) (b)

Figure 1.5. (a) SEM images of a ring resonator fabricated in a substrate of pSi. Reprinted from [41]. (b) SEM image of a waveguide interferometer fabricated in a substrate of pSi. Reprinted from [43].

Additionally, pSi has been combined with plasmonic metal nanoparticles, fluorescent quantum dots or a combination of both to create ultrasensitive hybrid platforms for (bio)detection purposes [45].

Nanoporous alumina is another material with similar features to pSi that has arisen interest for the development of biosensors. Indeed, several biosensors are developed using this material [46, 47], as well as supports for the study of drug delivery [48].

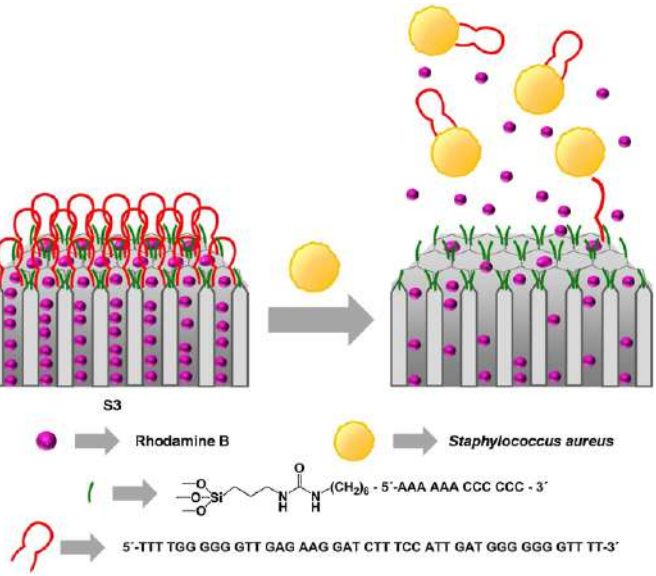

Figure 1.6. Sketch of a porous alumina biosensor for the detection of *Staphylococcus aureus* based on molecular gates technology. Reprinted from [46].

There are other examples of porous materials such as porous germanium. In this material waveguides have been fabricated, showing a lower LOD in gas sensing related to their homologous fabricated in bulk materials [49]. Nevertheless, this material is less common than the two previous ones for the development of biosensors.

1.2 Biofunctionalisation of the transducer surface

The reliability of a biosensor will ultimately depend upon how well the bioreceptor is bound to the sensor surface and remains there during the sensing step. The immobilisation of the bioreceptor on the transducer is referred as biofunctionalisation and has to accomplish several conditions such as (1) conserving the bioreceptor activity, (2) ensure a close contact between the bioreceptor and the transducer and (3) maintain the specificity and selectivity of the bioreceptor. To such aim, several biofunctionalisation approaches have been developed [50, 51].

Non-covalent binding of the bioreceptor to the surface is the easiest way of biofunctionalisation. In this approach the bioreceptor is bound to the transducer by hydrogen bonding, van der Waals forces, electrostatic forces and hydrophobic interactions. Since this approach does not require the use of chemical reagents, the biofunctionalisation process can be simplified and a lower disruption of the protein function is achieved. Nevertheless, since the attachment occurs through weak bonds, this approach shows some drawbacks such as the lack of orientation of the bioreceptors, a poor control over their location and a higher risk of removing the bioreceptors layer during washing steps. Altogether, it can result in a lower sensitivity and specificity of the final biosensor. The bond can be directly created between the bioreceptor and the transducer surface (physical adsorption) or through an intermediate previously attached to the surface of the transducer. This intermediate can be a molecule with a high affinity by the bioreceptor or by a label previously conjugated to it (affinity immobilisation) or a 3D porous matrix in which the bioreceptor is embedded (entrapment) (see Figure 1.7.a). Examples of complementary molecules are protein A or G, that bind the antibodies through their constant fragment (Fc) region, lectins that bind carbohydrate moieties present in some biomolecules, affinity tags or the streptavidin-biotin complex, among others. The latter is specially used because it forms a very stable complex that shows one of the strongest non-covalent affinity constants that exist. In the case of 3D matrixes, the sensitivity of the biosensor can be enhanced due to the higher number of bioreceptors available if compared with a flat surface. However, unspecific adsorption of target analyte on the porous matrix and its instability can compromise the final biosensor performance.

The alternative is the covalent attachment of bioreceptors to the chemically activated surface of the transducer, what improves the stability of the final biosensor. This conjugation involves the reaction of two functional groups, one in the bioreceptor and the other in the transducer surface to create a covalent

bond (see Figure 1.7.b). This binding is usually mediated by external reagents and depending on the number of reacting functional groups available in the bioreceptor, a different attachment can be obtained. If the bioreceptor has more than one reacting functional group in its structure it binds in a random or non-site directed way, what can reduce their recognition ability. On the contrary, if the bioreceptor only presents one functional group in its structure, it binds in a oriented or site-directed way, what improves its recognition ability. The most employed functional groups are amine, thiol, carboxylate, hydroxyl and aldehyde.

Almost any peptide molecule can be conjugated by amine-coupling processes, in which the primary coupling reactions occur by acylation or alkylation. The wider employed chemistry to create acylating agents consists in the reaction of a carboxylate with N-hydroxysuccinimide (NHS) in presence of a carbodiimide to form a NHS-ester derivative. The reaction of NHS-ester derivative with primary and secondary amines lead to the formation of stable amide and imide bonds, respectively. An alternative is the reaction of amines with aldehydes to form labile Schiff base intermediates, which can be chemically stabilised by reduction [52].

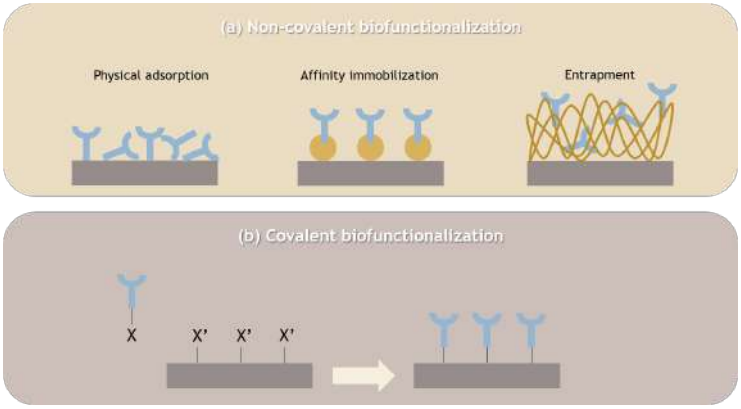

Figure 1.7. Two main approaches usually employed for the biofunctionalisation of the transducer surface. (a) Non-covalent biofunctionalisation, where weak bonds are formed. (b) Covalent biofunctionalisation, where a covalent bond is formed between the bioreceptor and the transducer when two functional groups (X and X') react.

1.3 Objectives

According to the previously exposed state-of-art of biosensors, optical transducers are the most promising ones. And it is especially interesting the use of porous materials for their development, since, as previously explained, the higher surface-to-volume ratio they show and the possibility of the sample to analyse to get into the structure is related to an increase in the sensitivity of the final device. The

main objective of this Thesis is studying the suitability of different porous optical transducers and developing a proper biofunctionalisation of their surface for the development of label-free and real-time optical biosensors. As a starting point, pSi, a well-studied porous optical transducer, as previously stated, was selected. Then, different alternative porous materials will be proposed as good candidates for label-free optical biosensing purposes. Likewise, natural and bioengineered bioreceptors will be studied. To address such a broad objective, the following specific objectives were accomplished.

1. **Study of the optical response of different porous transducers**

   The optical transducer forms the basis for the development of an optical biosensor. Therefore, the first step is finding out a suitable material and structure for its fabrication, whose optical response allows their use for label-free biosensing purposes. In this Thesis, monolayers of porous materials are proposed as suitable candidates. These structures, when illuminated with light, show a FP cavity response consisting in several fringes whose position varies with the effective refractive index of the structure and hence, with the refractive index changes provoked when a biorecognition event occurs. In the approach of this Thesis, not only a suitable response is pursued, but also a simple and low-cost fabrication of the transducer, avoiding expensive and complex nanofabrication techniques. Altogether, in this Thesis pSi, electrospun polymeric nanofibres (NFs) matrixes and commercial polycarbonte track-etched membranes (TEMs) were proposed. The former is a well-known porous material for the development of optical transducers, whilst the suitability of the rest for label-free optical biosensing purposes is going to be studied.

2. **Development of a proper biofunctionalisation protocol according to the transducer surface**

   Biofunctionalisation of the surface is essential for the final use of the biosensor and must be adapted according to the transducer material, the final use and the available commercial molecules for the recognition of the analyte (since we cannot synthesise our own). In this Thesis both covalent and non-covalent approaches will be explored for the biofunctionalisation of the transducer. Likewise, different kinds of bioreceptors will be explored depending on the analyte: DNA aptamers and antibodies. The final result of the biofunctionalisation protocol will be characterised either by real-time optical measurements or Attenuated Total Reflection (ATR) measurements.

3. **Establishment of the biosensing protocol and characterisation of the performance parameters of the biosensor**

   The last step in the development of the optical biosensor is the development of a biodetection protocol. Since the aim of this Thesis is the label-free and real-time biodetection of the analyte, a microfluidic system and a interrogation platform are needed. Subsequently, a proper processing of

the data and the analysis of the behaviour of the final biosensor must be also carried out.

4. **Exploration of natural photonic structures as transducers for the development of label-free optical biosensor**

   In line with the first objective where it is exposed the aim of this Thesis of finding porous optical transducers that not require a complex fabrication, nature could be an interesting source of resources. Nature has evolved to adapt to the environment and several species have developed photonic structures for photosynthesis or vision purposes [53], among others. One example are diatoms, algae with a silica exoskeleton that shows a periodic pattern of pores that converts them in photonic crystals when illuminated with light. Such presence of pores makes these natural structures interesting for the development of this Thesis in which the suitability of porous materials for label-free optical biosensing is studied. It is interesting to remark that the reflectance spectrum of this silica exoskeleton has not been previously used for this purpose.

1.4 Framework of the Thesis

The work presented in this Thesis was mainly carried out in the Biophotonics research group of the Nanophotonics Tecnology Center (NTC) at Universitat Politècnica de València. The NTC was created in 2005 with the aim of becoming a leading research and development center in nanophotonic science and technology. The main mission is placing NTC at the forefront of knowledge in fundamental nanophotonic science and using such knowledge to develop novel materials, devices and systems for several applications. NTC fabrication facilities –consisting of several laboratories and a 250 m^2 clean-room– were recognised as ICTS (Infraestructura Científica y Técnica Singular) and is one of the nodes of the micronanofabs network (www.micronanofabs.org), together with the Institute of Microelectronics of Barcelona (IMB-CNM) and the Institute of Optoelectronic Systems and Microtechnology (ISOM).

Regarding the Biophotonics group, it is focused on the design, fabrication and characterisation of optical transducers and its biofunctionalisation for the development of optical biosensors. For such aim, the research group uses the NTC facilities and has all the equipment required for the opto-fluidic interrogation of the developed photonic structures. Among all that equipment, 3 tunable laser sources with continuous sweep operation, 2 high speed infrared cameras, 1 high resolution optical spectrum analyser, 1 optical interrogator, 3 fluidic pumps, and 3 automatic microfluidic switches can be highlighted. Additionally, this group also has the facilities and the knowledge for the development of polymer-based microfluidic flow cells for the implementation of the whole biosensing chips. Characterisation equipment for both the optical structures and the biofunctionalisation layers is also available in the centre, such as Fourier Transform Infrared (FTIR) microscope, profilometer or atomic force microscope

(AFM), among others. Finally, the centre also disposes of several fume hoods with centrifuge, vortex or balance, among other equipment, to perform the chemical reactions required for the biofunctionalisation.

The Natural and Artificial Photonic Structures (NAPS) reseach group at International Iberian Nanotechnology Laboratory (INL) in Braga was chosen as the place where carrying out a three-month research stay. INL is the first, and so far, the only, fully international research organisation in Europe in the field of nanoscience and nanotechnology. INL is an international intergovernmental organisation (IGO) with the mission of performing cutting-edge research and development in interdisciplinary nanotechnology and to function as an innovation integrator to address major challenges of nanotechnologies, in four main areas: health, safety in environmental and food control, renewable energy and information and communication technologies. One of the aspects that stands out at INL is its infrastructure, which provides a high-tech research environment formed by state-of-the-art infrastructure equipped with the latest technologies and a 1,000-m^2 nanofabrication clean room facility (Class 1000 and Class 100) including seven bays and high accuracy labs with an extremely low vibration and EM–shielded space for some of the atomically resolved characterisation techniques.

Regarding NAPS research group, it is at the forefront of the research of photonic nanostructures, in particular bioinspired nanophotonics. From a multidisciplinary approach, they carry out experimental and numerical studies on the light management properties of unicellular organisms and vascular plants, among others. The group is also active on the design, fabrication and characterisation of new structures for light management at the nanoscale based on biomimetic concepts with applications in light harvesting and photochemical processes. Moreover, the group is at the forefront of the development of new optical setups for the characterisation of photonic nanostructures. In particular, NAPS group counts with a unique optical setup that combines measurements of microscatterometry with PAM fluorescence which makes it the only one in the world able to measure photonic properties and photosynthesis simultaneously in a single cell.

For the development of this PhD Thesis, the author was awarded a competitive grant PAID-01-17 by the Universitat Politècnica de València, as well as an associate grant to the previous one to carry out the three-month stay at INL.

Additionally, the author had the opportunity to work in a national project funded by the Spanish government for the development of a photonic biosensor: OPTONANOSENS (reference TEC2015-63838-C3-OPTONANOSENS). This project had a total duration of 45 months and aimed at developing a photonic biosensor for the rapid and effective detection of chemical, biological, radiological and nuclear (CBRN) agents in collaboration with Tecnalia and Instituto Nacional de Técnica Aeroespacial “Esteban Terradas” (INTA)-Campus "La Marañosa". This has allowed her to work together with other research institutions, experience the different stages of development of a scientific project and working in the facilities of INTA-Campus "La Marañosa" for a week.

1.5 Structure of the document

According to the objectives pursued, this Thesis document is structured in five chapters in which the results of using each one of the proposed porous optical materials as optical transducer are exposed:

- **Chapter 1:** This chapter contains the state-of-art that defines the context in which this Thesis is carried out, the objectives pursued, the framework in which these objectives were carried out and the structure of the final document.
- **Chapter 2:** This chapter contains the research and the results regarding the use of pSi as the porous material for the development of label-free optical biosensors. A deeper introduction to pSi, the structural requirements of the material for our goal, the protocol followed for its fabrication and biofunctionalisation, its characterisation and the biosensing experiments results are contained. Additionally, it is also contained the biofunctionalisation of integrated PhC waveguides and the results of the biodetection experiments using them.
- **Chapter 3:** This chapter contains the research and the results regarding the use of electrospun NFs as the porous material for the development of label-free optical biosensors. A deeper introduction in OPTONANOSENS project and the NFs potential, the fabrication of the NFs layers as optical transducers, their characterisation and biofunctionalisation and the biodetection experiment results are contained.
- **Chapter 4:** This chapter contains the research and the results regarding the use of polycarbonate TEMs as the porous material for the development of label-free optical biosensors. A deeper introduction in TEM materials, the manipulation of polycarbonate TEMs to do optical measurements and the sensing results are contained.
- **Chapter 5:** This chapter contains the research and the results regarding the use of girdle bands from diatoms as the porous material for the development of label-free optical biosensors. A deeper introduction in diatoms and their potential optical applications, the functionalisation protocol of their surface and the sensing experiment results are contained.

The document ends with the general conclusions extracted from this Thesis and the proposal of future research lines. A list showing the original contributions derived from this work is also added.

Chapter 2

Silicon-based porous optical transducers

2.1 Introduction

Silicon is a semiconductor material with a diamond crystal structure formed by covalently linked Si atoms. In 1956, Arthur and Ingeborg Uhlir were studying electropolishing of semiconductors to obtain structures suitable for microelectronic circuits. To do that, they anodised a crystalline silicon substrate in a fluoride-based electrolyte solution. They observed that, under a certain current and electrolyte composition, the surface became black or red and narrow pores appeared in <100> direction of the wafer [54]. They had just discovered porous silicon (pSi) (see Figure 2.1). However, those results were not interesting for their purpose and hence, they did not fathom out the meaning of those observations. The results went unnoticed and pretty little interest in pSi aroused until 1970's, when the possibility of thermally oxidise the structure to create silicon dioxide (SiO_2) was discovered, acting as an insulator material for electronics development [55].

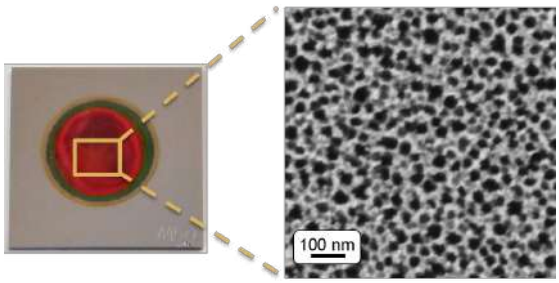

Figure 2.1. Porous silicon (pSi) sample fabricated in our laboratory (left) and Scanning Electron Microscope (SEM) image of its surface where pores can be observed (right).

However, the boom in pSi research started when its luminescence due to quantum confinement effects was discovered by Leigh Canham [56] and Ulrich Goesele and Voelker Lehmann [57]. This new characteristic added to other already well-known unique characteristics of pSi: a high surface-to-volume ratio, the possibility of easily changing its structure (porosity, size of the pore, thickness, etc.), a versatile chemical modification of its surface and compatibility with conventional silicon microfabrication technologies. Altogether led to new possibilities for the implementation of pSi in different technologies:

optoelectronics, micro-optics, energy conversion, environmental monitoring, microelectronics, wafer technology, micromachining and biotechnology [58, 59].

By mid 1990's the approach of using pSi for optoelectronic purposes, in which its luminescent properties could be exploited, was abandoned because of the low efficiency showed by the material and its low mechanical and chemical stability. However, the rest of properties of the material endowed it unique characteristics that led to the skyrocketing of the application of pSi for optics and sensors development [60]. This was specially due to its easy synthesis, avoiding complex nanofabrication techniques, its versatile morphology, easily modifiable by changing the electrochemical etching parameters, and its high surface-to-volume ratio, which leads to a higher functional area in a smaller volume with an increased number of recognition sites and predominant molecular and surfaces forces (i.e., Van der Waals, steric, hydrophobic and capillary) over bulk phenomena while flowing for sensing purposes [61]. Since the first paper of a pSi biosensor in 1997 [62], numerous works using pSi for biodetection purposes have been published, where a high sensitivity of the structure has been demonstrated [63–65].

Because of the already demonstrated potential of pSi, it was selected as an interesting porous transducer for the development of optical biosensors in this work. Nevertheless, in addition to the transducer material, the other key factor for the development of a pSi biosensor is the molecular probe employed. As explained in Section 1.1.1, many molecular probes can be used. However, since their appearance in 1990, aptamers have become very popular for the development of affinity based biosensor due to their easy chemical synthesis and modification, reversible folding and excellent stability [66]. Additionally, once identified the correct sequence of the aptamer capable of binding the target molecule, it can be easily produced by commercial providers at a lower cost than antibodies. Currently, there are hundreds of already developed sequences against different targets. Therefore, it can be obtained a very versatile optical biosensor for the detection of different target molecules by varying only the employed aptamer, if correctly developed the chemical functionalisation of the pSi surface.

Considering the promising features of pSi and aptamers, the aim of this work is to study the suitability of both elements for the development of a real-time and label-free optical biosensor with an aptamer as the recognition element (also known as aptasensor). As a first approach, thrombin was chosen as the target molecule because of the important biological role of the protein and the availability of a well-known thrombin binding aptamer (TBA) for its recognition.

Thrombin is a pleiotropic enzyme with a central role in blood coagulation. In normal conditions it is absent in blood. However, when a vascular injury occurs, the coagulation cascade is activated and thrombin is generated from its precursor plasma protein, prothrombin, to convert fibrinogen to fibrin, which aggregates together with platelets creating clots that avoid blood losses [67] (see Figure 2.2).

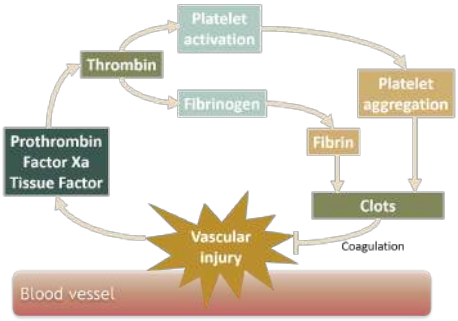

Figure 2.2. Onset of the coagulation cascade when a vascular injury occurs to avoid blood losses by the formation of a blood clot.

Thrombin generation is divided into three consecutive stages characterised by the molecular factors involved and the final thrombin concentration achieved: initiation (from 1 nM to ∼30 nM), propagation (from ∼30 nM to >800 nM thrombin), and termination (when thrombin is no longer produced and free thrombin is inactivated) [68–72] (see Figure 2.3). Such a complex process is known as vascular haemostasis and the disruption of this haemostatic state is related to the onset of diseases such as thrombosis, atherosclerosis [73], Alzheimer's [74] or growth, metastasis, and angiogenesis of tumours [75, 76].

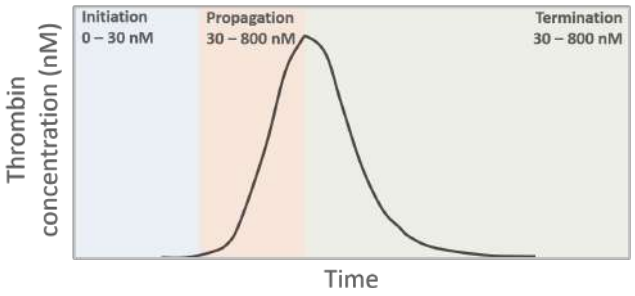

Figure 2.3. Thrombin generation along time.

Consequently, in recent years, a great interest has arisen in order to develop systems able to accurately monitor variations in thrombin concentration. Currently, some thrombin generation assays are commercially available. However, most of them are based on indirect measurements and the use of labelled substrates. Additionally, they require laborious preparation of the sample, cannot assess all the phases of haemostasis, and the lack of standardisation prevents their use in general clinical practice [77–79]. To overcome such limitations, aptamer binding assays have come to the attention of researchers as a suitable approach due to the outstanding features of aptamers as biorecognition molecules [66].

In this work, we aim at overcoming such limitations with a pSi-based aptasensor. We will focus on studying the initiation phase of the thrombin generation process. At this stage, very reduced thrombin concentrations (ranging from 1 nM to 30 nM) are produced to trigger the conversion of fibrinogen to fibrin and hence, the clotting process [68, 71, 72]. However, typically used clinical tests to study thrombin generation are not sensitive enough to detect this thrombin concentration range [69]. Some works have reported the development of aptasensors able to detect lower concentrations of thrombin, for example, in research of Chen, X. et al. [80] and Cho, H. et al. [81]. However, they require the incubation of thrombin and the aptamer as well as the use of dyes to measure the final aptamer-thrombin complexes, thus not offering the possibility of performing a continuous and label-free monitoring of the binding events.

The chosen aptamer is the very well-known first TBA aptamer selected in 1992 by the SELEX method among 10^{13} sequences against thrombin [82, 83]. It is a single-stranded DNA with the 15-mer sequence 5' - GGTTGGTGTGGTTGG - 3' that has a high specificity and affinity for thrombin. According to nuclear magnetic resonance (NMR) measurements, TBA folds in a unimolecular antiparallel quadruplex with a chair-like conformation stabilised by cyclic hydrogen bonding of four guanines and coordination ions between adjacent stacks of G-tetrads. This G-tetrads are surrounded by two TT loops on one side and a TGT loop on the other side (see Figure 2.4.a). This structure was also confirmed by X-ray measurements of thrombin-TBA complex, although slight differences regarding the connection of the central bases were observed between the two models [82]. The recognition of thrombin by TBA occurs through the exosite I of thrombin (the recognition site of fibrinogen) and the two TT loops of TBA [84] (see Figure 2.4.b).

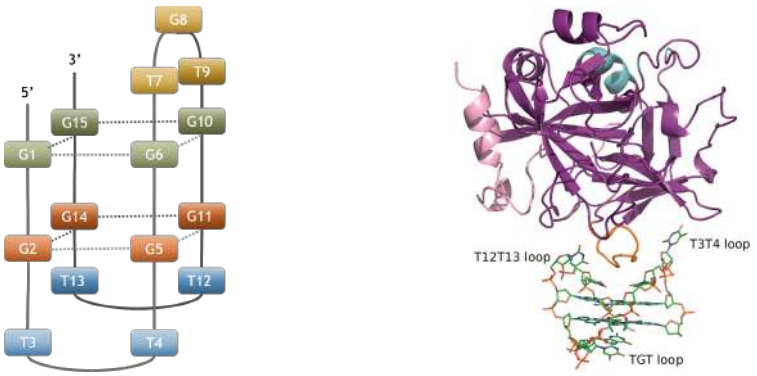

Figure 2.4. (a) Conformation of thrombin binding aptamer (TBA) employed in this work for the functionalisation of pSi. (b) Structure of thrombin-TBA complex obtained from [82]. The different functional regions of thrombin protein are coloured as follows: heavy chain in purple, light chain in pink, exosite I in orange and exosite II in cyan.

2.2 Fabrication of porous silicon

In presence of water or air, silicon is unstable and tends to create a native oxide layer (i.e., SiO_2 layer) according the Equation 2.1 that protects the underlying silicon from further oxidation in acidic or neutral medium .

$$Si + O_2 \longrightarrow SiO_2 \tag{2.1}$$

The resulting SiO_2 layer can be easily removed by immersing the wafer in an aqueous solution of hydrofluoric acid (HF), where SiO_2 reacts to form the water-soluble ion ${SiF_6}^{2-}$, according to the Equation 2.2. This reaction is driven by the fact that Si−F bond has a higher dissociation enthalpy than Si−O bond.

$$SiO_2 + 6\,HF \longrightarrow {SiF_6}^{2-} + 2\,H^+ + 2\,H_2O \tag{2.2}$$

However, in absence of such oxide native layer, the dissolution of bare silicon in HF to create a porous structure becomes extremely slow, unless a strong oxidising agent or an electrochemical reaction is carried out. This is the reason why the wider employed method for pSi fabrication is the electrochemical etching employing HF. The electrochemical reaction that drives pore formation is explained in Equations 2.3 - 2.5 and graphically showed in Figure 2.5.

$$Si + 2\,HF + n\,h^+ \longrightarrow SiF_2 + 2\,H^+ + (2\text{-}n)\,e^- \tag{2.3}$$

$$SiF_2 + 2\,HF \longrightarrow SiF_4 + H_2 \tag{2.4}$$

$$SiF_4 + 2\,HF \longrightarrow H_2SiF_6 \tag{2.5}$$

Where h^+ is the hole, e^- the electron and n is the number of charges exchanged.

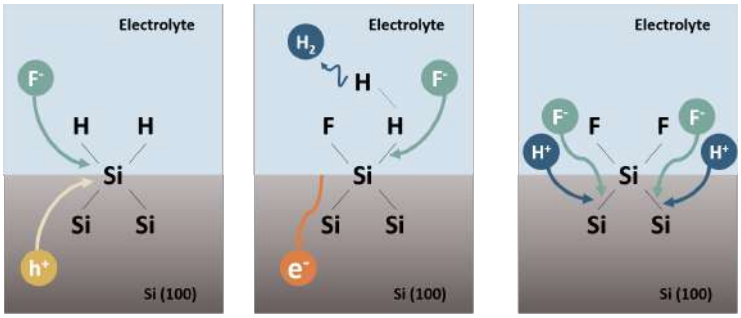

Figure 2.5. Electrochemical reaction to produce the pores in the silicon wafer.

To perform the electrochemical reaction, two electrodes must be defined: the cathode, where the reduction reaction occurs, and the anode, where the oxidation reaction occurs. In pSi fabrication, the former is a platinum electrode

and the latter, the silicon wafer itself, both separated by the electrolyte solution (see Figure 2.6.a). When the positive current supplied by a power source passes through the silicon wafer, silicon is oxidised, enhancing the formation of SiO_2 that reacts with HF to produce $SiF_6{}^{2-}$ while giving rise to the porous structure [85]. The voltage also promotes the movement of holes and fluoride ions to the silicon surface, favouring the pore formation.

For the development of this Thesis, an electrochemical cell made on Teflon –resistant to HF– was employed. It allows the vertical electrochemical attack of the silicon, giving rise to a 1 cm^2 pSi surface. The gap between the electrodes can be varied by displacing the platinum electrode and a maximum volume of 10 ml of the electrolyte solution can be contained. A copper contact was employed to connect the silicon wafer to the current generator as the anode and a coiled platinum electrode was employed as the cathode (see Figure 2.6.b).

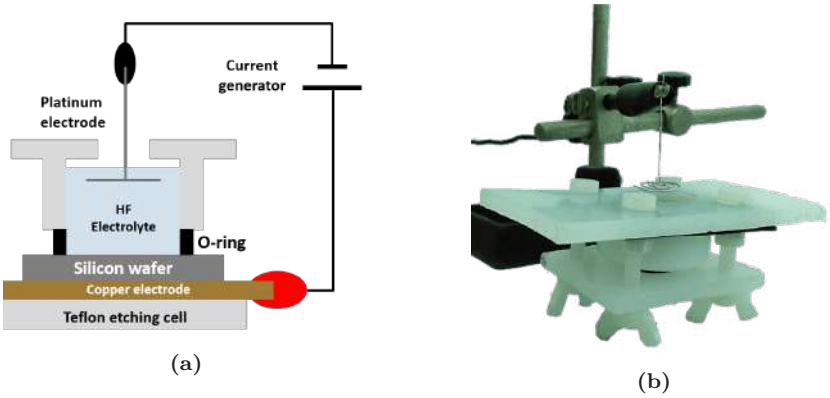

Figure 2.6. (a) Scheme of the configuration employed for the electrochemical etching of pSi. (b) Electrochemical etching cell employed in this work for the fabrication of pSi samples.

2.3 Importance of pore diameter for sensing purposes

Pore diameter is a critical feature of pSi for biosensing applications. It conditions the flow dynamics and limits the size of the molecules and particles entering the pores. According to the diameter of the pores, the resulting pSi can be classified as microporous (pore diameter of <2 nm), mesoporous (pore diameter from 2 nm to 50 nm) and macroporous (pore diameter of >50 nm).

For our objective, it was estimated that a pore diameter of 20 nm to 30 nm (mesopores) would be suitable. The diameter of the aptamer employed is ∼1 nm [86] and the diameter of thrombin is ∼5 nm [87]. Therefore, a minimum diameter of 12 nm is required, plus an extra diameter required to let the solutions flow into the pores.

To create a big enough pore for our purpose, it must be considered that the final pore diameter is conditioned by the configuration of the electrochemical

etching. Current density and electrolyte composition are the main affecting factors [88], but also does the wafer doping: heavily doped p-type silicon usually forms micropores, whilst mesopores and macropores are easily achievable in low-doped silicon [89, 90].

In our laboratory, only heavily-doped p-type silicon with a resistivity of $\sim$17 mΩ cm were available. As previously stated, only micropores are typically obtained using them. The high presence of positive charges in the wafer leads to a fast creation of micropores, hardening the achievement of macro and mesopores. This was observed when our high resistivity silicon samples were chemically anodised in a typical solution of 37.5 % HF in pure ethanol at a current density ranging from 150 mA cm^{-2} to 300 mA cm^{-2}. The biggest pores obtained had a diameter of 15 ± 5 nm, too narrow for the thrombin detection purpose.

Nevertheless, although difficult, it is not impossible obtaining macropores in p-type heavily-doped silicon. But currently, there is not a general protocol for it. Therefore, the protocol to create macropores in our silicon wafers had to be optimised in our laboratory and two different approaches were studied:

1. Fabricate microporous pSi using the wider-employed electrolyte solution composed by HF and ethanol and then, increase the pore diameter by:
   - Oxidation and dissolution in HF of the structure
   - Dissolution of the structure in alkali solutions
2. Fabricate mesoporous pSi using organic electrolytes.

2.3.1 Increase of the pore diameter after pSi synthesis

2.3.1.1 Oxidation and dissolution of the structure

A thin SiO_2 layer can be created over the pSi structure by thermal treatment. Approximately 45 % of the thickness of the layer grows in the silicon crystal and the rest, in the pore [91]. As previously explained in this chapter, SiO_2 can be dissolved by HF. Therefore, if after the thermal treatment the sample is exposed to a <5 % HF solution, an increase of the pore radius equivalent to the 45 % of the thickness of the SiO_2 layer can be achieved (see Figure 2.7). A consequence of this treatment is the narrowing of the pore walls that could lead to a reduction in the stability of the porous layer.

Figure 2.7. Increase of the pore diameter by oxidising and then removing the oxide layer by HF treatment.

In our case, pSi was fabricated by anodisation with a 17 % HF solution and a current density of 6 mA cm^{-2} applied for 100 s, resulting in a microporous pSi structure. Then, the sample was placed in a plasma asher PVA Tepla 200 (PVA Tepla, Wettenberg, Germany) for 20 min at 1.5 mbar and 400 W with a O_2 flow to create the oxide layer. Finally, it was immersed in <5 % HF solution, thoroughly rinsed with MilliQ water and dried with nitrogen. Following the procedure, the bigger pores obtained had a diameter of ∼25 nm.

2.3.1.2 Alkali solutions

NaOH or KOH aqueous solutions can react with Si–H bonds present in pSi and bulk silicon to form H_2 according to the equation 2.6 and 2.7, respectively [92]:

$$Si_xSiH_y + MOH + H_2O \longrightarrow M_2SiO_3 + H_2 \tag{2.6}$$

$$Si + MOH + H_2O \longrightarrow M_2SiO_3 + H_2 \tag{2.7}$$

where M can be K or Na and $\mathbf{x} + y = 4$.

However, this reaction is faster in pSi than in bulk silicon due to the high surface area and relatively strained nature of Si-Si bonds in pSi [85]. Therefore, these reactions can be used to increase the pore diameter by immersing the pSi in such solutions after their fabrication. In our case, 5 min immersion in different KOH concentrations were analysed. The bigger pores were obtained with a pSi sample etched with a 1:4 HF:EtOH electrolyte solution, a current density of 6 mA for 120 s and finally immersed in a 8 M KOH solution in deionised (DI) water. The average pore diameter of this sample was ∼25 nm.

2.3.2 Increase of the pore diameter during electrochemical etching. Organic electrolyte.

Organic solvents, such as dimethyl formamide (DMF) or dimethyl sulfoxide (DMSO), are commonly added to HF etching solutions to create organic electrolytes. It has been demonstrated that the use of organic electrolytes allows the formation of macropores in p-type silicon. It is hypothesised that the aprotic character of DMF and DMSO leads to a bigger mobility of anions resulting from the electrochemical etching, e.g. F^- and $HF_2{}^-$, enhancing the silicon dissolution rate. Differences among organic solvents are explained by their oxidizing character, redox and built-in potentials and the solubility of the products of the reaction on them [93].

In our case, the biggest pores were obtained with DMSO. Using a current density of 11 mA cm^{-2} for 90 s and an organic electrolyte with 82 v/v% DMSO and HF and DI water in the same volumetric proportion, pores of ∼50 nm were obtained. However, the pSi layer showed very low stability due to the extremely thin walls of the pores (∼10 nm).

Using DMF at the same concentration and a current of 11 mA cm^{-2} for 90 s the biggest pores showed a diameter of ∼30 nm, but a better stability of

the structure was observed due to the increased interpore distance (∼20 nm). Such stability was improved by reducing the DMF concentration up to 67 v/v%, obtaining an interpore distance of ∼40 nm and pores with a diameter of ∼25 nm when a current density of 22 mA cm^{-2} is applied for 90 s. A layer thickness of ∼2 µm was obtained. Additionally, the homogeneity of the sample was better using DMF than using DMSO.

Considering the pore diameters obtained with each approach, big enough pores for our purpose were obtained using all the approaches studied. However, since the use of organic solvents mean a single fabrication step, this approach was selected as the suitable one for the fabrication of the samples used in this work. DMF was used instead of DMSO since a more stable structure, with thicker walls of the pores, was obtained (see Figure 2.8).

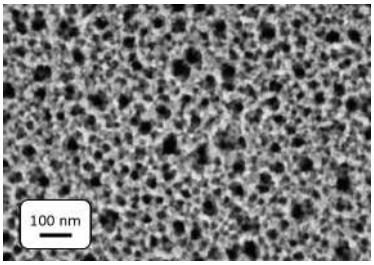

Figure 2.8. SEM image of a pSi prepared with 1:1:4 HF:DIW:DMF, with a density current of 24 mA cm^{-1}

2.4 Optical structures

Once determined the electrolyte solution required to obtain big enough pores for our biosensing purposes, the optical response of the resulting pSi structure should be defined, since it also conditions the final detection. The optical response of a pSi structure depends on how several pSi layers with different effective refractive index (n_{eff}) are combined. This n_{eff} depends on the porosity of the layer that can be modified by changing the number of pores and/or their diameter. In our laboratory, three different optical structures can be fabricated:

1. **Monolayer:** it consists in a single pSi layer that behaves like a FP cavity, showing a fringe pattern where the maximum peaks appear at λ_m according to the Equation below [94, 95]:

$$\lambda_m = 2n_{eff}\frac{d}{m} \tag{2.8}$$

where n_{eff} and d are the effective refractive index and the thickness of the pSi layer, respectively, and m is an integer.

The effective refractive index of the porous structure can be calculated according to Looyenga equation:

$$n_{eff}{}^{2/3} = (1 - P)n_{bulk}{}^{2/3} + Pn_{void}{}^{2/3} \tag{2.9}$$

where n_{bulk} is the refractive index of the material that constitutes the pore walls, n_{void} is the refractive index of the medium filling the pores and P is the porosity.

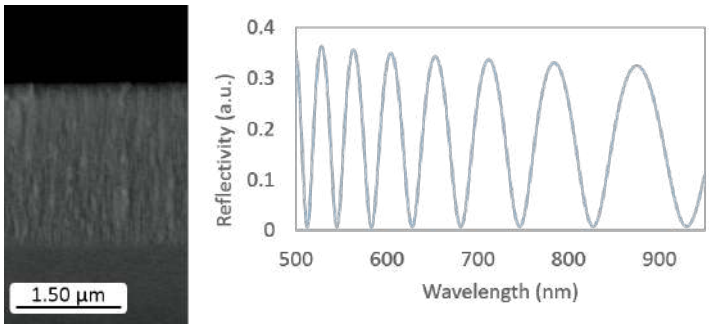

Figure 2.9. SEM image of the cross-section of a pSi monolayer (left) and the typical Fabry-Pérot (FP) cavity response shown by this kind of structures, where several peaks are observed (right).

2. **Distributed Bragg reflector (multilayer):** this configuration consists in a double pSi layer, each layer with a different n_{eff} and a thickness $\lambda/4$, that is consecutively repeated along the thickness of the silicon wave (z-axis) as many times as desired, resulting in a 1D photonic crystal that shows a PBG centred at λ in its optical response [96].

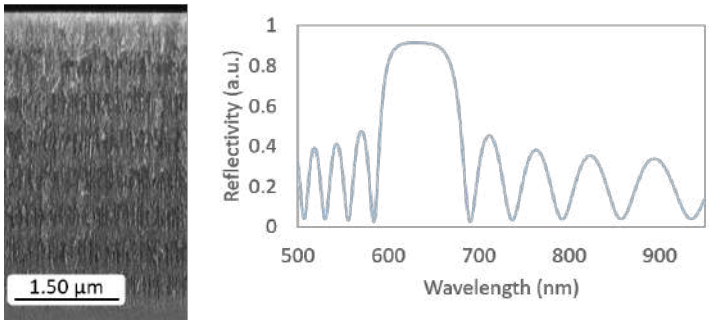

Figure 2.10. SEM image of the surface of a pSi distributed Bragg reflector (left) and the typical spectrum shown by this kind of structures (right).

3. **Optical microcavity:** this structure consists of two Bragg reflectors inverted respect to each other and separated by a pSi layer with a refractive

index n_c –the same or different refractive index to the ones used for the DBRs layers– whose thickness is a integral multiple of $\lambda/2n_c$. This results in a PBG with a centred resonance at λ [97, 98].

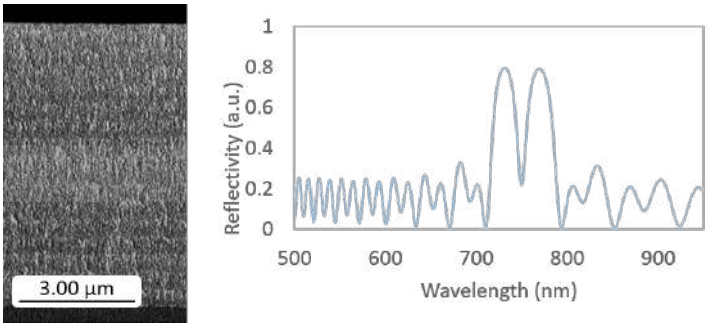

Figure 2.11. SEM image of the surface of a pSi microcavity (left) and the typical spectrum shown by this kind of structures, where a resonance can be observed at 750 nm (right).

In this work, it was decided to work with monolayers, although the quality factor of the resonance of microcavities is typically higher than that of reflectance peaks in monolayers, which usually means a higher resolution of the sensor. Monolayers are the simplest-to-fabricate structures and the fact that only one layer of porous material has to be filled by the analyte solution is expected to make easier the biofunctionalisation and final detection experiments.

2.5 Chemical activation and passivation of the surface

As fabricated, pores surface is covered by Si–H species (SiH, SiH_2 and SiH_3) with a reducing character that can be exploited for the activation and subsequent functionalisation of pSi surface. Furthermore, the porous structure can also have an influence in the functionalisation of the surface due to some particular features it shows, such as its huge area, an increased lattice strain if compared with bulk Si, the microcapillary forces that appear in the pores and the quantum confinement in the structure [99].

For the activation of the surface, most of the approaches imply the formation of Si-O and Si-C bonds on pSi surface[100], which not only endow the surface with new chemical groups but also passivate the structure and hence, stabilise its optical response when aqueous solutions are flowed in later sensing experiments.

In this work, two surface activation approaches were employed: hydrosilylation and oxidation of the surface.

2.5.1 Thermal hydrosilylation

Thermal hydrosilylation consists in the reaction at <200 °C of 1-alkenes with the Si-H species on the surface of as-prepared pSi to create a alkyl monolayer bound

through a Si-C bond. If the 1-alkene molecule has a functional group in its chain, pSi will add a new functionality to its surface, making it more reactive for further biofunctionalisation. In this work, undecylenic acid was employed and its covalent attachment to the pSi surface was performed by a thermal reaction. As a result, pSi was covered by carboxyl moieties, adding additional functionality to the pSi [101] (see Figure 2.12).

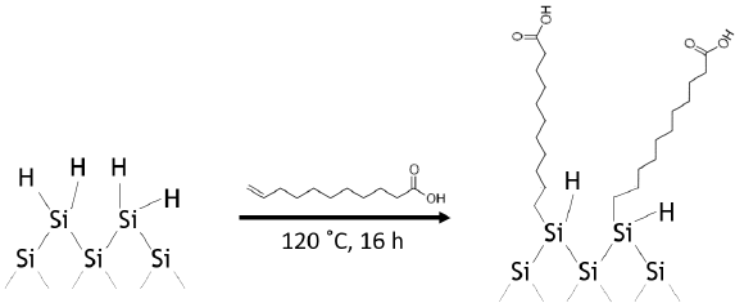

Figure 2.12. Thermal hydrosylilation scheme.

Thermal hydrosilylation results in the formation of Si – C bonds, less reactive than Si – O bonds formed by thermal oxidation. This fact, together with the hydrophobicity of the added alkyl chains and the disappearing of Si – H bonds –prone to oxidation– protects pSi from further oxidation in basic and aqueous solutions and hence, endow it with a higher stability in such media [102, 103]. This is especially interesting for biosensing purposes in which the analyte is usually flowed in aqueous solutions.

In this work, pSi samples were immersed overnight in pure undecylenic acid at 120 °C in an oil bath. Previously to the sample immersion, the Erlenmeyer flask and undecylenic acid were purged with nitrogen. Once immersed the sample, the Erlenmeyer flask was purged again for ∼15 min and tightly sealed. A balloon with nitrogen is used to maintain the inert atmosphere during the whole reaction. To remove the non-reacting undecylenic acid, samples were immersed in ethanol and then, isopropyl alcohol (IPA) for 5 min each. This process was repeated three times. Finally, samples were rinsed with DI water and dried with a nitrogen flow.

2.5.2 Oxidation of pSi

Oxidation of pSi results in the formation of a SiO_2 layer on the pSi layer. As previously explained, such silica layer has a passivating role that protects the underlaying silicon from degradation in acid and neutral aqueous media. But it also endows the surface with Si – OH bonds. They have a high reactivity for further biofunctionalisation and increase the hydrophilicity of the porous structure, which must ease the entrance of liquids inside during biofunctionalisation and biodetection steps.

To achieve such SiO_2 layer, several techniques have been applied, such as thermal oxidation or chemical oxidation, being the former the most used. It consists in converting Si into SiO_2 by thermolysis at temperatures below 950 °C, to avoid the modification of the shape of the structure [104–106] (see Figure 2.13).

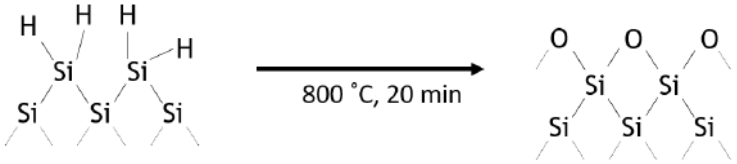

Figure 2.13. Thermal oxidation process of pSi samples.

In this work, pSi was oxidised using a tube furnace CTF 12 (Carbolite Gero Ltd, Sheffield, United Kingdom). Samples were heated at 800 °C, with a heat up rate of 13 °C min^{-1}, while flowing 4 l min^{-1} of nitrogen. When 800 °C were reached, oxygen was flowed at 2.175 l min^{-1} for 20 min. Finally, a cool down rate of ∼2 °C min^{-1} was set until reaching room temperature while flowing nitrogen.

2.6 Biofunctionalisation and biodetection of thrombin using pSi

Once activated the surface, crosslinkers were employed to covalently attach the aptamer to the surface. In oxide-activated surface, available hydroxyl groups are employed for further surface biofunctionalisation. Whilst in undecylenic acid activated pSi, carboxyl groups were employed.

Regarding the employed aptamers, it was chosen a well-known TBA with a high affinity towards thrombin [82, 83]. It was purchased from NZYTech, Lda (Lisbon, Portugal). The sequence was 5'- NH2 - $(T)_{12}$ - GGTTGGTGTGGTTGG - 3'.

2.6.1 Biofunctionalisation protocol of hydrosilylated pSi

Once hydrosilylated, the carboxyl groups on the pSi surface were activated using EDC/NHS solution, a zero-length crosslinker. For such aim, the sample was immersed in a solution of 100 mM EDC and 100 mM NHS for 30 min at room temperature. Then, the sample was immersed in DI water for 5 min and dried with nitrogen. Afterwards, a drop of 5 µM TBA solution in 1 X PBS with 1 mM $MgCl_2$ was placed on the sample and let to react overnight in a humidity chamber. 5 µM TBA solution in 1 X PBS with 1 mM $MgCl_2$ was heated at 95 °C for 5 min and let to cool down at room temperature for 15 min before being dropped to assure the correct folding of the aptamer. Finally, the sample was rinsed with 1 X PBS and dried with nitrogen (see Figure 2.14).

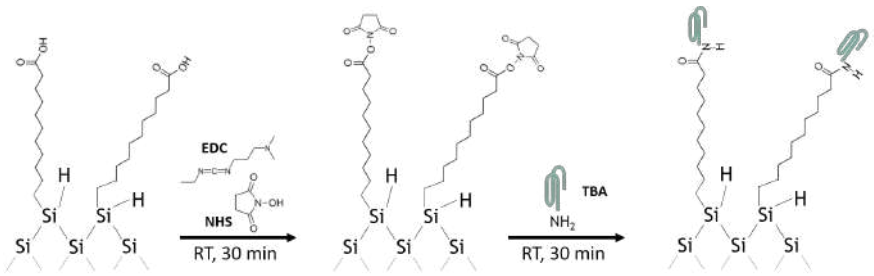

Figure 2.14. Biofunctionalisation protocol of hydrosilylated pSi.

2.6.2 Biofunctionalisation protocol of oxidised pSi

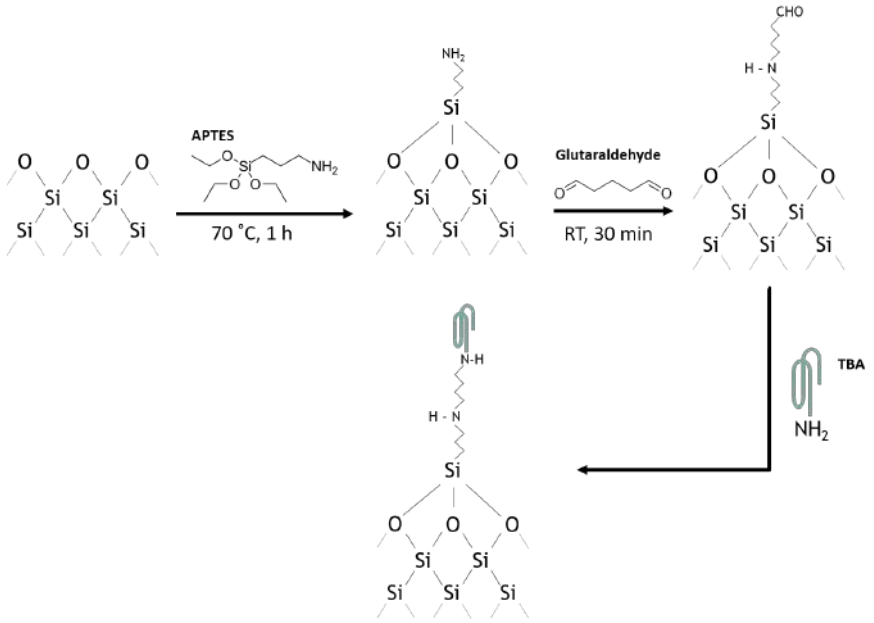

Figure 2.15. Biofunctionalisation protocol of oxidised pSi.

Figure 2.15 summarises the biofunctionalisation protocol followed in oxidised pSi. Once oxidised, samples were immersed in a 3:1 H_2SO_4:H_2O_2 solution (piranha solution) for 30 min to increase the surface density of reactive hydroxyl groups. Then, the sample was rinsed with DI water and dried with nitrogen. Afterwards, the sample was immersed in a solution of 1 % (3-aminopropyl)triethoxysilane (APTES) in 95 % ethanol aqueous solution for 1 h at 70 °C. Such solution was prepared 5 min before using it to allow the hydrolysis of APTES. Then, the sample was immersed in 95 % aqueous ethanol solution for 5 min, rinsed with ethanol, DI water and dried with nitrogen. It was then cured at 110 °C for

15 min to remove adsorbed water molecules and create stable Si–O–Si bonds. Afterwards, the sample was immersed in a 2.5 % glutaraldehyde solution in 1 X PBS for 30 min. Then, the sample was immersed in 1 X PBS for 5 min, rinsed with DI water and dried with nitrogen. Finally, a drop of 5 µM TBA solution in 1 X PBS with 1 mM $MgCl_2$ was placed on the sample and let to react overnight in a humidity chamber. As previously explained, TBA solution was heated and cool down to assure the correct folding of the aptamer. Finally, the sample was rinsed with 1 X PBS and dried with nitrogen.

2.6.3 Real-time and label free optical biodetection of thrombin

For real-time optical biodetection of thrombin a goniometer –for the optical interrogation– and a flow cell –to deliver the solutions to the pSi surface– were employed.

The goniometer consists of two arms holding optical elements that rotate around a central axis to direct, focus and collect the optical beam employed for the interrogation of the sample. For the development of this Thesis, each arm is placed at 15° from the perpendicular axis. In one arm, an optical fibre with a collimator was connected to a HL-2000 tungsten halogen lamp (Ocean Optics, Dunedin, FL, USA) and used to illuminate the pSi layer. On the other arm, another optical fibre connected to a Flame T spectrometer (Ocean Optics, Dunedin, FL, USA) collected the reflected light. Employing the Ocean Optics software, the reflectivity spectrum was recorded every 4 s with a resolution of 207.5 pm and an integration time of 3 ms (see Figure 2.16.a). To carry out the calibration of the equipment, an aluminium sample was used.

The flow cell consists of a polymethylmethacrylate (PMMA) cover with an inlet and an outlet tube and a double-sided adhesive with a 100 µm height and a cavity of 2 mm × 7 mm (width × length) on its centre that constitutes the flowing channel. The outlet tube was connected to a syringe pump working in withdraw mode at 20 µl min^{-1} (see Figure 2.16.b).

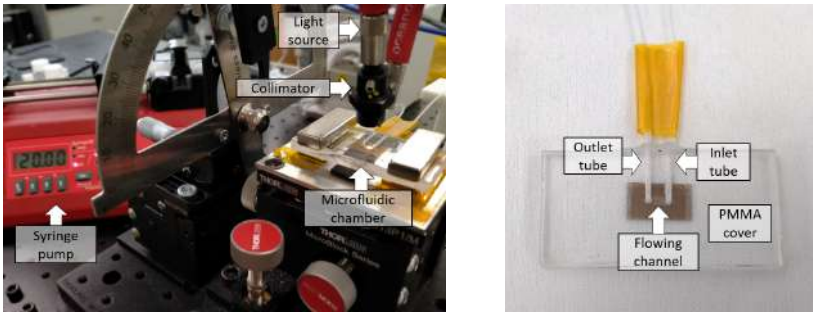

(a) **(b)**

Figure 2.16. (a) Picture of the interrogation setup employed for the reflectivity optical measurements performed in the visible range and (b) the flow chamber employed to deliver solutions over the sample.

The biodetection process was monitored by studying the change of the effective refractive index of the structure provoked by the attachment of thrombin molecules to the TBA (see Figure 2.17). According to Equation 2.8, this change would lead to a shift of the spectrum. Therefore, we can follow the biorecognition events by monitoring this spectral shift of the reflectance spectrum. Additionally, changes in the effective refractive index of the structure can be also found out by studying changes in its effective optical thickness (EOT) because they are proportional according to the following equation: $EOT = 2n_{eff}L$, where n_{eff} and L are the effective refractive index and the thickness of the layer, respectively. For both processing approaches MATLAB (R2019b, MathWorks, Natick, MA, USA) was used.

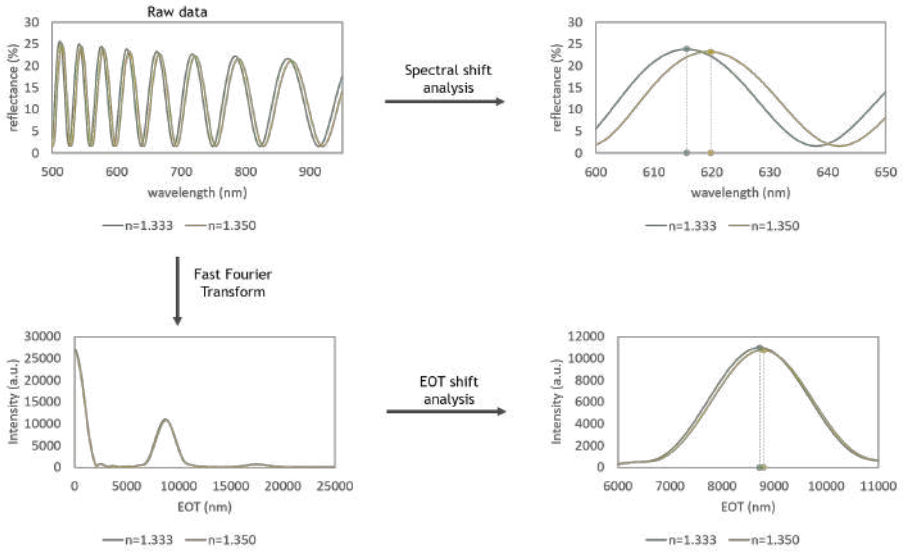

Figure 2.17. Scheme of the data processing. Raw data can be processed in two ways: directly quantifying the spectral shift (spectral shift analysis) or performing a FFT of the signal and measuring the change in the effective optical thickness (EOT) of the sample (EOT shift analysis).

To monitor the shift experienced by the reflectance spectrum when the refractive index of the surrounding medium changes along the experiment, raw data obtained from the spectrometer were interpolated to increase the resolution up to 1 pm and filtered to reduce the setup noise. For this, a Fast Fourier transform (FFT) of the interpolated data was carried out. Then, normalised frequencies above 0.03 were eliminated and an inverse FFT was applied to the resulting data to recover the filtered reflectance spectrum. Afterwards, the maximum reflectivity peak to follow was selected and a Gaussian fitting was applied to localize maximum peak position. This process was automatically repeated for all the obtained reflectivity spectra to determine the shift of the

maximum peak.

To monitor the change in the EOT of the sample, the Fourier transform is applied to the reflectance intensity versus frequency. For such aim, the wavelength axis of the reflectance spectrum is changed from wavelength to wavenumber ($1/wavelength$). Then, a cubic-spline interpolation is applied to obtain 4095 data points. Afterwards, a Hanning window – zero padded to 2^{24}– is applied. Finally, the FFT algorithm is applied to the zero-padded reflectance spectrum, obtaining a main peak whose position on the x-axis ($1/wavenumber$) gives the EOT value. This process was automatically repeated for all the obtained reflectivity spectra. In the sensogram, the variation of EOT normalised to the initial EOT value (EOT_0) was depicted as a function of time.

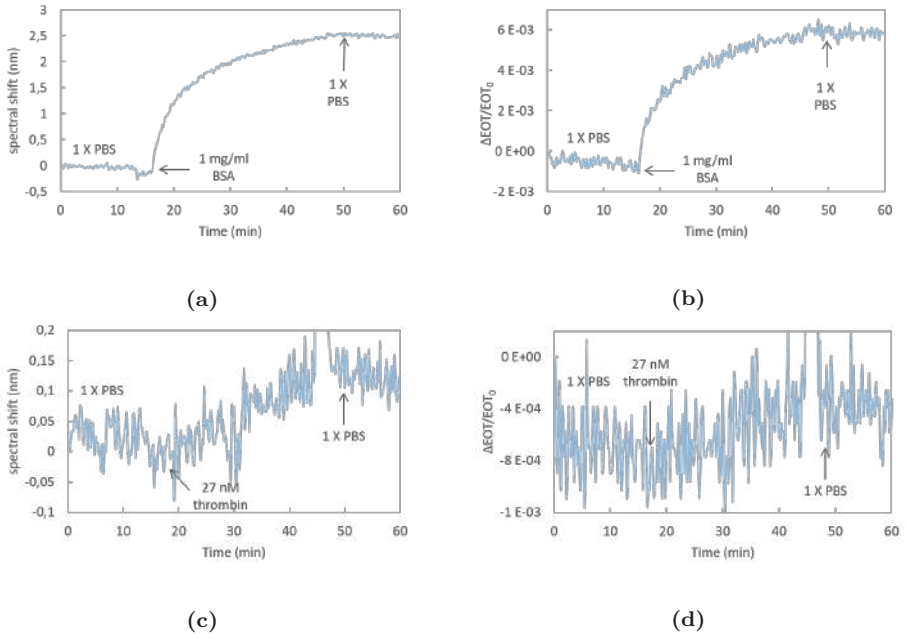

Figure 2.18. Experiment of thrombin biodetection using hydrosilylated samples. Firstly, the surface was blocked with bovine serum albumin (BSA), the sensogram is shown for (a) spectral shift and (b) EOT change analyses. Then, 27 nM thrombin was flowed and the sensing curve is shown for (c) spectral shift and (d) EOT change analyses.

In both, oxidised and hydrosilylated samples, $1\,mg\,ml^{-1}$ BSA in 1 X PBS was firstly flowed. This protein reacts with the remaining reactive aldehyde and carboxyl groups from glutaraldehyde and undecylenic acid, respectively, and block the remaining voids on the pSi surface. Both things avoid thrombin from unspecific attachment.

In hydrosilylated pSi, after flowing $1\,mg\,ml^{-1}$ BSA, a net spectral shift of 2.62 nm and a variation of the EOT of 6.39×10^{-3} units were observed. This

shift is maintained after flowing 1 X PBS, what indicates a stable blocking of the surface. For biosensing, a solution of 27 nM thrombin in 1 X PBS was flowed and a spectral shift of ∼120 pm and a EOT variation of 4.5×10^{-4} units was observed. Again, these changes were maintained when 1 X PBS was finally flowed (see Figure 2.18). In order to elucidate the capability to discriminate thrombin detection from noise, SNR was calculated assuming the noise floor as three times the standard deviation of the temporal signal during the first 10 minute, while flowing 1 X PBS, and setting a threshold of $\sqrt{2}$ as a good indicator of SNR. The noise floor calculated for the spectral shift was 81 pm, leading to a SNR of 1.5, slightly higher than $\sqrt{2}$. Regarding EOT measurements, the noise floor calculated was 7.93×10^{-4}, leading to a SNR of 0.6, under the threshold. Thus, demonstrating the capability to clearly discriminate thrombin detection from noise only by measuring the spectral shift.

In oxidised pSi, after blocking the surface with BSA, a net spectral shift of 0.85 nm and a net EOT shift of 1.32×10^{-3} units occurred. When 27 nM is flowed, a net spectral shift of ∼85 pm and a net EOT change of 3.3×10^{-4} units were observed (see Figure 2.19). The noise floor calculated for the spectral shift was 140 pm, leading to a SNR of 0.6, below the threshold. Regarding EOT measurements, the noise floor calculated was 3×10^{-4}, leading to a SNR of 1, under the threshold. Thus, demonstrating that using APTES-functionalised samples, thrombin detection cannot be clearly distinguished from noise.

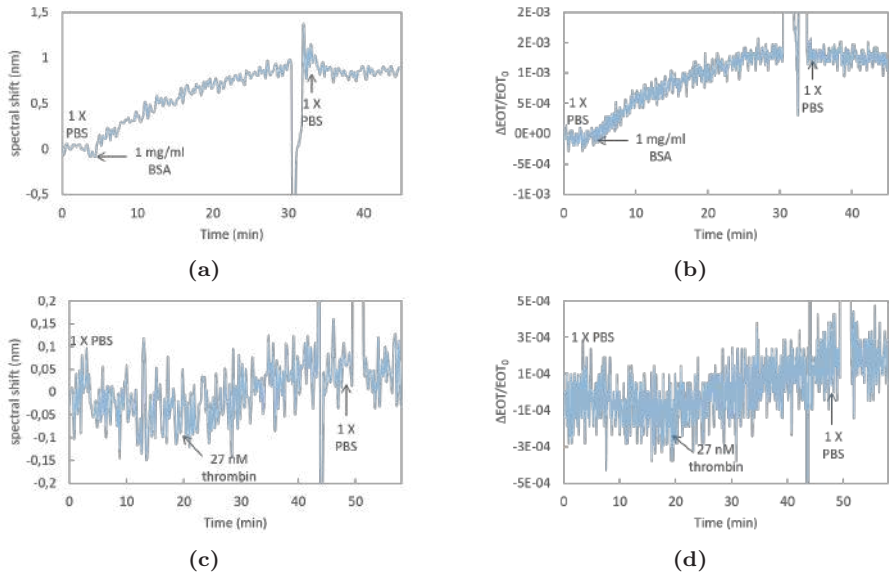

Figure 2.19. Experiment of thrombin biodetection using APTES-functionalised samples. Firstly, the surface was blocked with BSA, the sensogram is shown for (a) spectral shift and (b) EOT change analyses. Then, 27 nM thrombin was flowed and the sensing curve is shown for (c) spectral shift and (d) EOT change analyses.

Therefore, a different response was observed between hydrosilylated and oxidised samples, being the later less sensitive to both things: BSA and thrombin detection. Two factors were hypothesised to be responsible for such a difference: the thickness of the oxide and the APTES layers. When oxide layer grows, it occupies part of the pore, reducing the available volume to allow biomolecules to enter into the porous structure during biofunctionalisation and biodetection steps. Additionally, APTES can polymerise creating layers of several nanometres of thickness, which also reduces the available volume. A possible solution to this could be reducing APTES concentration, but best sensing results were obtained with 1 v/v% APTES solution.

According to these results, we abandoned the APTES-mediated biofunctionalisation and continued with hydrosilylation. However, although results were better in hydrosylilated samples than in oxidised ones, difficulties were found to replicate such results. Additionally, both the spectral shift and EOT change provoked by thrombin recognition were too small and the binding curve was extremely noisy, especially when thrombin is flowed, hardening the possible detection of lower concentrations of thrombin, as we aim at doing.

One possible reason to this low sensitivity of the biosensor is a bad biofunctionalisation of the surface and hence, a lack of bioreceptors. To asses whether this was the reason, Fourier Transform Infrared-Attenuated Total Reflectance (FTIR-ATR) spectroscopy measurements were performed.

2.6.4 FTIR-ATR characterisation of the biofunctionalisation process in hydrosilylated samples

FTIR-ATR spectroscopy relies on the total internal reflection of infrared radiations at the interface of two media. This physical phenomenon occurs when an infrared light beam travels from a material with a higher refractive index (the germanium tip of the equipment) to a lower refractive index material (the sample) with an incidence angle greater than the critical angle, resulting in an evanescent field in the interface that can be measured. When infrared active species are in the surface of the sample, a characteristic absorption peak can be observed in the spectrum. Each chemical bond absorbs at a certain wavelength, creating a unique signature that allows the identification of the different bonds created and broke during chemical reactions of biofunctionalisation.

The FTIR-ATR equipment employed in this work is Vertex 70V (Bruker, Billerica, MA, USA) working in the near-infrared region (NIR, from 1100 nm to 2500 nm) and using a KBr beam splitter and a Mercury-Cadmium-Telluride (MCT) detector. The ATR accessory employed has a germanium tip. Regarding measurement settings, the resolution was set at $4\,cm^{-1}$ and 1040 measurements were performed to obtain an ATR signal. Air was measured as the background signal.

In Figure 2.20 it is shown the different FTIR-ATR spectra of pSi along the functionalisation process. As-anodised, porous silicon presents characteristic peaks at $\sim 2080\,cm^{-1}$ and $\sim 2110\,cm^{-1}$ due to Si–H and Si–H_2 stretching vibrations, respectively. These peaks disappear after the hydrosilylation of

the sample. Then, peaks at $\sim$2850 cm^{-1} and $\sim$2920 cm^{-1} and a strong peak at $\sim$1090 cm^{-1} indicate the presence of CH_2 symmetric and asymmetric stretching, respectively. Also a strong peak at $\sim$1720 cm^{-1} is characteristic of carbonyl stretching. This peak disappears after the reaction with EDC/NHS and new peaks appear at $\sim$1815 cm^{-1}, $\sim$1785 cm^{-1} and $\sim$1742 cm^{-1} attributed to the succimidyl ester. Also N–O and C–O stretching modes appear at $\sim$1070 cm^{-1} and $\sim$1209 cm^{-1} [103]. Finally, after reaction of TBA, DNA characteristic bands should appear at $\sim$1688 cm^{-1}, related to carbonyl groups, and at $\sim$1230 cm^{-1}, related to phosphate groups [64]. However, this last step could not be clearly seen in our samples, indicating that only a small amount of TBA molecules might have bound to the pSi surface –since biodetection was observed. However the amount of aptamer on the surface should be small, what could explain the noise and the small spectral shift and EOT change observed while flowing thrombin.

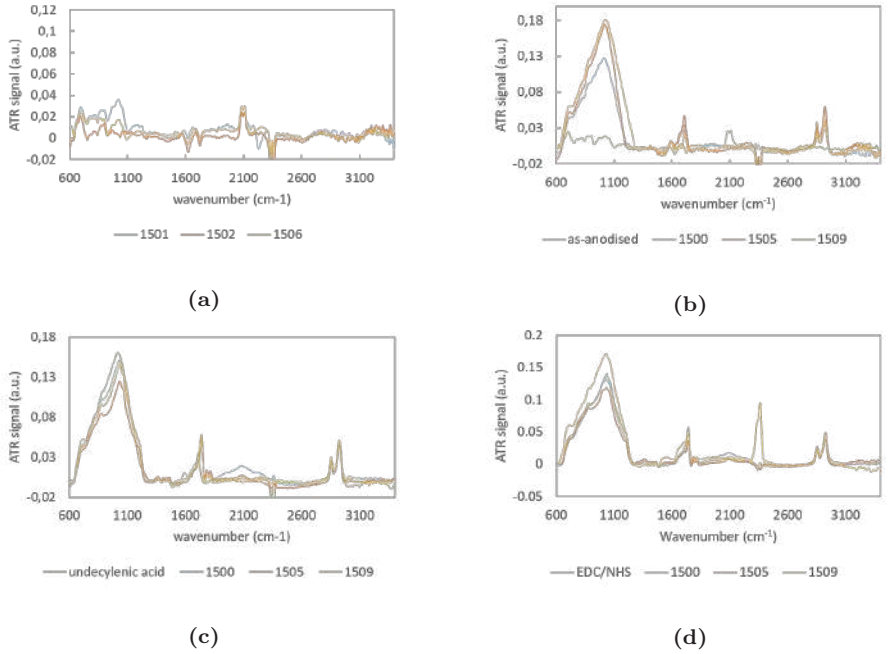

Figure 2.20. FTIR-ATR spectra of a pSi sample along the biofunctionalisation protocol: (a) as-anodised, (b) after thermal hydrosilylation, (c) reacting with EDC/NHS and (d) TBA reaction.

Considering that undecylenic acid endows the surface with an hydrophobic character that could be hindering the entrance of aqueous solutions, we tried to biofunctionalise the samples in flow to favour the entrance of liquids inside the pores. Additionally, the concentration of TBA was doubled up to 10 µM and BSA was replaced by Tris buffer in order to block the EDC/NHS activated carboxyl groups. Tris molecules are smaller than BSA ones, therefore, a smaller

reduction of the pore when the surface is cover by Tris is expected, favouring the entrance of thrombin molecules.

2.6.5 Real-time optical monitoring of biofunctionalisation and biodetection using hydrosilylated pSi samples

After carrying out the hydrosilylation of the sample (in bench), the flow cell was stuck on it. After calibration of the system, the sample with the flow cell was place in the goniometer and the biofunctionalisation process of the sample was monitored.

Firstly, the EDC/NHS solution was flowed over the sample after creating a stable baseline with DI water. Then, DI water was flowed again to remove the unreacted EDC and NHS molecules. A net shift of 1.95 nm and a EOT change of 1.32×10^{-2} was observed, indicating the successful reaction of EDC/NHS with the carboxyl groups on the pSi surface (see Figure 2.21).

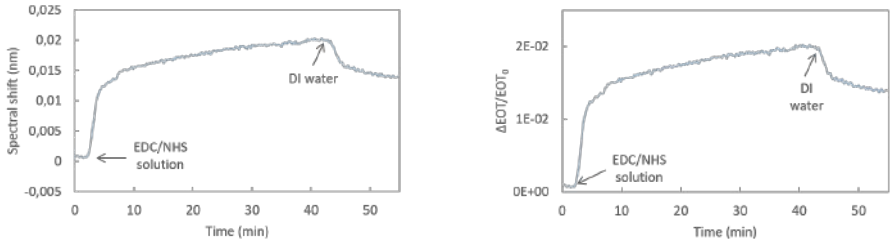

(a) **(b)**

Figure 2.21. Optical monitoring of EDC/NHS solution reacting with carboxyl groups present on the pSi surface. Sensograms of (a) spectral shift and (b) EOT change analyses are shown.

Once activated the carboxyl groups of the pSi surface, TBA was flowed at a concentration of 10 µM in a folding buffer composed of 1 X PBS and 1 mM $MgCl_2$. Previously to be flowed, TBA solution was heated at 95 °C for 5 min and then, allowed to cool down at room temperature for 20 min. In order to remove the unreacted TBA, 1 X PBS was flowed again. A net shift of 0.23 nm and an EOT change of 1.27×10^{-3} were observed (see Figure 2.22). The irregularities than can be observed while flowing 1 X PBS are due to a bubble in the middle of the channel.

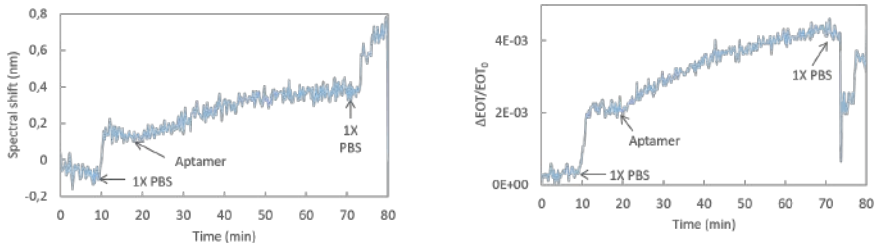

(a) **(b)**

Figure 2.22. Optical monitoring of TBA reacting with activated carboxyl groups present on the pSi surface. Sensograms of (a) spectral shift and (b) EOT change analyses are shown.

Finally, a 10 mM Tris solution in 1 X PBS was flowed to avoid the unspecific covalent attachment of the upcoming thrombin to pSi surface. A EOT change of 4.99×10^{-4} was observed, however a continuous drift of the spectral position was observed, what makes difficult quantifying the spectral shift (see Figure 2.23).

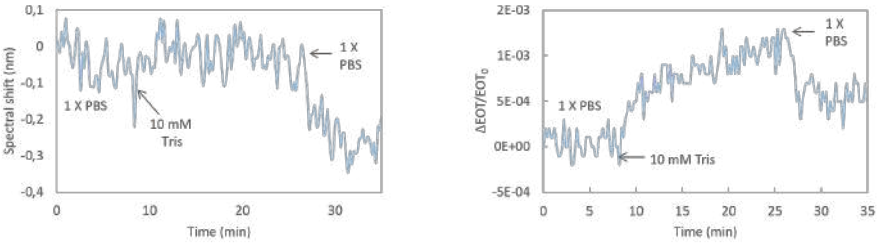

(a) **(b)**

Figure 2.23. Optical monitoring of Tris blocking of the pSi surface. Sensograms of (a) spectral shift and (b) EOT change analyses are shown.

Once demonstrated the correct biofunctionalisation of the pSi surface and its blocking, 27 nM thrombin (1 X PBS) was flowed to specifically detect it. A final net EOT change of $\sim 1.0 \times 10^{-3}$ was observed, which is the double than the change observed for in-bench biofunctionalised samples, indicating a little increase in sensitivity. However, when looking at the spectral shift, the shift observed after flowing thrombin solution is reversed after flowing 1 X PBS. This result could be indicating that the shift observed was only due to the higher refractive index of the thrombin solution compared to 1 X PBS solution and no recognition of thrombin by TBA occurred (see Figure 2.24). Therefore, we could not evince an improvement when in-flow biofunctionalisation is carried out and a higher concentration of TBA is employed.

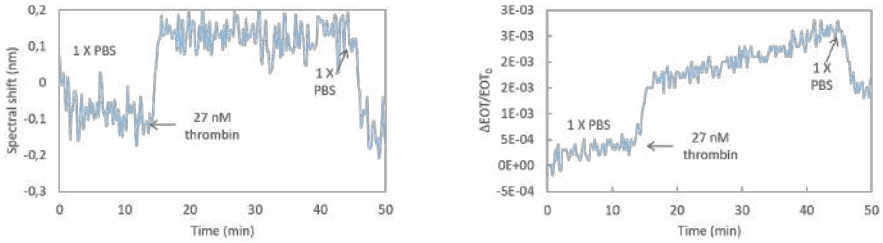

(a) **(b)**

Figure 2.24. Optical monitoring of TBA reacting with activated carboxyl groups present on the pSi surface. Sensograms of (a) spectral shift and (b) EOT change analyses are shown.

Several factors were hypothesised to be responsible for these bad results and lack of reproducibility:

- **Low reproducibility of pSi fabrication.** Although the fabrication parameters and the silicon wafers were always the same, it was observed that the optical response was not always reproducible between different samples. Indeed, the optical response was not homogeneous along the same surface, suggesting a different structure of pSi at different points. These different morphologies of pSi layers could affect the dynamics of the liquids flowed and hence, the result of the experiments. In order to improve the morphology –bigger pores and higher homogeneity– and the optical response –higher quality factor of the reflectance peaks–, different fabrication configurations were studied such as the creation and removal of a top parasitic layer [107], the use of different concentrations of HF and current densities or the use of aluminium instead of copper as the anode, but no significant improvements were achieved.

- **The pores are not big enough.** Although dehydrated aptamer and thrombin are expected to have a diameter of $\sim$1 nm and $\sim$5 nm, respectively, in aqueous solutions molecules of water and some other molecules that form the buffer tend to bind to the surface increasing its diameter. This is known as the hydrodynamic diameter. Therefore, although the pores diameter was $\sim$25 nm, if the molecules have a bigger hydrodynamic diameter than this value, they will not be able to go inside the pores. The diameter of the biomolecules in aqueous solution could be analysed by Dynamic Light Scattering (DLS) measurements. However, in the research centre there is not an available equipment to do it.

  This hypothesis could be supported by the work developed by Terracciano et al [108] in which they report the synthesis of TBA inside the pSi and the selective and reversible detection of thrombin at a concentration of 14 ± 8 nM when pores with a diameter of $>$50 nm are achieved.

- **No recognition of thrombin by TBA.** Maybe the recognition TBA-thrombin does not occur due to a bad conformation of the aptamer once attached to the surface or due to repulsions between molecules.

- **Functionalisation protocol not fully optimised.**

To study the suitability of the covalent strategy to attach TBA to a silicon surface and its capability to recognise and specifically bind TBA, alternative optical structures previously exploited for biosensing purposes in the group were employed: integrated PhC waveguides.

2.7 Thrombin detection employing integrated photonic crystal waveguides

In recent years, silicon has become the main material for the development of photonic technologies because of the outstanding features it shows compared with other materials such as InP, GaAs or $LiNbO_3$. Firstly, its cost effectiveness in complementary metal-oxide semiconductor (CMOS) fabrication procedures, improving the yield and hence, a large-scale production and integration. Secondly, the high refractive index contrast between Si (n=3.48) and SiO_2 (n=1.45) offers a strong optical confinement that allows the nanometric scaling of photonic devices and the observation of non-linear optical effects. Finally, silicon shows outstanding material properties such as high thermal conductivity, high optical damage threshold and third-order optical non-linearities and low attenuation optical losses from near to medium infrared (MIR) region [109, 110].

One of the main technologies in which silicon is employed is the development of integrated photonic circuits –consisting of complex photonic systems created by the combination of wavelength scale optical components– with application in different fields such as sensing, communications, medical applications or imaging, among others [111].

One of the commonly used photonic structures in the development of photonic integrated circuits are waveguides. They allow the propagation of light and serve as connectors between different photonic structures. In addition to their interconnecting role, waveguides can be engineered to create a periodic modulation of the effective refractive index of the structure by using a periodic pattern. To do that, one of the possibilities is placing periodic transversal elements to the main guide creating a corrugated waveguide. This results in a photonic crystal with a PBG in its optical response suitable for biosensing purposes (see Figure 2.25.a). Because of that, this structure is going to be employed in this study.

To monitor the biorecognition events during biosensing, variations in the PBG position are studied. When the analyte binds to the surface, a refractive index change occurs, changing the position of the cut-off wavelength of the transmitted spectrum. Ideally, such change is proportional to the concentration of the analyte and allows its quantification [112, 113] (see Figure 2.25.b).

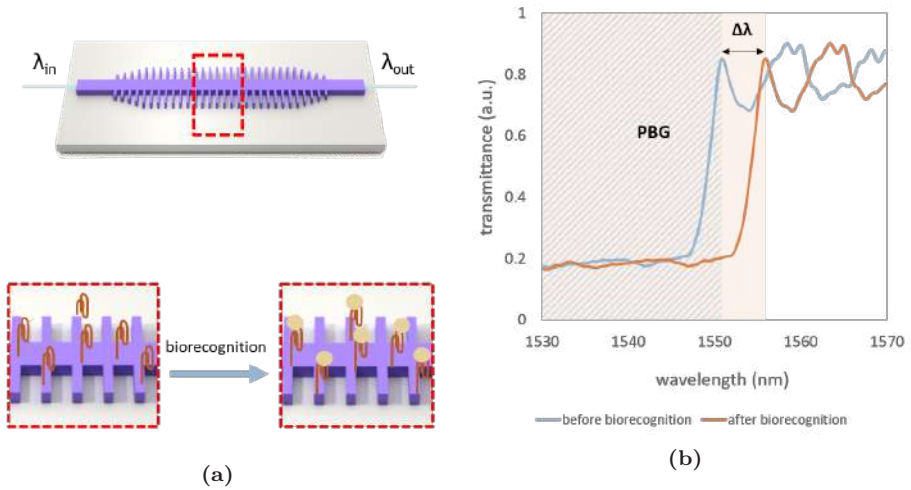

Figure 2.25. (a) Sketch of 1D PhC structure employed: a corrugated waveguide (top). For biosensing experiments, the surface of the PhC is biofunctionalised to carry out the specific biorecognition of the analyte (bottom). (b) Transmission spectrum of the corrugated waveguide in which a PBG –a range of wavelengths that cannot propagate– appears (blue striped area). When the biorecognition occurs, there is an increase of the refractive index that provokes a shift of the PBG edge ($\Delta\lambda$) towards longer wavelengths).

The employed 1D PhC corrugated waveguides were fabricated on a silicon-on-insulator (SOI) wafer employing e-beam lithography (EBL) and inductively coupled plasma (ICP) etching of the top silicon layer. The parameters of the 1D PhC structures are the following (see Figure 2.26.a): height (h) of 220 nm, width (w) of 460 nm, period (a) of 380 nm, transversal elements length (we) of 1500 nm, and four possible transversal elements widths (wi) of 140 nm, 120 nm, 100 nm and 80 nm. In order to improve light coupling to/from the 1D PhC structures and the input/output single mode waveguides (also with a width of 460 nm), a 5-element taper was included. These silicon integrated 1D PhC structures are highly compact –footprint below 50 μm^2– (see Figure 2.26.b), thus offering the opportunity to create arrays of sensors within the same photonic chip. Accordingly, in this work, we have designed a photonic chip containing 16 PhC sensing structures distributed in 4 groups (named G1, G2, G3, and G4, see Figure 2.26.c) of 4 PhC sensors, each one with a different wi parameter (see Figure 2.26.d). Besides the PhC sensors groups, alignment reference waveguides were also included in the chip. All the photonic structures within the chip were accessed at the input and the output via 70 −nm-deep shallow etched 1D grating couplers.

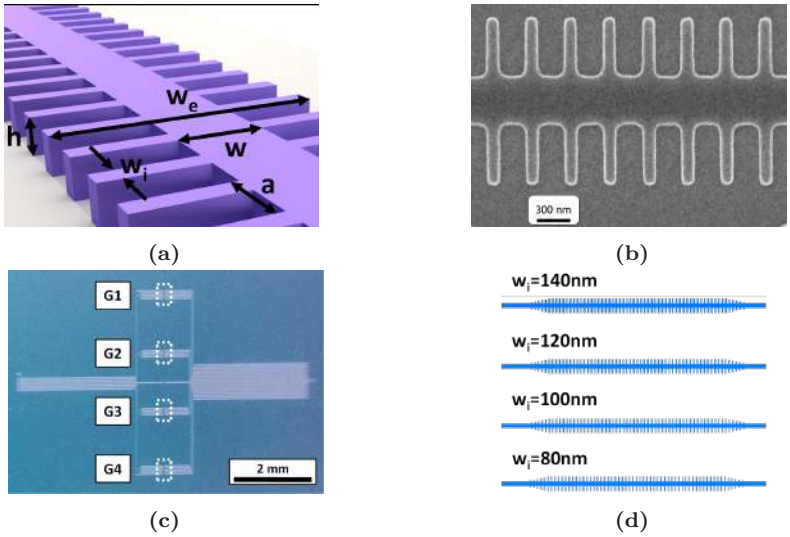

Figure 2.26. (a) Sketch of the 1D PhC structure showing its main parameters. (b)SEM image of one of the fabricated 1D PhC sensing structures. (c) Image of the fabricated photonic chip, in which the different groups of 1D PhC sensing structures are indicated. (d) Distribution of the 1D PhC structures within each sensors group.

For the interrogation of the optical structures, a wavelength-tunable laser (81980A, Keysight, Santa Rosa, CA, USA) is employed. It is coupled to the input grating couplers of the chip through a fibre aspheric collimator (CFS2-1550-APC, Thorlabs, Newton, NJ, USA). The output light from the chip is collected by a 20X objective (Plan Achromat N.A. 0.4, Olympus, Shinjuku, Japan) connected to an infrared camera (Xeva-1.7-320, Xenics, Heverlee, Belgium). All these devices are controlled using a software implemented in LabVIEW (2014 SP1, National Instruments, Austin, TX, USA) (see Figure 2.27).

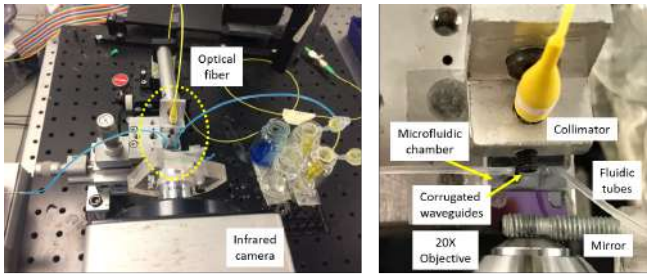

Figure 2.27. Optical setup employed for the characterisation and the real-time measurements in flow using corrugated waveguides (left). The microfluidic cell is highlighted with a yellow circle. A more detailed picture of the microfluidic cell mounted on the chip is also shown (right).

2.7.1 Biofunctionalisation strategy

SOI technology employed for the fabrication of PhC corrugated waveguides results in a PhC structure made on silicon and a substrate over which it lies made on silica. In order to perform the hydrosilylation of the PhC, it should be exposed to an HF solution to remove the native oxide layer that is formed over the silicon waveguide. However, it would also remove part of the silica of the substrate, what could affect the confinement of light in the structure and its optical response. Because of that, the covalent attachment of TBA to the surface to test its recognition capability was performed by silanisation of the surface with APTES and the use of glutaraldehyde as a crosslinking molecule.

In order to clean and activate the silicon surface of the PhC structures, the chip is immersed in piranha solution (H_2SO_4:H_2O_2, 3:1) at 100 °C for 30 min, rinsed with DI water, and dried with nitrogen. Afterwards, to perform the surface silanisation, the chip was immersed in 1 % APTES solution in 95 % ethanol aqueous solution at 70 °C for 1 hour. Then, it was rinsed three times with 95 % ethanol and IPA, rinsed with DI water, dried with nitrogen, and cured for 15 min at 110 °C. Once silanised, the chip was immersed in a 2.5 % glutaraldehyde solution in 1 X PBS for 1 h at room temperature and then rinsed three times with 1 X PBS and dried with compressed air. Finally, 5 µM TBA in folding buffer (1 X PBS, 1 mM $MgCl_2$) was dropped on the PhC structures and allowed to react for 4 hour at room temperature in humid atmosphere. Then, the chip was placed at 4 °C overnight. After incubation, the chip was rinsed with 1 X PBS three times to remove the excess of TBA, dried with compressed air, and stored at 4 °C until use. Aptamers were pre-folded before incubation on the surface by heating the 5 µM TBA solution in folding buffer at 95 °C for 5 min and then allowing it to cool down at room temperature.

2.7.2 Detection of thrombin increasing concentrations

To perform the in-flow biodetection experiments, a microfluidic chamber is assembled on the chip. Such microfluidic chamber consists of a PMMA piece and a double-sided adhesive tape with an open area on it (250 µm height, 8 mm length and 500 µm width). To assemble the fluidic system, the adhesive tape is glued on top of the silicon chip so that its open area covers the PhC structures. Then, the PMMA piece with inlet and outlet tubing were properly attached to the adhesive tape in order to create a channel to flow liquids over the PhC sensors. For pumping, a syringe pump working in withdraw mode was connected to the outlet tube and set at a constant rate of 20 µL min^{-1}.

In order to analyse the data obtained in the experiments, MATLAB software was used. First, FFT was applied to raw data. Then, inverse FFT was performed to data whose frequencies are located under a normalised cutoff frequency of 0.02. Once the original data is filtered, the local maximum transmission peak at the end of the PBG was located and fitted with a Gaussian function in order to determine its central position with a higher accuracy. This procedure was

carried out automatically for all the spectra acquired during the experiments in order to determine the shift of the PBG edge.

We began trying to demonstrate the detection of a thrombin concentration of 27 nM (1 µg mL^{-1}), a value that is near the upper concentration of the initiation phase [70]. To this aim, the surface of the PhC sensing structures in the chip was biofunctionalised as described in Section 2.7.1. Then, the microfluidic cell was attached to the photonic chip and the optical response of each sensing structure was checked while flowing 1 X PBS.

In the employed chip (hereafter referred as experimental chip), only PhC sensors groups G1 and G3 had an acceptable transmission spectrum and were considered in the experiment. From these two PhC groups, only the sensing response of the PhC structures with wi values 140 nm and 120 nm were monitored as their PBG edges were in the working wavelength range of the laser (from 1520 nm to 1630 nm) and had a well-defined edge shape (see Figure 2.28). Hereafter, the monitored PBG edges from PhCs group G1 will be referred as G1-1 (wi = 140 nm) and G1-2 (wi = 120 nm) and those from PhCs group G3 will be referred as G3-1 (wi = 140 nm) and G3-2 (wi = 120 nm). While flowing 1 X PBS, the noise of the set-up was also characterised and a value of 8.9 pm was obtained.

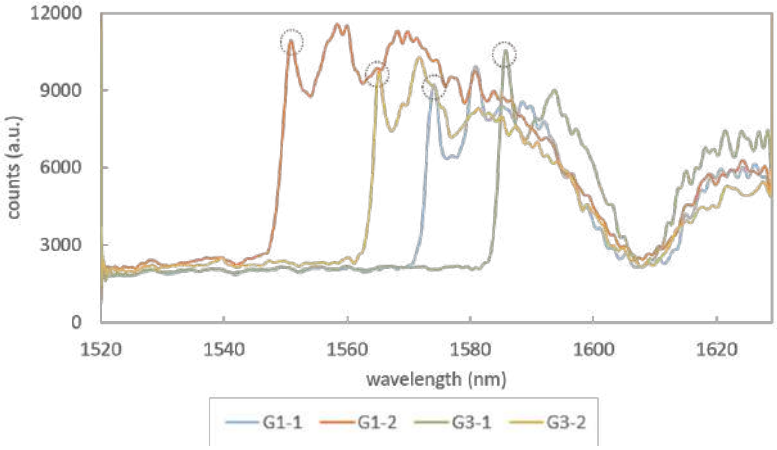

Figure 2.28. Transmission spectra of the four PhC structures being monitored. The circles indicate the PBG edge, where a local maximum transmission is observed and whose spectral position will be monitored during biosensing experiments. Counts refer to the digital values provided by the 14-bit analogue to digital converter (ADC) of the infrared camera. The dip at ∼1608 nm indicates the minimum for the response of the access grating couplers.

Prior to thrombin detection, a blocking solution (BS) of 1 mg ml^{-1} BSA in 1 X PBS was flowed for 30 min to block the remaining reactive sites of glutaraldehyde on the surface (hereafter this process will be referred to as blocking). Afterwards,

in order to check that the surface is completely blocked and no unspecific recognition by TBA occurs, a solution of 18 nM (1 µg mL^{-1}) streptavidin in BS was flowed. When the streptavidin solution is flowed over the photonic chip, no changes occur in the position of the PBG edges, thus confirming that streptavidin is neither binding to the aptamers nor adsorbing to the surface (see Figure 2.29).

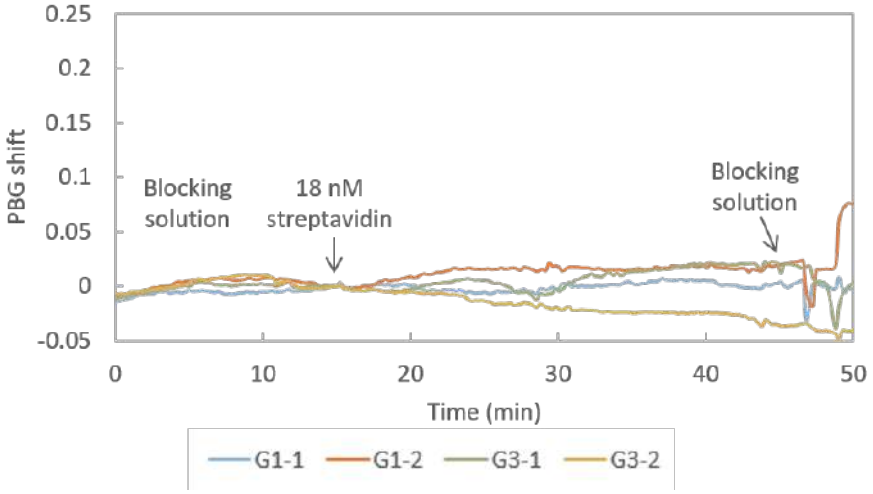

Figure 2.29. To test the recognition specificity, 18 nM streptavidin in blocking solution (BS) was flowed over the TBA-functionalised photonic chip. In minute 15, after establishing a baseline with BS, the streptavidin solution was injected and no change related to detection was observed, confirming that the surface was totally blocked and no unspecific recognition occurred.

Once the lack of unspecific recognition was demonstrated, the BS was flowed again. When a stable baseline (i.e., centred in zero for at least 2 min and with a standard deviation below setup noise) was achieved, a solution of 27 nM thrombin in BS was flowed over the PhC structures. As shown in Figure 2.30, a shift of PBG edges towards longer wavelengths was produced, indicating the binding of thrombin to the aptamers on the surface. Finally, BS was flowed again to remove the excess of thrombin. The average net shift of G1-1 and G1-2 was 97 pm, whereas the average net shift of G3-1 and G3-2 was 166 pm. The differences between PhCs groups can be attributed to two factors. First, a different density of bioreceptors on their surface [51, 114]. The biofunctionalisation process is carried out manually, which might imply errors related to the manipulation of the materials employed, humidity, and temperature changes of the room and the precision when dropping the TBA solution over the PhC structures. Second, slight structural differences between PhCs groups are also expected due to the inherent limitations of EBL technique when fabricating the smallest features of the photonic chip [115]. These structural differences might be influencing the optical response of the PhC structures and their sensitivity.

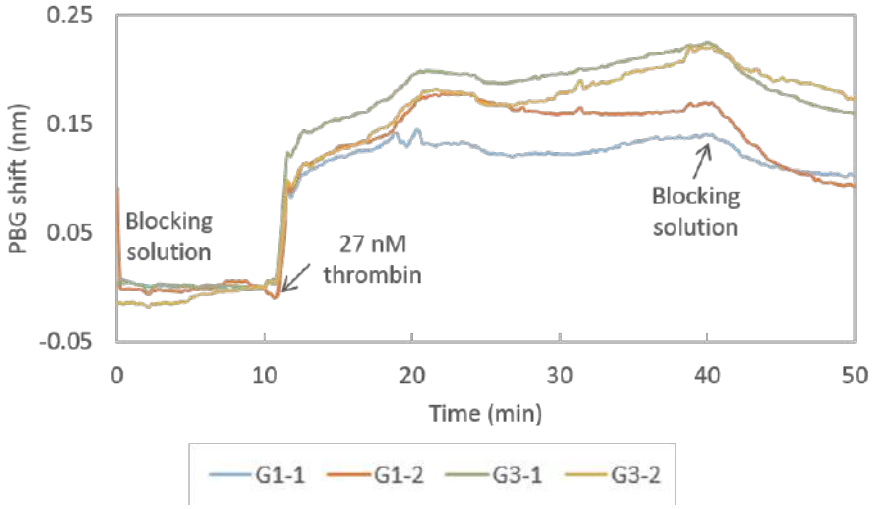

Figure 2.30. Sensing response of the PhC sensing structures when a 27 nM thrombin solution is flowed. At minute 10, 27 nM thrombin in BS was flowed and its binding to TBA on the surface was clearly observed. At minute 40, BS was flowed again to remove the excess of thrombin. An average spectral shift of 97 pm and 166 pm was observed for the structures from groups G1 and G3, respectively. The bumps that appear while flowing 27 nM thrombin are ascribed to fluidic irregularities.

After this experiment, a negative control assay was performed to check unspecific adsorption of thrombin on the sensor surface. In parallel to the biofunctionalisation of the experimental chip, another chip with the same characteristics (hereafter referred as control chip) was biofunctionalised using the same protocol, except that only PhCs groups G1 and G2 are incubated with TBA while PhCs groups G3 and G4 are incubated just with folding buffer (control groups). As in the previous experiment, the microfluidic flow cell was assembled on the photonic chip and the PBG edges monitored were G1-1, G1-2, G3-1, and G3-2.

As in the previous experiment, PhCs surfaces were blocked by flowing BS first. Once a stable baseline was obtained for BS, 27 nM thrombin in BS was introduced. As it can be observed in Figure 2.31, only those PhC structures with the TBA immobilised on their surface exhibited a change in their PBG position when thrombin was flowed (an average net shift of 119 pm was observed), while no response was observed for those PhC structures on which the bioreceptors are not present, thus confirming that unspecific adsorption was not produced. Regarding the small peak observed when thrombin gets to the control PhC structures, it indicates a refractive index increase attributed to flowing irregularities provoked by the contrast of densities of the solutions being exchanged in the fluidic chamber; once the new solution replaces the previous one and the flow regime is recovered, the PBG edges position is also recovered [116, 117].

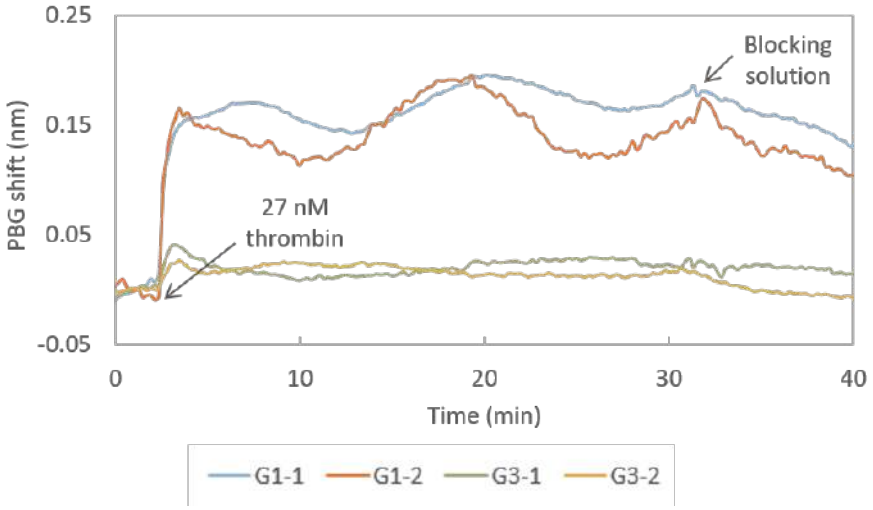

Figure 2.31. Sensing response obtained when flowing a 27 nM thrombin solution over a photonic chip where only half of their PhC structures have TBA on their surface (G1-1 and G1-2). Only the PBG edges of such PhC structures experienced an average shift of 119 pm, whereas control PhC structures (G3-1 and G3-2, without TBA) did not experience any sensing change. This confirms the recognition specificity. Regarding the instability of G1-1 and G1-2 while thrombin was flowed, it was again attributed to fluidic irregularities.

Once it was demonstrated that the optical aptasensor was able to specifically detect a thrombin concentration as low as 27 nM, the next objective was to detect a thrombin concentration near the lower concentration limit of the initiation phase (i.e., ∼1 nM). With this aim, the experimental chip was regenerated and biofunctionalised again using the protocol explained in Section 2.7.1.

Regeneration of the PhC structures consists in removing the biolayer created on them to create a new functional one. For such aim, the chip was immersed in piranha solution (see Section 2.7.1) for 30 min, rinsed with DI water and dried with nitrogen. Then the chip was rinsed with acetone and IPA, dried with nitrogen and exposed to O_2 plasma for 10 min. Finally, the chip was exposed to vapour of 16 % HF aqueous solution for 7 s, rinsed with DI water, dried with nitrogen and stored in desiccator until being biofunctionalised again following the protocol of Section 2.7.1.

Figure 2.32 shows the sensing results obtained when a 2.7 nM thrombin solution in BS is flowed over the photonic sensing chip (a ten-fold lower concentration with respect to previous experiments). Note that the thrombin was clearly detected despite its low concentration, providing average net shifts of 39 pm and 30 pm for PhCs groups G1 and G3, respectively. In this occasion, differences between PhCs groups are mainly due to the slightly higher desorption observed for G3-1 when BS is flowed again. As the photonic chip and the

microfluidic chamber are the same employed for the detection of 27 nM thrombin solution, this different behaviour can be ascribed to heterogeneities in the manually performed biofunctionalisation process, as previously explained.

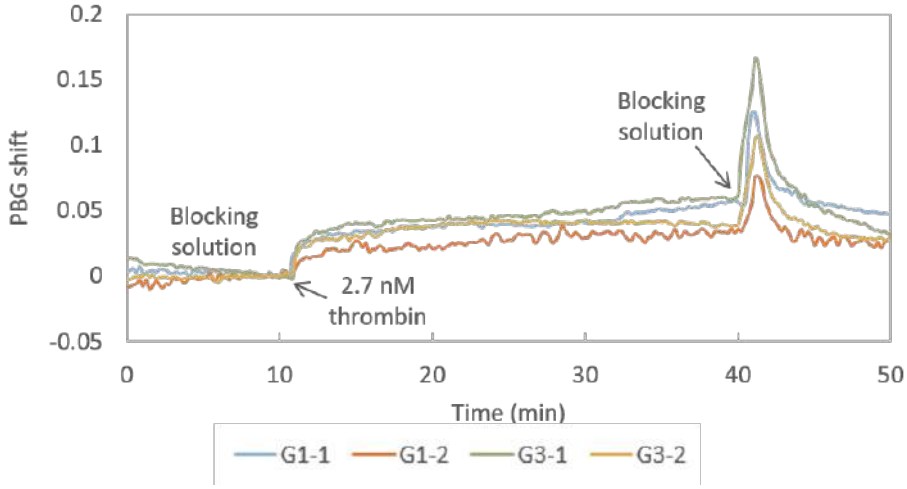

Figure 2.32. Sensing response of the PhC-sensing structures when a 2.7 nM thrombin solution is flowed. At minute 10, 2.7 nM thrombin solution in BS was flowed and its binding to TBA on the surface was clearly observed. At minute 40, BS was flowed again to remove the excess of thrombin. The sudden peak observed is a refractive index increase due to different densities of the two solutions being exchanged in the fluidic chamber, as previously observed in Figure 2.31. Note that now the structure G1-2 corresponds to the 1D PhC with wi of 100 nm from group G1.

At this point, the capability of the optical aptasensor to specifically detect thrombin at concentrations as low as those observed during the initiation phase of the thrombin generation process had been demonstrated. The goal of the following assay was assessing its capability to do this in a continuous way when the concentration is constantly increasing. With this aim, ten-fold serial dilutions of an initial 27 nM thrombin solution in BS were flowed over a photonic chip functionalised as explained in Section 2.7.1. As in previous assays, the PBG edges monitored were from PhCs group G1 (G1-1 and G1-2) and PhCs group G3 (G3-1 and G3-2). Figure 2.33 shows the experimental results obtained when increasing concentrations of thrombin were flowed over the photonic sensing chip. In Figure 2.33.a, the evolution of the wavelength position of G1-1 and G1-2 is shown. An average shift of 12 pm, 24 pm, and 52 pm was observed when flowing 270 pM, 2.7 nM, and 27 nM thrombin solutions, respectively (see details in Figure 2.33.c-f). No change in the position of those PBG edges was observed when 27 pM thrombin solution was flowed. Regarding G3-1 and G3-2, they experienced an average shift of 12 pm, 22 pm, and 44 pm in presence of 270 pM, 2.7 nM, and 27 nM thrombin solutions, respectively (see detail in Figure 2.33.c-f).

These PBG edges did not change their position when flowing 27 pM thrombin solution either. It is important to remark that the response of both PhCs groups was very similar in this assay, which indicates a good homogeneity regarding the optical behaviour, the bioreceptor density on sensing structures and the transport of analyte from bulk solution to the sensors surface. Nevertheless, although a binding curve can be observed when a concentration as low as 270 pM is flowed, the SNR of this sensing step is close to 1 –considering a calculated noise floor of 13 pm–, which indicates that the discrimination of the signal from the noise can be hard and suggesting the necessity of optimisation of the biosensing platform. Either way, this aptasensor showed a promising response to increasing thrombin concentrations in a range that would allow to monitor the initiation phase of the thrombin generation process in real-time.

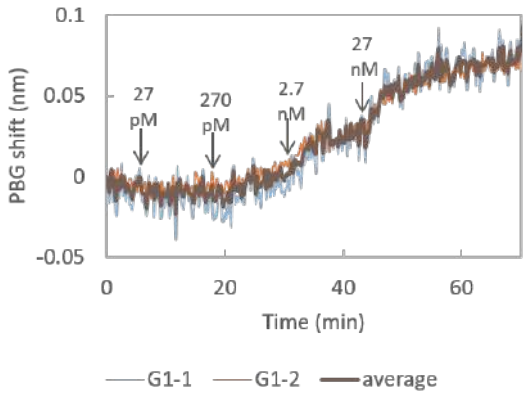

(a)

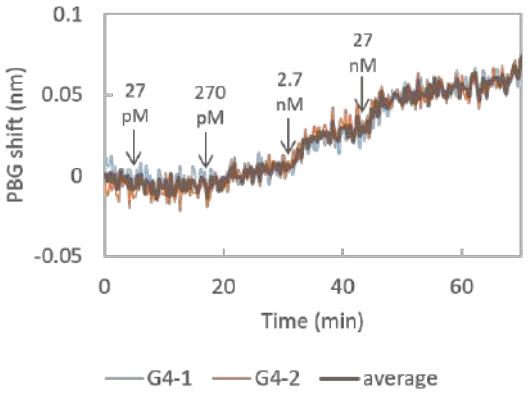

(b)

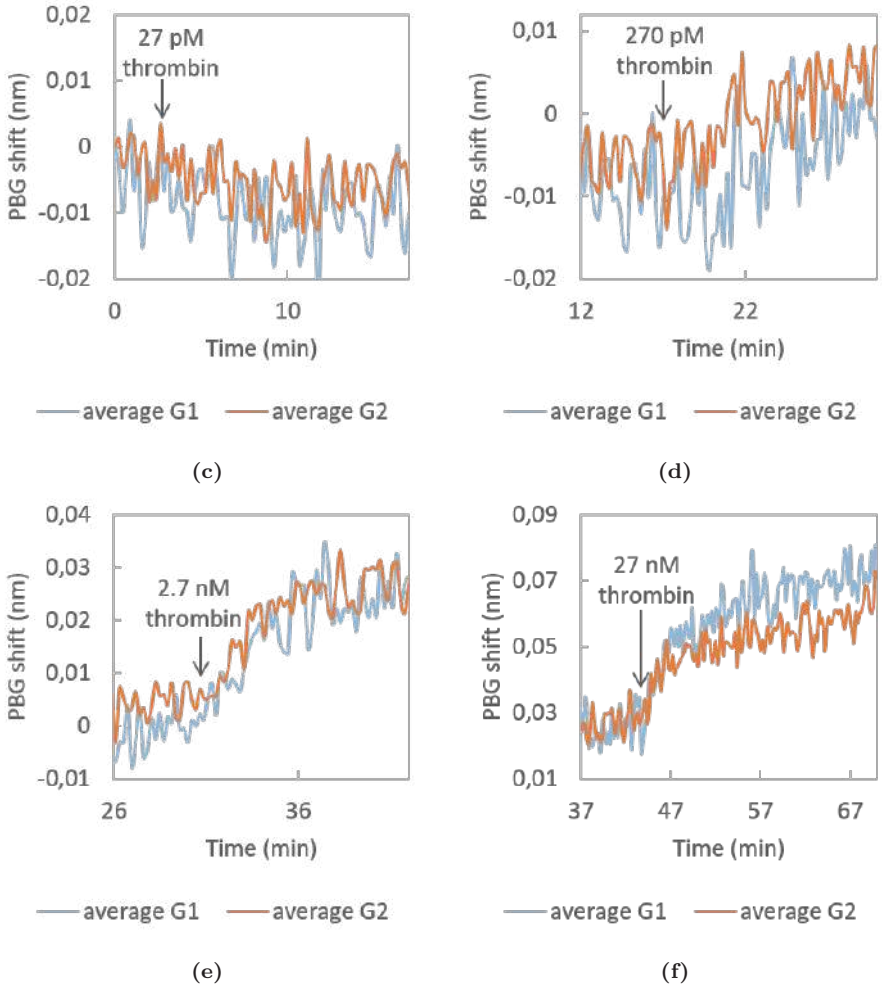

Figure 2.33. Resonance shift experienced by PhCs groups G1 and G3 when increasing concentrations of thrombin were consecutively flowed over time. (a) Shift experienced by PhCs group G1 and their average shift. (b) Shift experienced by PhCs group G3 and their average shift. (c) 27 pM thrombin solution was not detected neither by PhCs group G1 nor by group G3. (d) 270 pM thrombin solution provoked an average PBG shift of 12 pm for both PhCs groups. (e) 2.7 nM thrombin solution provoked an average PBG shift of 24 pm and 22 pm for PhCs groups G1 and G3, respectively. (f) 27 nM thrombin solution provoked an average PBG shift of 52 pm and 44 pm for PhCs groups G1 and G3, respectively.

It is also remarkable that these results were consistent to those obtained from previous detection assays of discrete concentrations. In this assay, when flowing 2.7 nM thrombin, the average total net shift showed by PhCs group G1 is

36 pm and by PhCs group G3 is 34 pm, similar to those observed in Figure 2.32 (39 pm and 30 pm, respectively). When flowing 27 nM, PhCs group G1 showed an average total net shift of 88 pm, which is also very similar to that observed in Figure 2.30 (97 pm). Only PhCs group G3 showed an average total net shift notably different from that observed in Figure 2.30 (78 pm vs. 166 pm). This difference is attributed to the different density of bioreceptors on the surface of PhCs group G3 when only the detection of 27 nM thrombin was performed, as previously discussed then.

2.8 Conclusions

In this chapter, it was developed an aptasensor capable of detecting thrombin at concentrations in the nanomolar range –characteristic of the initiation phase of the coagulation cascade– in real time without using labels.

According to the high bulk sensitivity showed by pSi in previous works developed by the Biophotonics group of Nanophotonics Technology Center – Caroselli et al. reported a sensitivity of 1000 nm RIU^{-1} [97]–, pSi was expected to be a good candidate for the development of a thrombin aptasensor. In this chapter, it was demonstrated that TBA –a good candidate for the biodetection of thrombin– can be attached to the pSi surface by, at least, two chemical approaches: hydrosilylation and APTES-mediated biofunctionalisation. Depending on which one is employed, the final performance of the biosensor is conditioned, being more sensitive those prepared by hydrosilylation. This could be explained by the reduction of the pore diameter experienced after the oxidation and the APTES silanisation steps, thus hardening the entering of the target solutions inside the pores.

The correct biofunctionalisation of hydrosilylated samples was demonstrated by flowing the reagents and measuring in real time the optical changes provoked by the reactions. However, a low efficiency of them and hence, a low density of bioreceptors in the pSi surface was reported according to FTIR-ATR measurements. This could explain the fact that only the upper limit concentration of the initiation phase of the coagulation cascade (27 nM) could be detected.

In order to study if this low efficiency was due to the porous structure or to limitations in the biofunctionalisation protocol and TBA functionality, PhC structures were employed. They demonstrated a better sensing performance, being able to detect concentrations of thrombin ranging from 270 pM to 27 nM, thereby covering the nanomolar range corresponding to the initiation phase of thrombin generation that other thrombin generation assays cannot afford [Wolberg2008]. Additionally, they also showed the capability of differentiating between different concentrations when they are continuously flowed. Other groups have published similar label-free assays to detect increasing concentrations of thrombin, but the detected ones were higher than those detected in this Thesis [118–120], which indicates that the system presented here has a better sensitivity. On the other hand, other groups published the detection of similar thrombin concentrations but employing dyes, long incubation times and without the

possibility of monitoring the recognition of thrombin by TBA while it occurs [80, 81].

According to these results, the most limiting factor seemed to be the porous structure of pSi. Such porous structure not only conditions the optical response of the final biosensor, but also the hydrodynamics when entering the pores of the different solutions employed for biofunctionalisation and biodetection and, as a result, the outcome of both processes. Therefore, big efforts have to be made to get an adequate morphology of pSi depending on the final application of the biosensor. According to the work of Arshavsky Graham et al. [121], porous diameter and layer thickness are the most critical parameters to use pSi monolayers in sensing purposes: during biorecognition the binding rate decreases as the thickness increases and the pore diameter is reduced. Indeed, most of the pSi-based biosensors present a pore diameter of, at least, 50 nm [63, 64, 122]. However, in this Thesis pores bigger than 30 nm could not be obtained, although we tried to replicate the fabrication protocol of previously published works. Consequently, the main limitation of our work could have been the diameter of the pores. Although initially a pore diameter of 20 nm to 30 nm was estimated to be enough, it seems it is not. We will keep on working in this issue.

Chapter 3

Electrospun polymeric nanofibres

3.1 Introduction

Nanofibres (NFs) are fibres with a nanometre scale diameter typically synthesised by electrospinning. This fabrication technique appeared in the late 20^{th} century and has become a well-developed, versatile, and efficient method that requires a relatively inexpensive setup [123]. Electrospinning allows the fabrication of low-cost and complex electrospun layers with a highly-porous 3D network from a wide diversity of polymers [61] and at a large scale if properly configured [124, 125].

Polymeric NFs layers are nanostructured materials with a high surface-to-volume ratio, which has attracted great attention for their use in the development of technologies where a large surface area is required [126–129], such as tissue engineering scaffolds, filtration or biosensors [61, 130], among others. There are several examples of such NFs biosensors based on colorimetric [131], electrical [132] or potentiometric [133] measurements. However, any polymeric NFs layer had been previously employed for the development of a label-free optical biosensor.

Therefore, the aim of this chapter will be the development of a label-free optical biosensor based on NFs layers. Such work was framed in the OPTONANOSENS project: a national-funded project aiming at developing an optical biosensor based on NFs layers for the label-free and real-time detection of biological threats in a chemical, biological, radiological and nuclear (CBRN) attack.

Bioterrorism agents are pathogenic organisms or biological toxins that can lead to the onset of diseases, or even death, in animals or humans just several minutes after their spread through air, food or water. Due to the channels employed for their dissemination, they can be spread fast and affect a vast number of individuals from a population, being difficult to detect and control. Because of that, they are a commonly-employed agents for terrorism. During last 100 years, several bioterrorism events have been experienced by the population [134] and new outbreaks of bioterrorism agents could happen anytime. Accordingly, the development of a device for a fast and reliable detection of bioterrorism agents is essential to achieve a faster treatment of affected people and control the spread preventing further damages. In this sense, biosensors could play a central role.

Bioterrorism agents can be classified according to the risk they present in [135]:

- Category A: Biological agents easily transmitted, causing a high morbidity and mortality. They lead to the onset of illnesses, such as botulism (caused

by *Clostridium botulinum*), anthrax (produced by *Bacillus anthracis*) or bubonic plague (caused by *Yersinia pestis*), among others.

- Category B: Biological agents with a more difficult transmission and causing a lower morbidity and mortality such as ricin (from *Ricinus communis*) and abrin toxin (from *Abrus precatorius*) or food bacteria (*Escherichia coli O157: H7*, *Salmonella*), among others.

- Category C: Emerging pathogens and biological agents that can be engineered for a massive dispersion causing significant morbidity and mortality, such as H1N1 influenza, hantavirus, HIV/AIDS, Nipah virus or SARS.

In OPTONANOSENS, the goal was detecting a protein toxin of category B: ricin. However, the use of bioterrorism agents to develop and optimise a detection system, such as a biosensor, involves several infection risks for the researchers. Because of that, for the initial development, biological warfare agent simulants (BWAS) are employed. They are harmless biomolecules or agents with a high similarity in their size, shape and inner structures to the bioterrorism agents [136]. For target protein toxins, such as those aiming to detect in OPTONANOSENS, a widely recognised BWAS is bovine serum albumin (BSA). Therefore, the first development and optimisation of the biosensor will be carried out with a versatile biofunctionalisation process with antibodies recognising BSA.

In a nutshell, OPTONANOSENS aims at developing a new optical biosensor based on NFs for the specific and label-free detection of protein toxins. For such aim, the development of a suitable transducer consisting of a NFs layer, the optimisation of a versatile biofunctionalisation protocol of the NFs surface and optical biosensing experiments for the detection of BSA must be carried out. Finally, validation with real samples of protein toxins should be performed.

This project was carried out in collaboration with Tecnalia, responsible for the synthesis of NFs layers, and Instituto Nacional de Técnica Aeroespacial (INTA)-Campus "La Marañosa" of the Spanish Defence Ministry, responsible for the development of biofunctionalisation strategies and validation with real samples of ricin. NTC was responsible for the design and characterisation of NFs layers and the optical measurements of biofunctionalisation and biodetection experiments employing such NFs layers.

3.2 NFs synthesis and optical characterisation

The final optical response of a NFs layer is conditioned by the NFs layer morphology itself. Since it is a porous monolayer, from a photonic point of view it can be regarded as a Fabry-Pérot (FP) cavity, as previously employed pSi monolayers. Therefore, optical response can be also predicted by the Equation 2.8, in which the essential parameters of the NFs layer are the effective refractive index –dependent on the refractive index of the NFs and the medium, as explained in Equation 2.9– and the thickness of the layer.

Regarding the refractive index of the NFs, most of the typically employed polymers for their synthesis, such as polycarbonate (PC), polystyrene (PS) and polyamide 6 (PA6), have a refractive index of around 1.5 [137]. Hence, this is not a decisive factor to chose a certain material to obtain a NFs layer with a certain optical response. However, depending on the material, a different diameter of the NFs can be achieved, and this do have an important impact in the optical response. In order to behave like an homogeneous medium for light, NFs diameter must be smaller enough than the wavelength of the light source employed for the interrogation. To reduce costs, a visible light source was decided to be used for such aim, avoiding expensive lasers working in the infrared region. Therefore, NFs diameter must be around few tens of nanometres. According to bibliography, PC and PS allow the creation of NFs with a diameter ranging from hundreds of nanometers to some microns [138, 139], whilst PA6 allows the fabrication of NFs with diameters smaller than 100 nm [140]. Considering this, PA6 was chosen as the polymer to create NFs layers.

Once defined the optimum diameter of nanofibres and the polymer to use, several electrospinning parameters affecting the resulting morphology of NFs should be optimised. Among them: percentage of polymer, the need of adding salts to increase conductivity of the electrospinning solution or the applied voltage. To evaluate the effect of each one of these parameters, Scanning Electron Microscope (SEM) images and reflectivity measurements were employed.

In order to obtain such a small diameter of the NFs, a low concentration of the polymer must be used. However, it is well known that a low concentration of polymer provokes the appearance of beads in the NFs [141] that could affect the optical response. Therefore, to increase the conductivity of the polymer solution and reduce the appearance of beads, different salts were added to the solution. Different concentrations of PA6 solutions ranging from 6 wt% to 11 wt% and three salts –tetrabutylammonium chloride (TBAC), potassium formate and pyridine– were studied. The solutions were prepared with a solvent consisting of a 2:1 mixture of acetic and formic acid and were stirred for 60 min at 80 °C. Afterwards, electrospinning was carried out over polished silicon wafers. For such aim, the equipment employed was NS LAB 500 (El marco, Liberec, Czech Republic), which is available in Tecnalia, where the NFs deposition was carried out. Deposition time and distance between the roller and the ground electrodes were fixed at 20 min and 170 mm, respectively. The applied voltage was varied between 60 kV and 75 kV, depending on the conductivity of the electrospinning solution. The environmental conditions were 19 ± 2°C and a relative humidity of 40 ± 5%.

According to SEM images, the thinner NFs diameters were obtained with the solution of 6 wt% PA6 and 5 wt% pyridine salt (see Figure 3.1.a). In this NFs layers, no counts were observed, compared to NFs synthesised without salts (see Figure 3.1.b), and a diameter from 22 to 40nm was obtained. A porosity of >80% was estimated (see Figure 3.1.c).

Once obtained a diameter that suited the theoretical dimensions to obtain a FP cavity response, the optical characterisation of the structure and an analysis of its behaviour while flowing solutions were carried out. It was employed the

same goniometer and flow cell used in Section 2.6.3 to characterise the optical response and deliver the solutions to the NFs layer, respectively.

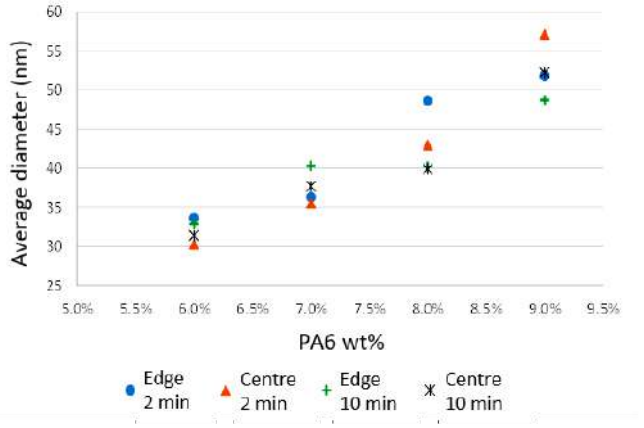

(a)

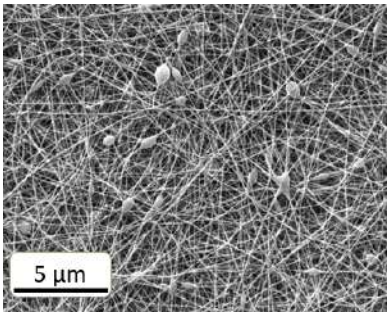

(b)

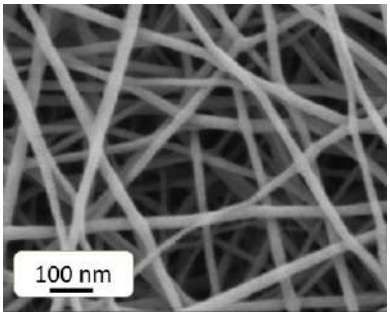

(c)

Figure 3.1. (a) Average diameter of the nanofibres (NFs) prepared with different concentrations of polyamyde 6 (PA6). (b) SEM image of a NFs layer prepared with 10 wt% PA6 without salt added. Beads can be clearly observed along NFs. (c) SEM image of a NFs layer prepared with 6 wt% PA6 and 5 wt% pyridine salt. The addition of salt increases the conductivity of the polymer solution and avoids the formation of beads.

As it can be observed in Figure 3.2.a, a FP cavity response is observed in absence of water (initial spectrum). Such response is maintained when water is flowed over the sample, but a decrease in the peak-to-peak amplitude is observed. This is due to the fact that the refractive index contrast between air and PA6 is bigger than that between water and PA6.

The loss of peak-to-peak amplitude in aqueous media is a problem to monitor in real-time the change of the spectral position of the reflectance peaks during biofunctionalisation and biodetection experiments. Therefore, the amplitude

must be increased to easily follow the peaks. For such aim, gold was evaporated by sputtering on the NFs layer. Different evaporation times were studied to get different thicknesses (1, 3 and 6 nm) of gold layers to obtain the optimal one. As it can be seen in Figure 3.2.b, the presence of a gold layer increases the peak-to-peak amplitude. The best response was obtained with 3-nm-thick gold layer, since a thinner and a thicker layer result in a lower and a similar peak-to-peak amplitude, respectively.

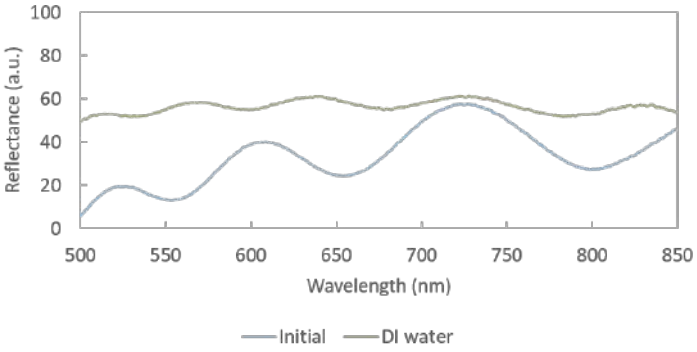

(a)

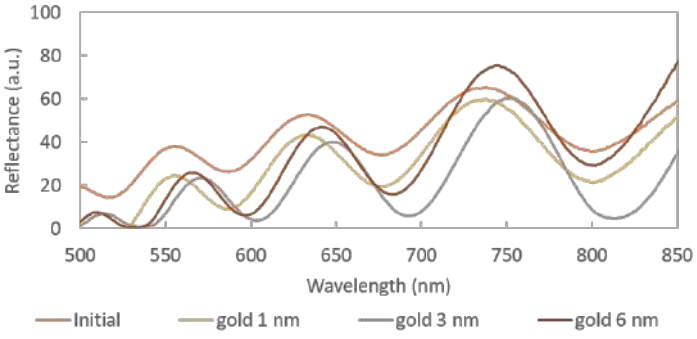

(b)

Figure 3.2. (a) Reflectance of NFs layer in air (initial spectrum) and deionised (DI) water. (b) Reflectance of NFs in DI water without gold (initial) and with gold layers of different thicknesses evaporated on it.

Once characterised the optical response and improved the peak-to-peak amplitude of the signal, a flowing experiment was performed to check the stability of NFs in such a dynamic environment. According to Equation 2.8, the peaks of the reflectance spectrum will experience a shift towards longer wavelengths when an increase in the NFs layer effective refractive index or thickness occurs. In contrast, a shift towards shorter wavelengths will occur if the effective refractive index or the thickness of the NFs layers decreases.

As a first approach, only DI water was flowed over the NFs layers. To track the maximum peak position MATLAB was employed as described in Section 2.6.3. As it can be seen in Figure 3.3, a constant drift of $\sim$150 pm min^{-1} of the peak towards longer wavelengths was observed. Since no change in the effective refractive index of the NFs occurred, such behaviour must be attributed to the swelling of the NFs structure, i.e. a thickness increase. Since the final objective is using this structure for biosensing, only a change in the effective refractive index of the layer is expected to provoke a change in the spectral position of the reflectance peak. Any other factor that could affect it will hinder or harden the biodetection. Consequently, a stabilisation of the NFs layer structure in aqueous media to avoid its swelling must be performed.

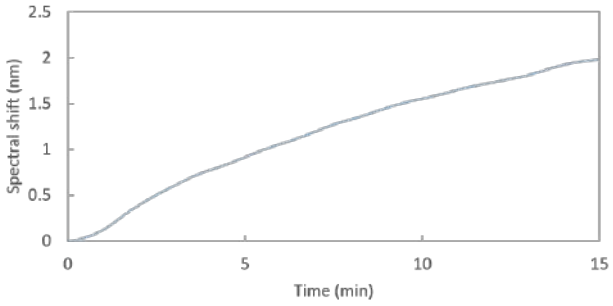

Figure 3.3. Experiment flowing DI water over a raw NFs layer. It can be observed a constant displacement of the maximum of the reflectance peak towards longer wavelengths, indicating the swelling of the structure.

3.3 Stabilisation of PA6 NFs layers

In order to increase the stability of the NFs layers in aqueous media, the followed strategy was fusing the contact point of NFs. As a prerequisite, the porosity of the structure and its FP cavity optical response must be maintained to allow the liquids to enter into the structure and perform detection experiments. For such aim, two approaches were studied: a chemical modification of the NFs (by solvent vapour treatment and by chemical crosslinking) and a thermal treatment.

3.3.1 Solvent vapour treatment

Solvent vapour treatment consists of exposing the non-woven net of NFs to the vapour of the solvent used for the polymer dissolution for deposition. The solvent dissolves and melts the already polymerised PA6, provoking the fusion of the contact points of NFs without notably varying the NFs structure and the layer porosity [142].

In order to apply the solvent vapour treatment to the PA6 NFs, 25 µL of pure acetic acid were dropped in a vial. The sample was placed upside down on the top of a vial and kept at room temperature for 15, 30, 45 and 60 min.

Afterwards, samples were removed and kept at room temperature in order to eliminate by evaporation possible traces of acetic acid vapour on them. No important variations in the reflectance or in the layer thickness were found in any case, but Field Emission Scanning Electron microscope (FESEM) images showed a slight reduction of the average NFs diameter from 33 nm to 31 nm (see Figure 3.4). Samples exposed for 60 min were used to perform real-time sensing measurements by flowing DI water. An average spectrum drift close to 120 pm min^{-1} was obtained, slightly lower than the one obtained for the non-stabilised NFs layers. This result indicates that only a slight improvement of the stability of the NFs layer was achieved, not being enough to avoid the spectral drift provoked by the swelling of the structure.

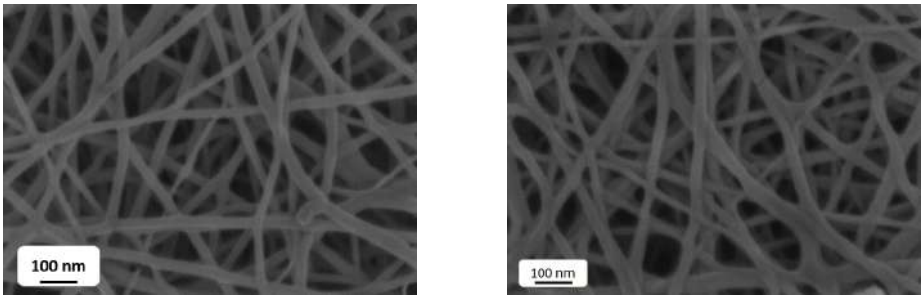

(a) **(b)**

Figure 3.4. SEM image of a NFs layer (a) previously to be exposed to vapour solvent treatment and (b) after 60 minute of exposure. No noticeable changes can be seen.

3.3.2 Hydrolysis and chemical crosslinking of NFs

The repeating unit of PA6 is $(C_6H_{11}NO)_n$ (see Figure 3.5). These monomeric units are bound by peptide bonds that can be hydrolysed by hydrochloric acid (HCl). This reaction results in the exposure of carboxyl and amino groups, which are able to react and form new peptide bonds if they are correctly activated [143]. This strategy is usually employed in order to bind proteins or any other biomolecule to the surface of PA6 supports [144].

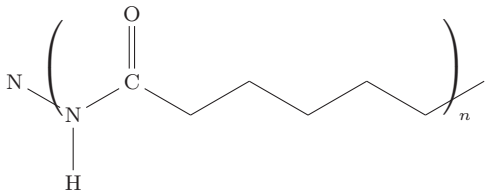

Figure 3.5. Repeating unit of PA6.

To stabilise the NFs layer, we aimed at exposing carboxyl and amine groups at NFs contact points and then, crosslinking them using glutaraldehyde, a well-known crosslinking agent previously used for pSi biofunctionalisation. It has to be considered that the region in which the reaction has to be carried out is very small compared with the high surface of the NFs. Because of that, hydrolysis ought to be well-controlled in order to hydrolyse only some peptide bonds of the NFs and avoid a loss of the layer stability. Therefore, NFs were not exposed directly to HCl but to its vapour for 15 min. Immediately after, they were rinsed with DI water and dried with a soft airflow. Then, NFs were immersed in 2.5 v/v% glutaraldehyde in 1X PBS for 30 min, rinsed with 1X PBS and dried with a soft airflow. As a result, the layer thickness was reduced by around 35 %, and the average diameter increased from 33 nm to 39 nm. Additionally, according to Figure 3.6, it seems that the NFs layer was partially dissolved, giving a reduction in its porosity. Real-time flowing measurements with DI water were performed and the drift was reduced to ca. 80 pm min^{-1}. Although smaller, such drift is too high for sensing purposes. Additionally, this approach carries a porosity and thickness reduction of the layer that might also affect detection experiments. Therefore, this stabilisation protocol was discarded as well.

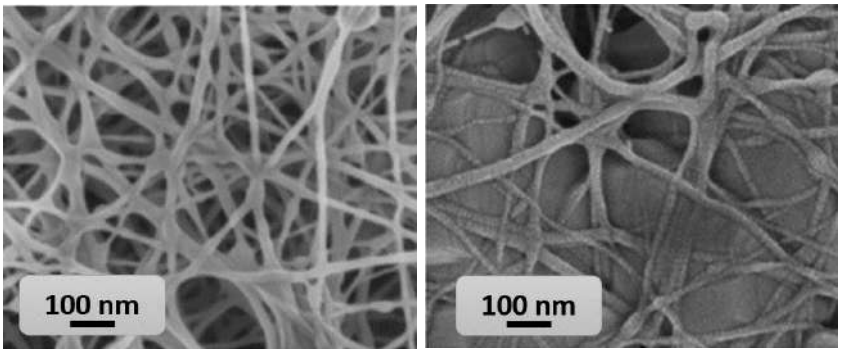

Figure 3.6. SEM image of a NFs layer (a) previously to glutaraldehyde crosslinking and (b) after it.

3.3.3 Thermal treatment

Heat treatment of NFs have been previously employed for the improvement of the chemical and mechanical stability of electrospun layers. In combination with pressure, it has been shown that contact points between fibres can be fused without varying the morphology of each individual fibre [145, 146]. Additionally, this treatment has been demonstrated to improve the adhesion between the electrospun layer and the material over which they are deposited [147]. Therefore, with this approach the NFs layer are expected to improve their stability not only by a crosslinking of their NFs, but also by a better attachment to the silicon

wafer substrate.

Firstly, the glass transition temperature (T_g) and the melting temperature (T_m) of the NFs layers were characterised by differential scanning calorimetry (DSC), since the applied temperature to fuse NFs must be comprised between these two parameters. According to Figure 3.7, T_g is close to 90 °C and T_m is close to 225 °C. Therefore, temperatures close to T_m (180 °C, 190 °C and 200 °C), together with a pressure of $\sim$500 g cm^{-2}, were applied for 1 h, 3 h and 5 h to NFs layer to find out the best configuration to fuse NFs contact points.

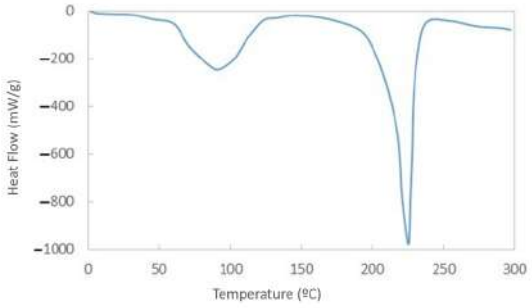

Figure 3.7. Differential scanning calorimetry (DSC) measurements of the NFs layers. The transition temperature (T_g) is close to 90 °C and the melting temperature (T_m) is close to 225 °C.

To study the resulting morphology after the thermal treatment, SEM images of differently treated samples were analysed. In Figure 3.8 two different treated samples are shown: 5 h at 200 °C (Figure 3.8.a) and 3 h at 190 °C (Figure 3.8.b). At a temperature close to T_m, the layer was melted, as expected. But a reduction of only 10 °C and a shorter heating time allow to partially melt the structure and, more importantly, the contact points of NFs. A slight increase of the NFs diameter (from 33 nm to 41 nm) was observed as well.

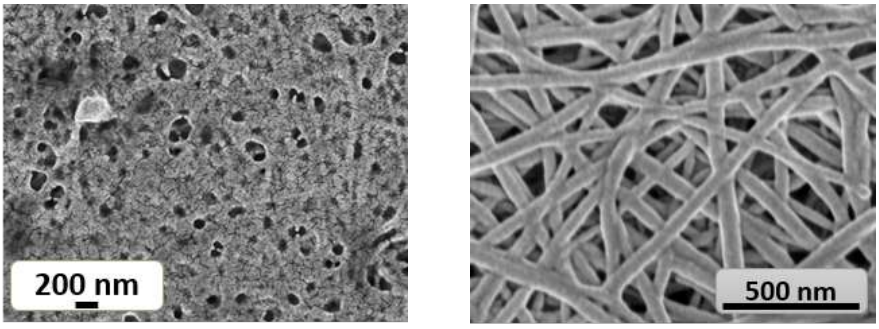

(a) **(b)**

Figure 3.8. SEM image of NFs layers heated (a) for 5 h at 200 °C and (b) for 3 h at 190 °C.

To measure the spectral drift of the structure due to the swelling after the thermal treatment, DI water was flowed over the structures. Summarised results are shown in Table 3.1. It was observed that best results of spectral drift were obtained for 3 h and 5 h at 190 °C. Since the heat treatment for 3 h at 190 °C is shorter, it was accepted as the best protocol to stabilise NFs layers (see Figure 3.9).

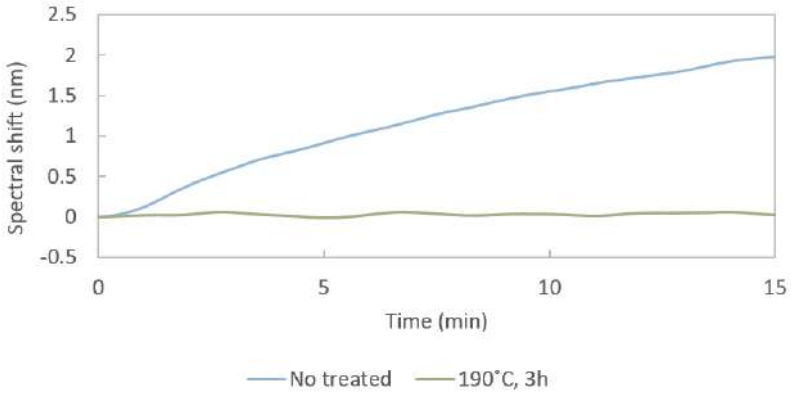

Figure 3.9. Spectral shift of the maximum of the reflectance peak when DI water is flowed over a non-treated NFs layer and a heated NFs layer at 190 °C for 3 h.

Also the thickness of the layers was measured by ellipsometry and, in all cases, a reduction of it was observed. But this effect is less noticeable in the samples heated at 190 °C for 1 h and 3 h. This thickness reduction affects the spectral shape by reducing the amount of peaks and increasing their width, making harder the detection of small variations of refractive index. These results reinforced the idea of NFs layers heated at 190 °C for 3 h as the best candidates for the development of the transducer.

Table 3.1. Summary of the different heat treatments applied to NFs layers, the morphological features of the resulting layers and the stability in DI water of their spectra.

NFs layer group	Temperature (ºC)	Time (h)	Average NFs diameter (nm)	Layer thickness variation (%)	Spectral drift (pm/min)
No treated	-	-	~ 33	-	~ 150
A	200	5	melted	~ -45	-
B	180	5	~ 36	~ 15	~ 30
C	190	5	~ 43	~ 25	~ 5
D	190	3	~ 41	~ 20	~ 8
E	190	1	~ 38	~ 15	~ 20

3.4 In-flow NFs biofunctionalisation and BSA biodetection

3.4.1 In-flow biofunctionalisation

Biofunctionalisation and biodetection experiments were carried out in flow. In this way, the increase in the effective refractive index of the NFs layers provoked by the attachment of biomolecules to its surface can be easily tracked in real time.

The specificity of antigen–antibody binding was used in this biosensor to ensure a reliable detection of the target analyte. Such detection occurs through the antigen binding fragment (Fab) of the antibodies and the epitope of the analyte, which requires a correct orientation of the antibodies on the NFs surface [148]. For this, recombinant protein A/G (AGp) was used as the intermediate protein, since it can adsorb to the NFs surface and bind the constant fragment (Fc) of the antibodies, attaching them to the NFs whilst leaving Fab exposed to the analyte solution [148–150].

To achieve such an oriented attachment of the antibodies to the NFs surface, a 50 µg ml^{-1} AGp solution in 0.1 M MES buffer (pH 4.5) was flowed for 30 min. Then, the protein excess was removed by flowing again 0.1 M MES for 10 min. As a result, a positive net spectral shift of 1.95 nm could be observed (see Figure 3.10). In the end, the fact that the maximum peak reached a stable final spectral position (i.e. a position centred at a given wavelength) when 0.1 M MES was flowed demonstrates that the refractive index change provoked by the binding of AGp to the surface of the NFs layer was stable and thus, its desorption did not occur.

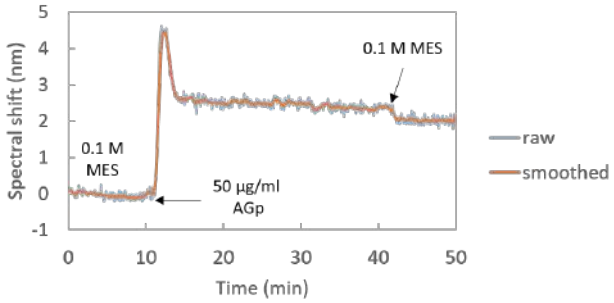

Figure 3.10. Real-time monitoring of the attachment of recombinant protein A/G (AGp) to the NFs when a 50 µg/mL solution of such protein was flowed. The stable position of the maximum peak when 0.1 M MES buffer was flowed at 40 min demonstrates that desorption of the AGp did not occur. The spike observed when AGp was flowed can be ascribed to fluidic irregularities and density differences between the AGp solution and 0.1 M MES buffer solution [151].

Afterwards, 2.5 mg ml^{-1} casein (1X PBS) solution was flowed for 30 min to block the remaining gaps between the AGp molecules in the NFs surface,

avoiding the unspecific adsorption of subsequent biomolecules to the surface and thus ensuring the specific recognition of anti-BSA antibodies (αBSA) by AGp and of BSA by αBSA. After removing the excess of casein by flowing 1X PBS solution for 10 min, a net spectral shift of 4.2 nm was observed (see Figure 3.11).

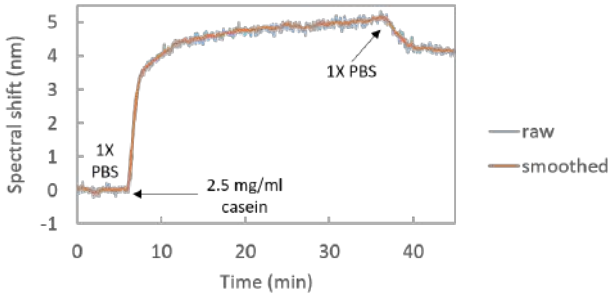

Figure 3.11. Real-time monitoring of the attachment of casein to the NFs surface to block the remaining empty spaces between AGp molecules, avoiding the unoriented attachment of αBSA to the NFs surface and forcing its oriented binding to AGp.

Then, 50 µg ml^{-1} αBSA solution in 1X PBS was flowed for 25 minutes and the excess was removed by flowing 1X PBS. Binding of αBSA by means of their Fc region to AGp led to a final spectral shift of 0.65 nm (see Figure 3.12), after flowing 1X PBS and removing the excess of αBSA solution from the medium. The final position of the maximum peak centred at a given wavelength while flowing 1X PBS for the last five minutes demonstrated that the binding of αBSA to AGp was stable and unbinding did not occur.

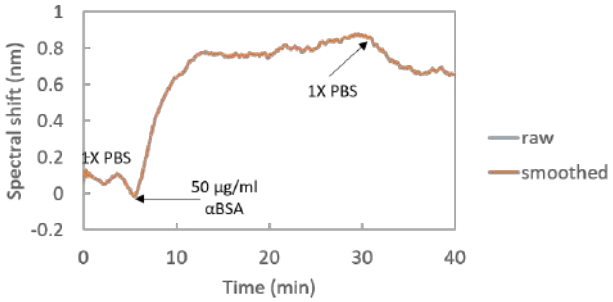

Figure 3.12. Real-time monitoring of the attachment of anti-BSA antibodies (αBSA) to the AGp molecules.

3.4.2 In-flow biodetection of BSA

At this point, an AGp–αBSA layer on the NFs surface was created and the in-flow biodetection of BSA can be performed. For such aim, a solution of 10 µg ml^{-1} BSA was flowed for 30 min. After flowing 1 X PBS to remove the excess, a net spectral shift of 200 pm was observed (see Figure 3.13). This result suggested the binding of BSA molecules to the NFs surface. However, this attachment could be the specific biorecognition of BSA by the antibodies or an unspecific binding to the surface.

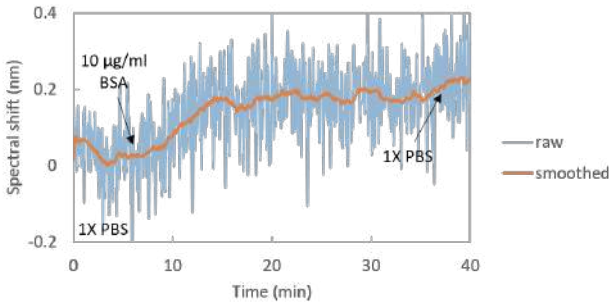

Figure 3.13. Real-time monitoring when 10 µg ml^{-1} bovine serum albumin (BSA) solution was flowed over NFs layers covered by αBSA.

To discard that the observed spectral shift when BSA was flowed was due to the unspecific adsorption of BSA to the NFs surface, 10 µg ml^{-1} BSA solution was flowed over two other NFs layers (named as NF1 and NF2) of the same electrospinning batch not having the αBSA bioreceptors. To this aim, 50 µg ml^{-1} AGp and 2.5 mg ml^{-1} casein were flowed over such NFs as previously stated in Section 3.4.1, but now the αBSA flowing step was avoided. In absence of the bioreceptor, when BSA was flowed, the slope attributed to the binding of BSA by αBSA could not be seen (see Figure 3.14), thus demonstrating the specific recognition of BSA by αBSA in the previous experiment.

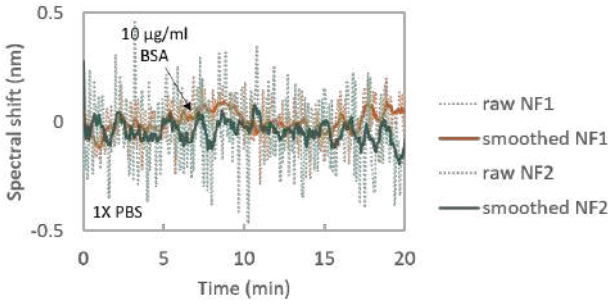

Figure 3.14. Real-time monitoring when 10 µg/mL BSA solution was flowed over NFs layers without αBSA.

Once the specificity of BSA detection was demonstrated, both the biofunctionalisation and biodetection steps were replicated in two other different NFs layers from the same electrospinning batch. The aim was to test whether electrospinning allows for the creation of several NFs layers with similar responses during the biofunctionalisation and biodetection steps and whether these steps are reproducible when the specific transducer changes. Figure 3.15 summarizes the experimental results obtained for these three samples, where it is indicated that NFs layers from the same batch have a similar response for all the biofunctionalisation and biodetection steps. Additionally, these results also confirm the reproducibility of the biofunctionalisation and biodetection steps when similar transducers are employed and the suitability of NFs layers for the specific biodetection of BSA. In conclusion, these results demonstrate the suitability of the electrospinning method to ease the fabrication process of optical transducers with a similar response for biodetection purposes.

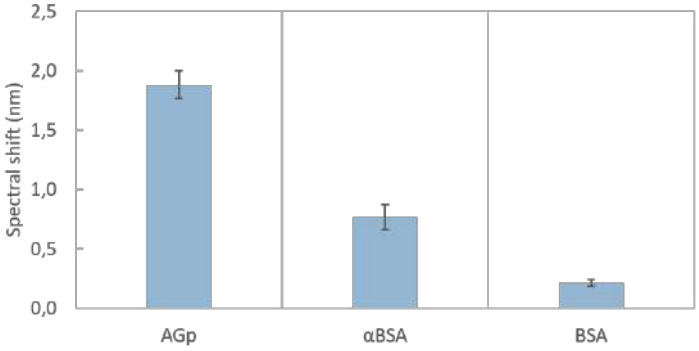

Figure 3.15. Spectral shift observed in three different NFs layers fabricated in the same electrospinning process when the same biofunctionalisation and biodetection steps (explained in Section 3.4) were carried out over them.

3.5 Conclusions

The results presented in this work demonstrate the suitability of electrospun PA6 NFs layers for the development of FP-based optical biosensors capable of detecting specifically the presence of a certain target analyte in aqueous solution when they are properly biofunctionalised.

Firstly, a valid protocol for the fabrication of electrospun NFs layers with a good FP cavity response was reported, becoming the first reported NFs layers suitable as an optical transducer. For their fabrication, a low concentration of PA6 was employed and salts were added to the electrospinning solutions to eliminate the appearance of beads that usually appear when low concentrations of polymer are employed.

However, in aqueous solution as-prepared NFs layers showed a constant positive drift of the spectrum towards longer wavelengths that could only be explained by the swelling of the structure –because the effective refractive index of the structure was kept constant during the whole experiment. Since this could be a limiting factor for the development of a biosensor, the work was focused on stabilising the structure by fusing the contact points of NFs. Different chemical and thermal treatments were explored, being the latter the one that gave better results. NFs layers heated at 190 °C for 3 h showed a little variation of the NFs diameter, a 15 % reduction of the thickness and a spectral drift of only $20\,\mathrm{pm\,min^{-1}}$.

Once a stable behaviour in aqueous solutions was achieved, real-time and label-free optical measurements were performed to track not only the biodetection of BSA, but also the biofunctionalisation of NFs surface. The successful biofunctionalisation of the structure employing AGp and αBSA was reported and the biodetection of $10\,\mathrm{\mu g\,mL^{-1}}$ BSA as well. Furthermore, similar optical responses were observed when both biofunctionalisation and biodetection procedures were performed in several samples from the same electrospinning batch, demonstrating the potential of electrospinning for the massive fabrication of transducers with similar characteristics, which would ease the massive production and use of the resulting biosensors.

Alternative porous materials such as porous silicon or porous alumina require longer fabrication procedures and the use of dangerous reagents [89, 152], whilst the electrospinning technique employed for the fabrication of NFs layers is an easier, safer, and cheaper manufacturing method [153]. Together with the fact that measurements are performed in the visible range, the use of PA6 FP-based biosensors implies cuts in experimental time and costs.

Nevertheless, a weak point of these NFs layers as FP-based biosensors is the low Q-factor they show compared to other photonic structures such as ring resonators [154] or photonic crystals [155], among others. Eventually, this low Q-factor can hinder the biodetection of tiny amounts of the analyte. Therefore, a compromise between sensitivity and low-cost of fabrication and experimental process and setup must be achieved according to the desired application.

In a nutshell, these results pave the way for the use of electrospun PA6 NFs matrices for the development of cheaper and easier-to-fabricate at large scales

optical biosensing devices for massive use. New biofunctionalisation protocols involving bioreceptors different from antibodies may be explored in the near future to make NFs layers specific toward different analytes of interest in different application fields.

Chapter 4

Commercial polycarbonate track-etched membranes

4.1 Introduction

Track etched membrane (TEMs) are polymeric porous layers made by the track-etch technique, consisting on creating marks on a polymeric membrane that are dissolved later to create pores in the material. Those marks, or tracks, are weakened regions of the polymer foil that can be created by two methods: irradiating with fission fragments of heavy nuclei or using ion beams from accelerators. Tracks, unlike other regions of the polymer, are sensitive to chemicals that can dissolve them, creating the pores. The morphology of such pores depends on the track and chemical etch rates and the different degree of damage provoked by the particles in different areas of the same track. By tunning the track-etch parameters, different porosity values and pore diameters can be achieved. Porosity can vary from 1 cm^{-2} to 10^{10} cm^{-2} and pores diameter can vary from tens of micrometers to ∼10 nm in polycarbonate TEMs, due to its higher sensitivity to organic solvents and its lower wettability [156].

Although the common use of TEMs is filtration and cell culture, our aim was using them for the development of label-free optical sensors, something never done before. As the previously employed pSi and NFs layers, the optical response expected for TEMs is also a FP cavity response according to Equation 2.8. For sensing purposes, the pores present in the structure can be filled by different solutions what should provoke a change in the effective refractive index of the TEM (see Equation 2.9) and hence, a change in the spectral position of the reflectance peaks. Unlike electrospun NFs or pSi, the fact that this porous polymeric material is commercially available means a simplification of the sensor development. Additionally, since TEMs are typically employed for filtration, the possibility of making liquids go through the porous structure –and not only fill the pores– could mean an improvement in terms of sensitivity.

In order to develop a sensor based on TEMs, the diameter of the pores is an essential parameter, as previously explained in Section 2.3. To create an homogeneous medium for light, pores <100 nm are required. Such pore diameter in track-etched membranes has been only achieved in polycarbonate foils. For that reason, polycarbonate TEMs were employed in this approach. The selected membranes were Whatman® 800307 polycarbonate TEMs. The membranes have a diameter of 19 mm, a thickness of 11 µm and a refractive index of 1.5551 at 2400 nm (obtained using the dispersion equation provided in [157]). The pores have a diameter of 30 nm, small enough to behave like a continuous medium for light.

4.2 Optical characterisation and stabilisation of polycarbonate TEMs

Firstly, the characterisation of the surface of commercially available polycarbonate TEMs was carried out. For that, SEM images were employed. In Figure 4.1 it can be observed the presence of pores with a bright appearance, in an irregular way and at a relatively high density on the surface of the membranes. Such irregular distribution has to be taken into account, because, depending on the illuminated area, it could lead to a different optical response of the layer at different points. This is why the effective refractive index at each point of the TEM will be different. Therefore, if TEMs are going to be used for sensing purposes, they should be in the same position during the whole sensing measurement to be sure that the changes observed in the spectral position of the reflectance peaks are only due to changes in the effective refractive index of the layer and not to changes in the TEM position.

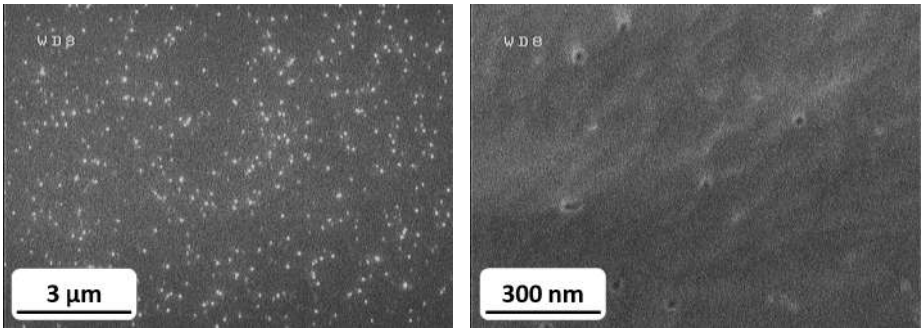

(a) **(b)**

Figure 4.1. SEM images of a commercial polycarbonate track-etched membrane (TEM) with a magnification of (a) 10 000 X and (b) 100 000 X.

To check if the polycarbonate TEMs show a FP cavity response, vertical reflectance measurements with the FTIR microscope were taken in the NIR range (1110 nm to 2500 nm). The set configuration was 30 scans for each measurement to enhance the signal-to-noise ratio (SNR) and a resolution of $4\,\mathrm{cm}^{-1}$. The background measurement was performed using a gold pattern with the same configuration.

When the TEM is placed in FTIR microscope surrounded by air, an interference fringe pattern characteristic of a FP cavity response appears. However, the reflectance was around 0.052 a.u., the peak-to-peak amplitude of the lobes was around 0.005 a.u. in the best case, and the spectrum was notably noisy, with a SNR value of 3.52 (see Figure 4.2.b). All these features are disadvantageous for the future employment of these membranes as optical sensing structures for two reasons. First, the noise can hide tiny displacements

of the spectra that could occur during the sensing event. Second, most solutions contain water and it is well known that its absorption coefficient in the NIR region is high [158]. If we place these aqueous solutions on the polycarbonate TEM in order to detect the presence of any component in it, part of the incident light will be absorbed by water and will not arrive to the polycarbonate TEM, leading to an even lower intensity of the reflectance signal.

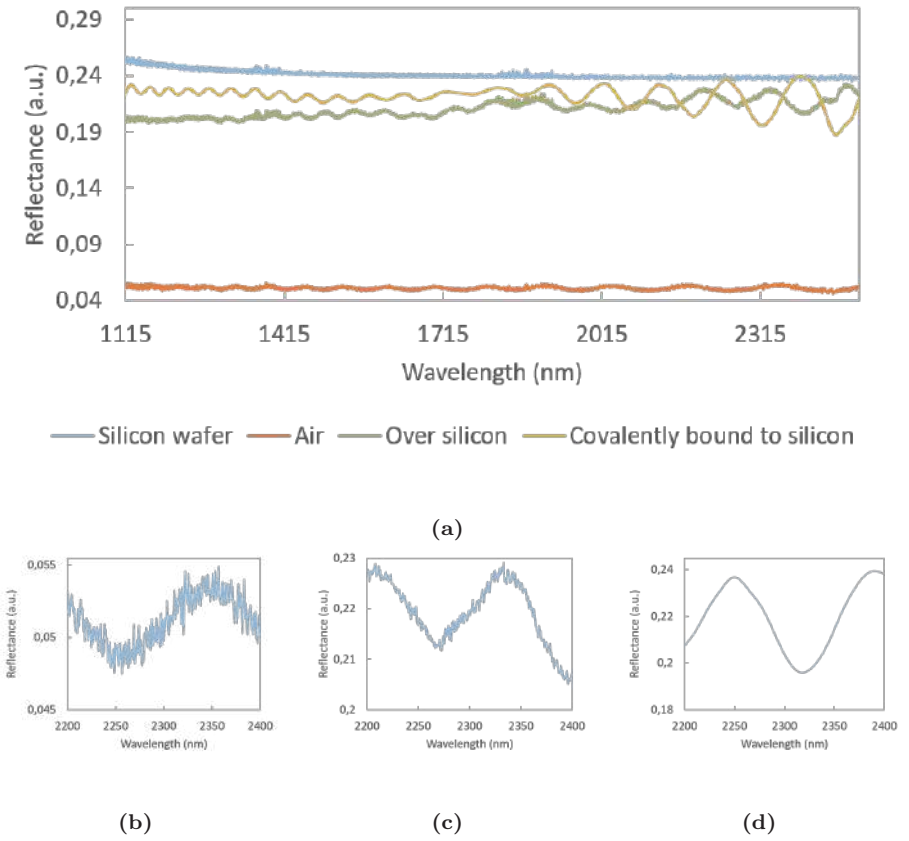

Figure 4.2. (a) Reflectance spectra of polycarbonate TEM surrounded by air, positioned over a silicon substrate and covalently bound to it. Detail of the spectrum between 2200 nm to 2400 nm for the polycarbonate TEM (b) surrounded by air, (c) placed over silicon and (d) covalently attached to it.

To maximise and improve the reflectance signal, and emulating what it was previously done with PA6 nanofibres in Chapter 3, a polished silicon surface was placed under the polycarbonate TEMs. Silicon has a reflectance signal of 0.24 a.u. and a flat spectrum in the NIR region where we are interested on carrying out the measurements (see Figure 4.2.a, light blue curve). Furthermore, placing a silicon wafer under the TEM offers an advantage: it might provide a

mechanical support to the labile membrane.

When measuring the optical response of a polycarbonate TEM simply placed on silicon, it can be observed that the reflectance of the polycarbonate TEM increases up to 0.2 a.u. (a 4-fold increase), the peak-to-peak amplitude of the lobes increases up to 0.014 a.u. and the SNR improves up to 9.88 (see Figure 4.2.c).

Nevertheless, only placing the polycarbonate TEM on silicon was not enough. To carry out sensing measurements it is essential to fix the position of the membrane. This can be achieved by covalently attaching the polycarbonate TEM to the silicon substrate, avoiding folding or displacement of the membrane. For that, the chemical protocol developed by Aran and co-workers was employed [159]. It is based on the use of (3-aminopropyl)triethoxysilane (APTES) as a crosslinking reagent. Briefly, the polycarbonate TEM was firstly activated by oxygen plasma in a plasma asher (PVA TEPLA 200, PVA TePla AG, Wettenberg, Germany) for 1 min at (50 W and 1.5 mbar). Immediately after, it was immersed in an aqueous solution of APTES at 80 °C for 20 min. Then, the membrane was removed from the solution and dried out on a cleanroom wipe. Once dried, it was dropped onto a newly activated silicon surface by piranha treatment (3:1 H_2SO_4:H_2O) for 10 min.

When it is studied the effect of the APTES-mediated covalent attachment of the polycarbonate TEM to the silicon substrate on the reflectance spectrum it can be seen that the APTES attachment preserves and even improves the reflectance spectra of the polycarbonate TEMs to perform sensing experiments. The reflectance is around 0.2 a.u., the peak-to-peak amplitude of the lobes is around 0.044 a.u., which is better than the previous measurement with no APTES treatment, and the SNR increases up to 36.92 (see Figure 4.2.d).

Although a well defined peak can be observed in the APTES-bound TEM, the peak-to-peak amplitude is still far away from that observed for NFs layers, which show a maximum peak-to-peak amplitude of 60 a.u. Therefore, during sensing experiments where the refractive index contrast between the TEM and the liquid filling the pores is too similar, the reflectance spectrum could almost disappear, as previously explained in Section 3.2. Nevertheless, instead of directly discarding the TEMs, some sensing experiments were carried out to study their sensing potential.

4.3 Sensing of refractive index variations

Once it was demonstrated that the spectral response of the polycarbonate TEMs is as expected (i.e., that for a FP cavity) and that the covalent attachment to a silicon substrate improves the reflectance spectrum and offers a mechanical support, the next objective was to demonstrate their suitability for use in sensing applications. To this end, a 10 µl drop of pure ethanol was placed on the area of the polycarbonate TEM illuminated by the light beam of the FTIR microscope. Then, it was let to evaporate at room temperature. The reflectance spectrum of the TEM was recorded every minute –i.e., the time required by the FTIR to

perform a measurement with the configuration previously described– before the drop deposition and during the evaporation. In this way, we can follow the shift experienced by the spectrum at a given point of the polycarbonate TEM in real time.

When the air present in the porous structure is replaced by ethanol, as ethanol has a higher refractive index than air, the effective refractive index of the structure increases and this is expected to provoke a shift of the spectrum towards longer wavelengths. Conversely, as ethanol evaporates, the air will start to fill the pores again and the effective refractive index of the structure will become smaller, which should make the spectrum return to its initial position. Regarding the spectrum, the best region to monitor how the position of its maxima changes when exposed to ethanol is between 2200 nm and 2500 nm. In this region, the peaks have a better quality factor and their amplitude is maximum, which will ultimately improve the sensitivity. In order to facilitate the identification of the peaks, the spectra were smoothed using the smooth function of MATLAB after acquisition.

In Figure 4.3, it can be seen that when ethanol fills the pores a shift of the spectrum of 19.29 nm occurs towards longer wavelengths (for the maximum at ca. 2400 nm). While evaporating, it can be clearly seen how the spectrum returns to its initial position gradually, and after 3 minutes, the sample seems to be almost dry as it reaches again the position in the beginning of the measurement. The differences in reflectance intensity during the measurement process are due to the layer of liquid created on the top of the sample. It increases the diffuse component of light reflected by the sample, thus reducing the number of beams arriving to the lenses of the FTIR microscope.

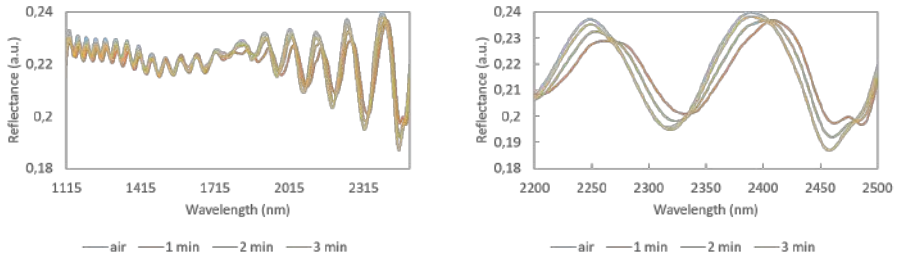

(a) **(b)**

Figure 4.3. Evolution of the reflectance spectrum of the TEM when placing pure ethanol on it. (a) For the whole characterisation range (from 1110 nm to 2500 nm). (b) Detail of the spectral region from 2200 nm to 2500 nm.

Immediately after the sensing of pure ethanol, another 10 µl drop of 50 v/v% solution of ethanol in DI water was placed on the polycarbonate TEM. The previous process was then repeated: the drop was evaporated at room temperature and the spectrum was recorded every minute with the FTIR

microscope. Figure 4.4 shows the reflectance spectra measured while carrying out this experiment. Here it can be observed a shift of 18.34 nm for the maximum peak located at ca. 2400 nm. Compared with the shift observed for pure ethanol, this shift is 0.95 nm smaller. The lower refractive index of the 50 v/v% ethanol solution, obtained by using the model proposed in [160], compared with the refractive index of pure ethanol obtained from [161], determines this smaller shift.

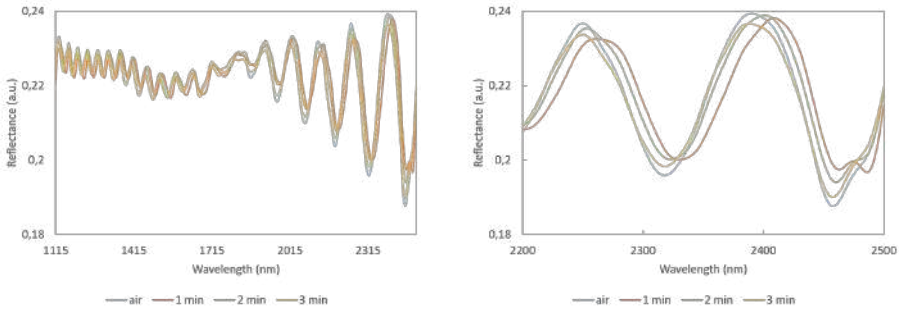

(a) **(b)**

Figure 4.4. Evolution of the reflectivity spectrum of the polycarbonate TEM when placing a 50 % ethanol solution on it. (a) For the whole characterisation range (from 1110 nm to 2500 nm). (b) Detail of the spectral region from 1110 nm to 2500 nm.

To check that the shift registered in the first FTIR measurement, after the deposition of the drop, is the maximum shift achieved by the spectrum –as the liquid could have slightly evaporated during this time lapse allowing the air to refill the pores [162]– the sensitivity of our sensor was calculated (summarised in Table 4.1). As both measurements were performed on the same point of the sample and under the same conditions, the differences might only be attributed to the different evaporation behaviour of the two solutions. For pure ethanol, a sensitivity of 56.49 nm RIU^{-1} is obtained, while for 50 v/v% ethanol solution 56.21 nm RIU^{-1} is obtained. Since they are very similar values, it can be assumed that the pores are equally filled by both solutions when the first FTIR measurement is done and that the differences in the shift only come from the different refractive index of the two solutions.

However, the bulk sensitivity values were too low compared to the $\sim$1000 nm RIU^{-1} showed by pSi [97] or 1060 nm RIU^{-1} showed by the NFs layers [163]. This, together with the bad definition of the spectral shape, led us to discard this structures for the development of biosensors, although their utility for sensing has been demonstrated for applications in which a high sensitivity is not required and where low cost is important.

Table 4.1. Summary of the refractive index values for each substance filling the pores, measured spectral positions for them during the experiment and calculated sensitivity values.

Solutions	Refractive index	Maximum position (nm)				Sensitivity
		Minute 0 (air)	Minute 1	Minute 2	Minute 3	
100 % ethanol	1.3415	2389.49	2408.78	2403.42	2389.61	56.49
50 % ethanol	1.3263	2390.09	2408.43	2401.28	2390.07	56.21
air	1.000					

4.4 Conclusions

In this chapter the capability of commercial TEMs to be employed for the development of optical sensors based on their optical response has been demonstrated for the first time.

Firstly, the optical response of the material was studied by performing vertical measurements in NIR region. It was reported that TEMs behave like a FP cavity, whose spectral shift towards longer or shorter wavelengths depends on the increase or decrease of the refractive index of the medium, respectively, as previously demonstrated with pSi and NFs.

Since the TEMs are labile layers, also the stabilisation of the structure of the layer and the optimisation of its optical response were studied. For such aim, TEMs were covalently bound to a silicon wafer by a silanisation reaction with APTES. In this way, an improvement in the reflectance, the peak-to-peak amplitude of the reflectance peaks and the SNR was reported. However, the best peak-to-peak amplitude value was 0.044 a.u.. That is a very low value that can be even lower if the TEMs were placed in an aqueous solutions, such as those employed for biosensing experiments.

Anyway, sensing experiments were carried out employing ethanol solutions and it was reported the shift of the spectrum as expected according to the refractive index changes occurring in the medium. A bulk sensitivity value of $\sim$56 nm RIU^{-1} was calculated, but this value was noticeably lower than the $\sim$1000 nm RIU^{-1} reported for pSi or NFs layers employed in our laboratories [97, 163]. Indeed, the sensitivity is pretty low compared with almost any other kind of optical transducer. Only some ring resonators have a similar bulk sensitivity [164]. This might be explained by the fact that TEM sensors only have a 0.4 % of porosity, while porous silicon typically has porosity in the range of 50 % and NFs, of $\sim$90 %. However, even with such a low porosity value, it can be clearly seen the presence of ethanol in the medium and TEMs porous structure presents an important advantage: it is ready to use. Therefore, this material could reduce the costs and time of manufacturing.

Altogether, this material was discarded as a good candidate for the development of label-free optical biosensor because of the low peak-to-peak value and the low sensitivity it shows. However, for the development of optical sensors where a higher sensitivity is not required and a low cost of the final devices

is pursued, TEMs could be a good candidate. Furthermore, polycarbonate is a versatile material that could be chemically modified to endow the final transducer with new functionalities [165, 166].

Chapter 5

Biosilica exoskeletons from diatoms

5.1 Introduction

Along this Thesis document nanostructured porous transducers that are artificially synthesised have been studied. However, since the Cambrian explosion, nature has evolved to create natural photonic structures able to control the flow of light in some organisms. Some examples are beetles and butterflies, in which these photonic structures are responsible of their bright colours, moth eyes or green algae, in which they act as antireflection coatings, and flora, where they control the light arriving to photosynthesis centres [53]. In other organisms, such as diatoms, photonic structures have been found, but it is still controversial whether or how they use them physiologically.

Diatoms are aquatic unicellular microalgae belonging to the eukaryotic protists. Actually, they are the microalgae class containing the vastest number of species: at least 100,000 species are identified worldwide. They can be found in almost any environment containing water, showing their capability to adapt to different conditions, and it is estimated that they are responsible for the 20% global photosynthetic fixation of carbon [167].

What distinguishes diatoms from any other organism is their silica cell wall or frustule, which covers the cell and constitutes the photonic structure itself. The frustule is formed by two thecae composed by a valve and one or more girdle bands that keep attached both thecae (see Figure 5.1). Girdle bands and valves present a different and characteristic periodic micro/nanoporous pattern formed by pores and chambers. Therefore, from a photonic point of view, they can be referred as a slab PhC (sPhC) with distinct symmetries and spectral ranges. sPhCs consist of slabs made on a dielectric material with a thickness of microns and a patterned periodic structure with a different refractive index along it [168]. This periodical pattern causes the light guided by the slab to undergo changes in its propagation, leading to the appearance of forbidden-to-propagate wavelengths, that is, PBGs in a certain direction [169], as previously seen in Chapter 2 with the corrugated waveguides.

This behaviour of girdle bands and valves as a sPhC was firstly demonstrated by Fuhrmann et al. [170] by means of 3D and 2D band-structure simulations using the dimensions of the frustule of a centric –rounded with radial symmetry– diatom species: *Coscinodiscus granii*. According to their results, the girdle band –with a squared lattice period of 250 nm, of the order of wavelengths of the visible light–, confines visible light and, in this wavelength range, resonances with a low optical group velocity were reported. On the other hand, in valves

–with a higher periodicity of 900 nm to 950 nm– the guided bands are in the infrared region and visible light is only partially guided, resulting in radiation of those wavelengths. Additionally to the guided modes, they calculated the penetration of the evanescent wave of the slab into the cytoplasm of the cell and they reported that the evanescent wave can reach the cell when the refractive index contrast of the frustule and the surrounding medium is low. Altogether, considering that the chloroplasts are right below the frustule and the dimmer the lightning conditions, the closer they are to it, these results suggested a possible biological role of the frustule: the efficient harvesting of light for photosynthesis.

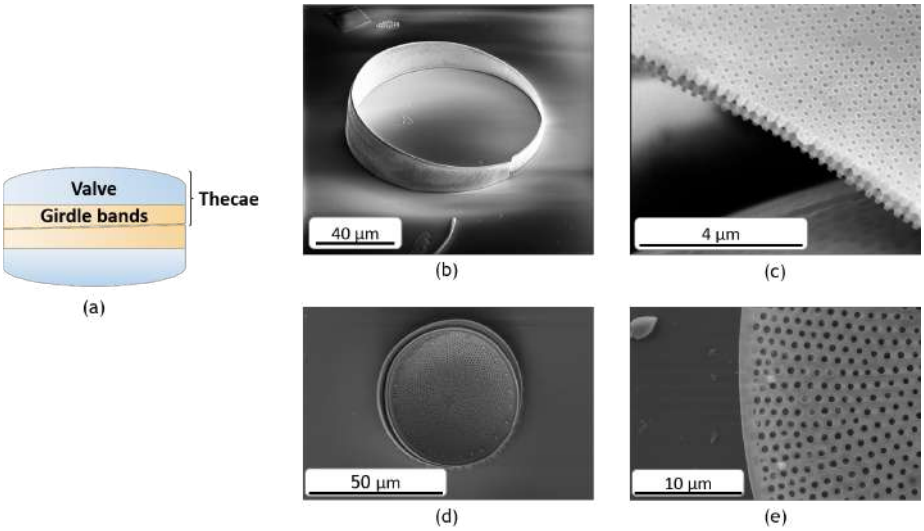

Figure 5.1. (a)Sketch of the diatom structure, consisting in two thecae composed by a valve and one or more girdle bands each one. SEM images of (a) a girdle band, (b) its squared periodic pattern, (c) a valve and (d) its periodic hexagonal pattern.

After this in silico approach of the diatoms as sPhC, the photonic properties of valves have been largely studied experimentally, demonstrating their capability to guide light and concentrate it at local hotspots depending on the wavelength of the light and the medium that surrounds the valves [171, 172]. However, very little attention was paid to the photonic properties of girdle bands until the work of Goessling et al. [173]. In that work, *C. granii* was also employed. Firstly, a very detailed description of the frustule structure is provided. The cells they worked with had a cell diameter varying from 40 µm to 200 µm, since the diameter of the cell is reduced from generation to generation during asexual reproduction. Despite this, the periodical pattern stays constant along generations. The valves are convex shells with holes in an hexagonal pattern with a lattice constant of 900 nm to 950 nm and a thickness of approximately 700 nm. In contrast, the girdle band has a square lattice with a lattice constant in X-

and Z-directions of 285 ± 5 nm and 279 ± 11 nm, respectively. The thickness of the band is 750 ± 40 and cylindrical macropores are in the X- and Z-directions interconnected by central rhombic chambers. Additionally, they also reported a new feature: the silica walls of both the valves and the girdle bands are not solid, but rather they have a nanoporous structure in addition to the macropores. [173].

Then, using a Fourier microscatterometry setup, they demonstrated experimentally for the first time that such periodical pattern of girdle bands leads to the appearance of a pseudogap of the photonic bands when the light hits the structure along the z-direction, that is, along the thickness of the girdle band and normal to the surface in which it lies. In the reflectance spectrum, this pseudogap results in a sharp peak in the NIR spectrum when a low refractive index contrast medium-girdle band exists, i.e. in water. The position in the spectrum of this peak is more dependent on the lattice period than on the diameter of the pores. However, they also demonstrated that the periodicity is pretty preserved among strains and specimens –unlike the pore diameter– and hence, also the position of the reflectance peak. In a later research, Goessling et al. [174] demonstrated that the effect of the pore diameter in the optical behaviour of the girdle bands is negligible when a low refractive index contrast medium-girdle band exists (as that found in water in nature). Additionally, they also reported only 1 defect per 100 unit cells in average, reinforcing the idea of a well preserved periodic structure and optical response. Altogether, these results evinced the potential of diatoms girdle bands as sPhCs.

Regarding their biological meaning, these observations about how well preserved the periodicity and hence, the optical properties are along different strains indicate that girdle bands could have a key role in the physiology of diatoms, although the authors suggest they would be shaped to not interfere with cellular light absorption for photosynthesis. Nevertheless, besides the biological role, the fact that highly reproducible sPhCs, working in the visible spectral range, can be easily obtained from an abundant natural source avoiding expensive and laborious nanofabrication techniques results really attractive for technological developments. Some research groups have proposed frustules as a drug delivery system by *in vivo* incorporation of drugs to the silica structure [175, 176], other groups are focused on tailoring new chemical functional groups on the frustule surface to endow it with new functionalities [177], others used the frustules as SERS platforms [178] or platforms for cell cultures [179] and others, aim at developing biosensors based on diatoms [180].

Considering the scope of this Thesis, it is especially interesting the availability of a porous natural material with a reproducible optical response with a high potential to be employed as an optical transducer for label-free optical sensing. Previously, some research groups have employed diatoms for the development of SERS [181] or fluorescence-based biosensors [182]. But currently, any research group has reported the possibility of directly using the optical response of the frustule for sensing.

Therefore, the aim of this chapter is demonstrating experimentally, for the first time, the potential of the girdle bands of diatoms, more precisely from *C.*

granii, for optical detection based on their optical response. For such aim, the change of the spectral position of the reflectance peak will be firstly pursued by the functionalisation of the girdle bands surface. Then, the capability of the sensor to respond to a progressive increase of the refractive index of the medium will be tested to study the sensitivity of the girdle bands as optical sensors.

5.2 Functionalisation of girdle bands

The first objective of this chapter is demonstrating the capability of functionalising the surface of the girdle bands to tune their optical properties and change the central position of the reflectance peak in the spectrum. One possible approach to do it is by changing the effective refractive index of the structure according to Bragg's law [183]:

$$\lambda_c = 2a_1\sqrt{n_c^2 - n_i^2 sin^2\theta_{in}} \tag{5.1}$$

where λ_c is the central position of the reflectance peak, a_1 is the modulus of the lattice vector of the structure, n_c is the effective refractive index of the girdle band structure, n_i is the refractive index of the medium filling the pores and ϑ_{in} is the incident angle respective to the normal plane of the PhC.

To change the effective refractive index of the sPhC (n_c) independently of the surrounding medium, the effective refractive index of the silica structure (n_{silica_eff}) must be changed, according to Equation 5.2 [173].

$$n_c = \sqrt{f_i n_i^2 + (1 - f_i) n_{silica\_eff}^2} \tag{5.2}$$

where f_i is the void filling fraction of the structure.

One way of of changing the effective refractive index of silica is by functionalising its surface. Considering that TiO_2 nanoparticles have a high refractive index of 2.7 at 500 nm relative to silica (n=$\sim$1.45), they were proposed as a good candidate for the functionalisation. If all the surface of the girdle band is covered by TiO_2 nanoparticles, a noticeable increase of the effective refractive index of the structure is expected and hence, a shift in the position of the reflectance spectrum. To attach the nanoparticles to the surface, a non-covalent functionalisation protocol by adsorption was developed employing a cationic polyelectrolyte monolayer.

5.2.1 Separation and cleaning of valves and girdle bands from diatom cultures

The first step to functionalise the girdle bands is their separation from the valves and the removal of the organic compounds that cover them. To obtain the frustules, diatom culture strain K-1834 of *C. granii* from the Norwegian Culture Collection of Algae (NORCCA) was employed. Such cultures were established from one single isolated cell and proliferated by asexual and sexual reproduction during long-term cultivation in a culture collection. L1 diatom medium [184]

was used on an artificial seawater base (30 ‰ salinity). Cultures were kept at 18 °C under natural sunlight illumination.

To remove the organic part of the frustules and separate the valves from the girdle bands, a chemical treatment was carried out. To a variable volume (V ml) of diatom culture, $\frac{V}{10}$ ml 10 % HCl solution was dropped. Then, $\frac{V}{5}$ ml 30 % H_2SO_4 and V ml of a saturated potassium permanganate ($KMnO_4$) solution were added and left overnight. Finally, a saturated oxalic acid solution was added dropwise until the solution became transparent. Afterwards, the solution was centrifuged for 10 min at 20 g and the supernatant was discarded and replaced by MilliQ water. This step was repeated three times. Valves and girdle bands were kept in MilliQ water for further steps and, in this document, they will be referred as 'clean' structures from now on.

The resulting concentration of girdle bands and valves was calculated by counting the number of structures found in 1 ml. For such aim a Sedgewick Rafter counting chamber and an inverted microscope (Nikon Eclipse Ts2, Nikon, Tokyo, Japan) were employed (see Figure 5.2). The valve concentration was 7644 structures ml^{-1}, and the girdle band concentration, 2372 structure ml^{-1}. Although the concentration of both structures is expected to be the same, as this diatom species bears one girdle band structure per valve, the obtained ratio valves:girdle bands is 3.22. This is due to the loss of girdle bands in the supernatant during the centrifugation process and it is consistent with the observations of Goessling et al. describing that valves and girdle bands show different hydrokinetic properties leading to a different settling rate during centrifugation steps: valves tend to precipitate faster than girdle bands [174].

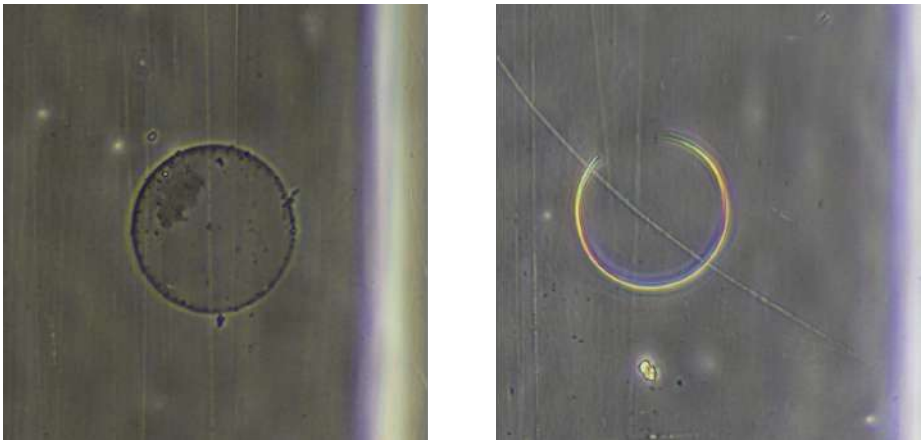

Figure 5.2. Aspect of valves (left) and girdle bands (right) after the cleaning and separation protocol under the inverted microscope. It can be clearly seen how the girdle band conducts light along the structure.

5.2.2 Attachment of TiO_2 nanoparticles to the surface of girdle bands

Since the functionalisation approach is based on electrostatic interactions between silica, the cationic polyelectrolyte and TiO_2 nanoparticles, their surface charge density should be studied.

The girdle band is a silica porous structure. Silica and silicate glass surfaces immersed in water are known to acquire a negative surface charge density. This is due to the silanol groups and the dissociation they experience according to Equation 5.3. The degree of dissociation of silanol groups and hence, the surface charge density is conditioned by the equilibrium established between the counter ions in the surface and in the solution [185].

$$\mathrm{SiOH} \rightleftharpoons \mathrm{SiO^-} + \mathrm{H^+} \tag{5.3}$$

Although the frustule is mainly formed by silica, it is covered by proteins and sugars [186]. This organic coating is supposed to be removed with the chemical treatment performed for the isolation of valves and girdle bands. Nevertheless, to confirm that the frustule structures are perfectly clean and show a negative charge density in the surface, zeta potential measurements were carried out before designing the functionalisation protocol. For such aim, a DLS system SZ-100Z (Horiba, Kyoto, Japan) was employed. Zeta potential of 500 µl of the resulting solution of valves and girdle bands from Section 5.2.1 in MilliQ water was measured. Five measurements were performed at 25 °C and the duration of the run was 45 s. The average zeta potential value obtained was −5.94 mV, what confirms the negative charge of the surface.

Then, the zeta potential of a TiO_2 nanoparticles solution in citrate buffer was also studied in order to predict the interaction that nanoparticles and the silica surface would establish. Five measurements were done with the same configuration employed for the frustule structures. The average zeta potential value obtained was −52.4 mV, indicating a negative charge density of the surface. Additionally, the diameter of the nanoparticles in solution was also studied by DLS measurements. The nanoparticles employed had an initial diameter of 5 nm when they were dry. However, in aqueous solution, nanoparticles in movement are covered by a dipole layer that changes the hydrodynamic friction of the particle. The resulting diameter of the nanoparticle with the surface bound species is known as hydrodynamic diameter and it is a good estimator of the absolute size of the molecule in such aqueous solution. In our case, this parameter has a big importance, since the aim is covering the whole surface of the girdle bands with the nanoparticles, even the inner surface of the pores. Therefore, TiO_2 nanoparticles must show a smaller hydrodynamic diameter than the pore diameter (∼100 nm) to assure they can go inside and avoid the problems previously seen in pSi. By DLS measurements, an hydrodynamic diameter of 38 ± 4 nm and a polydispersity index of 0.32 were obtained. These results indicated that the nanoparticles in aqueous solution could go inside the pores and they were not aggregated, respectively.

At this point, the negatively-charged surface of both silica and TiO_2 nanoparticles was reported and, thereby, their capability to interact with the cationic polyelectrolyte acting as an intermediate layer between them. Two polyelectrolytes were studied in this work: poly(allylamine hydrochloride) (PAH) and poly(diallyldimethylammonium chloride) (PDDA). Both are cationic polyelectrolytes (high pKa), but PAH has a molecular weight of 65 kDa, whilst PDDA has a molecular weight of 150 kDa (see Figure 5.3). Considering the big diameter of the girdle bands, it is hypothesised that PDDA could cover the surface in a more homogeneous way than PAH according to its bigger size.

(a) (b)

Figure 5.3. Repeating unit structures of (a) poly(allylamine hydrochloride) (PAH) and (b) poly(diallyldimethylammonium chloride) (PDDA).

The protocol followed for the functionalisation was as follows. Firstly, 272 µl of a 1 mg ml^{-1} polyelectrolyte (PAH or PDDA) solution in 0.5 M NaCl at pH 5.0 was added to 500 µl of the stock solution of girdle bands and valves. Then, it was placed on a shaker at 500 rpm for 20 min. Then, the sample was centrifuged at 2600 g for 30 min. The upper 600 µl of the supernatant were discarded and then replaced by MilliQ water to resuspend the pellet. The process was repeated two more times. In last step, the pellet was resuspended in 1090 µl of 0.2 mg ml^{-1} TiO_2 nanoparticles solution in 0.3 mg ml^{-1} sodium citrate. Then, it was placed on a shaker at 500 rpm for 180 min. Afterwards, the sample was centrifuged at 2600 g for 30 min. The upper 700 µl of the supernatant were discarded and then replaced by MilliQ water to resuspend the pellet. The process was repeated two more times. Finally, the functionalised girdle bands were kept in MilliQ water.

To study the success and the effects of the functionalisation in the optical response, two control samples were prepared. In one of the samples (control 1), instead of the polyelectrolyte solution, MilliQ water was added to study if the nanoparticles can directly adsorb to the girdle bands surface in absence of polyelectrolyte. The other sample (control 2) was exposed to the polyelectrolyte –PDDA, because, as previously mentioned, it was expected that it will cover the surface in a more homogeneous way than PAH– but instead of the nanoparticles, only the buffer in which they are dissolved is added. In this way, it is pursued to see differences only due to the polyelectrolyte and not to the nanoparticles.

As previously explained, the hydrokinetic properties of valves and girdle bands in solution are different. This work is focused on the girdle bands and their settling rate is slower than that of the frustules, tending to stay in the

supernatant. To assure that after all the centrifugation steps girdle bands were still in the solution it was carried out the counting of the structures (see Figure 5.4). It was observed that after centrifugation steps, part of the structures are lost in all the groups. When the polyelectrolyte is not employed (control 1 sample), the loss of structures is more pronounced. This could evince the fact that the covering of the structures with the polyelectrolytes increases their density and/or size and hence, their settling rate. Furthermore, differences can be observed between the two polyelectrolyte-containing groups. The loss of girdle bands is more pronounced in PDDA-functionalised girdle bands than in PAH-functionalised ones. This could be explained by a higher density/size of the PAH-functionalised girdle bands, but also to a lower density contrast of the PDDA-functionalised particles and the PDDA solution provoked by the higher molecular weight of PDDA. It is interesting to remark the similarity in the concentration of girdle bands in both groups treated with PDDA, indicating reproducible results. After the reaction with TiO_2 nanoparticles, practically the whole number of structures seem to be recovered, except in the control 1 sample (without polyelectrolyte), where the naked structures are still being lost during the centrifugation step, supporting the idea that the functionalisation endows the girdle bands with a higher density/size. The fact that a higher concentration is obtained after TiO_2 nanoparticles reaction in PDDA-reacted samples could be attributed to errors in the counting (see Figure 5.4).

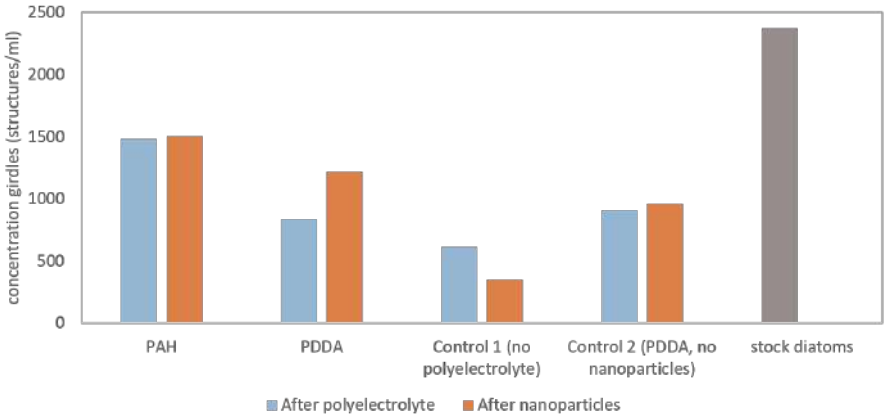

Figure 5.4. Concentration of girdle bands in different samples after the centrifugation step when the polyelectrolyte reaction (blue) and the nanoparticles reaction (orange) are carried out. The initial concentration of girdle bands in the stock solution is also shown to evince how many structures settle according to the treatment.

Afterwards, a zeta potential characterisation of the functionalised girdle bands solutions was performed to identify changes in the surface charge density provoked by the deposition of the polyelectrolyte and the nanoparticles. In Figure

5.5 it can be seen that after the chemical treatment with the polyelectrolytes and the TiO_2 nanoparticles, the frustule structures acquire a more negative charge than that showed when they were clean. This could be explained by the addition of the negatively-charged nanoparticles to the surface what would indicate the correct functionalisation of the surface. To determine if any difference exists between functionalising the samples with PDDA or PAH, a two-tailed t-test ($p<0.05$) was applied and no statistically significant difference between groups was found, indicating that both polyelectrolytes provoke the same change of the surface density charge of the silica structures.

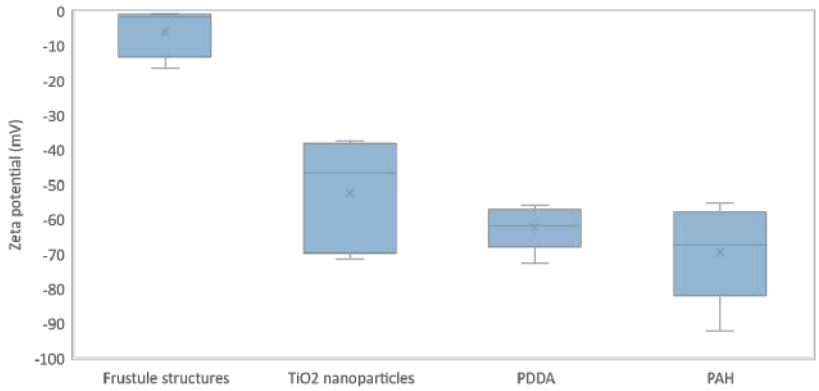

Figure 5.5. Zeta potential measurements of the clean frustule structures (a mix of girdle bands and valves in MilliQ water), the TiO_2 nanoparticles employed for the functionalisation of girdle bands and the frustule structures after the whole functionalisation protocol using two different polyelectrolytes (PDDA and PAH) and TiO_2 nanoparticles.

5.3 Optical characterisation of girdle bands

For the optical characterisation of the girdle bands, a Fourier image spectroscopy setup adapted for the study of natural photonic systems was employed (see Figure 5.6.a). The setup consists of a Nikon Eclipse T2 inverted microscope illuminated by a quartz tungsten halogen lamp and a Fourier imaging path. The latter consists of an iris, two optical switches, a photon density filter and two detectors: an spectrophotometer connected to an optical fibre and a CCD camera to check the field of view.

The working principle of the setup to perform a measurement is as follows. White light from the tungsten-halogen lamp is coupled with a multimode optical fibre of 50 µm diameter, then collimated and focused on the sample with a high numerical aperture oil-immersion lens (Nikon Plan-Apochromat 100 X NA 1.45 oil OFN25) (see Figure 5.6.b). This results in a reduction of the beam spot up to ∼2 µm to probe reflectance from the girdle band. Reflectance was collected for angles $\theta < \arcsin \frac{NA}{n_{oil}}$, where NA is the numerical aperture of the objective lens

and n_{oil}, the refractive index of the oil used for immersion of the lens. Since in our configuration $NA = 1.45$ and $n_{oil} = 1.51$, the maximum collected angle was $\theta_{max} = 74^o$. Reflected light was collected with a 100 µm optical fibre connected to a 2000+ Ocean Optics (Dunedin, USA) spectrometer (see Figure 5.6.c). Each individual spectrum was normalised against the reflectance spectrum of a silver mirror measured under the same conditions.

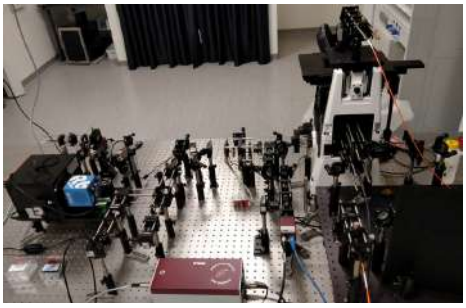

(a)

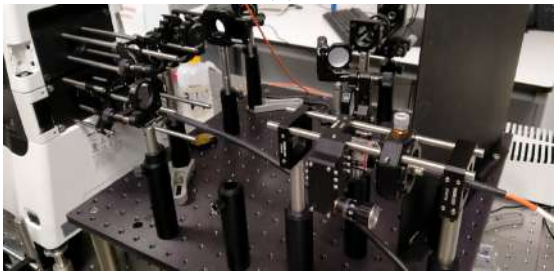

(b)

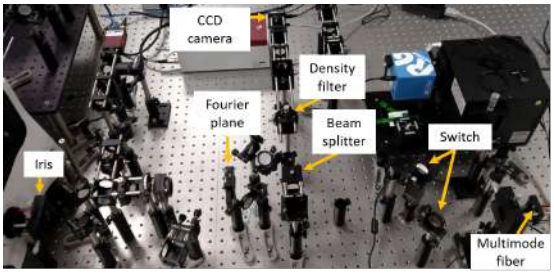

(c)

Figure 5.6. Microscatterometry setup employed for the optical measurements of girdle bands. (a)A general view of the setup, (b) the components of the light path before the microscope and (c) the Fourier imaging path are shown.

For the optical characterisation, clean girdle bands and valves in MilliQ water were dropped on a glass cover slip and placed over the oil-immersion lens to illuminate one girdle band (see Figure 5.7). The same was carried out with the

functionalised samples in MilliQ water. After performing the measurements, the reflectance spectrum was fitted to a Gaussian function using MATLAB to find automatically the central peak position.

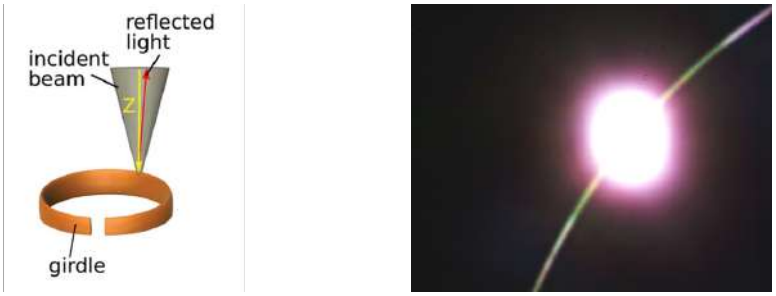

(a) (b)

Figure 5.7. (a) Sketch of the interrogation of a girdle band with a focused white light illuminating in the Z-direction. Reprinted from reference [173]. (b) Image obtained with the CCD camera where the spot of light illuminating the girdle band can be seen, as well as the girdle band guiding light.

Firstly, five clean girdle bands were measured in, at least, five different points of each structure and an average position of the reflectance peak at 760 ± 7 nm was obtained. In Figure 5.8 the spectra of three different points of the same clean girdle band are shown and a very conserved peak around 760 nm can be observed.

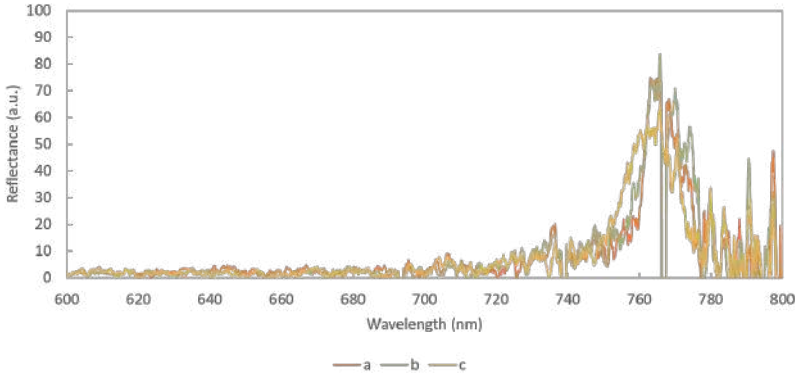

Figure 5.8. Reflectance spectrum of three different points (a-c) of a clean girdle band. A very conserved peak around 760 nm is observed.

Then, two functionalised samples –each one with a different polyelectrolyte– were measured at different points to check if the attachment of nanoparticles provoked a change in the spectral position of the reflectance peak and whether that change was reproducible. In figure 5.9, it can be observed the shift of the

reflectance peaks towards longer wavelength, if compared with the reflectance peak of a clean girdle band. In PDDA-functionalised samples, both reflectance peaks appear at ∼780 nm. However, in PAH-functionalised sample only one reflectance peak appears close to the PDDA peaks and the rest are placed at different positions at shorter wavelengths. This different behaviour was observed in another batch of functionalised samples and must be attributed to the different size of each polyelectrolyte. It has been reported that polyelectrolytes with a longer chain, i.e. a higher molecular weight, have a higher tendency to attach to the surface of spherical particles than polyelectrolytes with shorter chains. That different behaviour is attributed to a favourable gain in entropy of long chains in the surface [187]. This, together with the fact that the shift provoked in the reflectance peak was bigger in PDDA-functionalised samples, led us to abandon the use of PAH and focus on the use of PDDA.

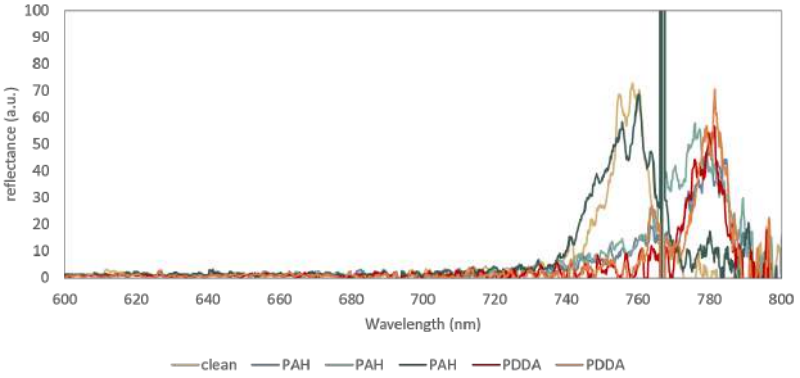

Figure 5.9. Reflectance spectra of two girdle bands functionalised with a different polyelectrolyte (PAH or PDDA). The reflectance of different points of each structure is shown. A very conserved peat at around 780 nm is observed for PDDA-functionalised samples, whilst a less conserved peak at different spectral positions is shown by PAH-functionalised girdle bands.

Figure 5.10 summarizes the reflectance measurements performed with three differently treated girdle bands. The optical measurements with PDDA-functionalised girdle bands were repeated in a bigger population of samples: five PDDA-functionalised girdle bands measured in, at least, five different points of their structure. It can be observed that the average spectral position of the reflectance peak was 773 ± 8 nm. This means a spectral shift of 13.7 nm, if compared with clean girdle bands, and confirms that a change in the effective refractive index of the girdle band structure occurred. To confirm that this spectral shift is due to nanoparticles attached to the girdle bands surface and not to nanoparticles that could not be removed after the cleaning and centrifugation steps and remained inside the pores, girdle bands from the control 1 sample –with nanoparticles but without PDDA– were measured. Five girdle bands from the control 1 sample were measured in, at least, five points of their structure. The

average spectral position of the reflectance peak in these samples was 764 ± 8 nm, which means a shift towards longer wavelengths of 4.6 nm if compared with the clean girdle bands, noticeably smaller than the functionalised sample. It is important to remark that the surrounding medium was always MilliQ water and hence, the changes observed in the reflectance peak could be only attributed to the modification of the surface of girdle bands. This result confirms that, as it was expected, in PDDA-functionalised samples the nanoparticles were not inside the pores, but attached to the surface.

To study if the observed differences between groups were statistically significant a Kruskal-Wallis test was applied with a confidence level of 95 % and statistically significant differences between groups were found ($H(2)=36.22$, p-value$=1.37 \times 10^{-8}$). To identify which groups were different from the other ones, the Bonferroni correction was done. Statistically significant differences between the functionalised girdle bands and the other two groups were found, whilst no statistically significant differences between the clean and control groups were found. In a nutshell, the functionalisation of the girdle bands with PDDA and TiO_2 nanoparticles leads to a spectral shift of the reflectance peak towards longer wavelengths, as it was expected.

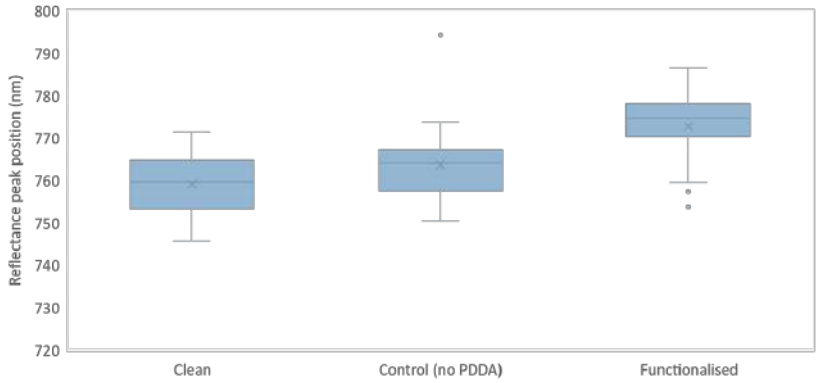

Figure 5.10. Spectral position of the reflectance peak showed by clean girdle bands, control girdle bands –only exposed to TiO_2 nanoparticles– and girdle bands functionalised with PDDA and TiO_2 nanoparticles. The appearing of the reflectance peak at longer wavelengths is observed for functionalised samples.

5.4 Optical detection of refractive index changes

Once demonstrated the possibility of functionalising the surface of girdle bands to tune the spectral position of their reflectance peak, the capability of these structures to detect changes of refractive index in the surrounding medium was studied.

To perform the refractive index sensing measurements, TiO_2-functionalised

girdle bands were employed. The idea was exposing the girdle bands to different aqueous solutions of glucose, because the refractive index of some glucose solutions is well known [188], it is a relatively cheap reagent and it has been largely employed for this kind of calibrating experiments [189].

In previous optical measurements shown in this chapter, girdle bands solutions were just dropped on a glass cover slip before measuring them. However, in aqueous media the girdle bands can float and any movement, such as the change of the medium, can provoke the displacement of the structures. Previously, this was not a problem because the idea was studying the reproducibility of the biofunctionalisation process at different points of the girdle bands by making only one measurement at each point. However, in sensing experiments several measurements are taken at the same point and it is essential that the girdle band stays at the same position during the whole experiment, since that is the only way of assuring that any observed change in the spectral position of the reflectance peak is only due to a change in the medium refractive index and not in the position of the structure. To fix the position of the girdle band in the glass cover slip, a strip of platinum was placed in the edge of the girdle bands by focused ion beam (FIB) induced deposition of platinum. Additionally, a mark was also created to make easier finding the structure of interest during subsequent optical measurements in the light microscope (see Figure 5.11).

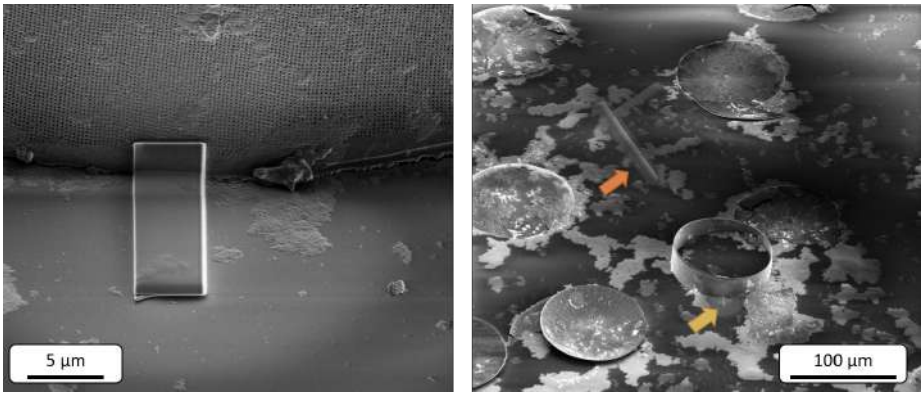

Figure 5.11. SEM image of the fixation of the girdle band to a glass cover slip by depositing a platinum strip by focused ion beam (FIB) induced deposition. On the left it can be seen a detailed picture of the aluminium strip. On the right, both the aluminium strip (yellow arrow) and the aluminium mark done to find easier the structure in the optical microscope (orange arrow) are shown, as well as frustules and valves.

Since the mechanical attachment of the girdle bands to the glass cover slip allows their unequivocal identification, Energy Dispersive X-Ray (EDX) composition analyses of one functionalised and one control girdle bands were performed. Previously to the measurement, both structures were thoroughly rinsed with MilliQ water to remove any residue that could interfere, such as

TiO_2 nanoparticles that could have stayed in the suspension, taking advantage of the fixing by the platinum strip. It was observed that the composition of both structures was the same, except for a peak attributed to TiO_2 bonds, only observed in the functionalised sample, confirming the proper functionalisation of the structure and previous observations based on reflectance measurements (see Figure 5.12).

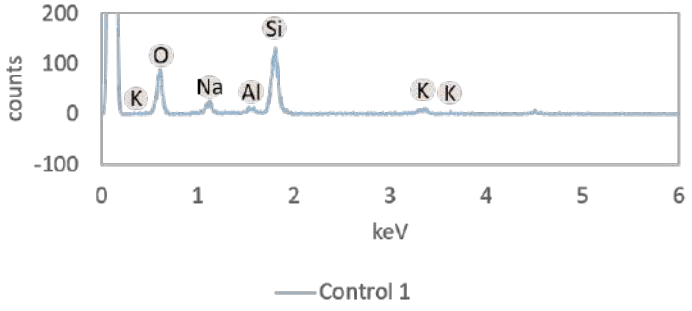

(a)

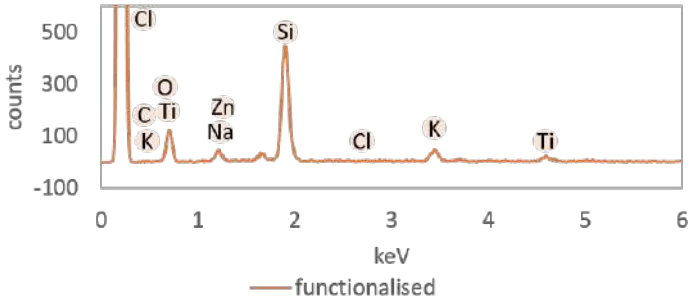

(b)

Figure 5.12. EDX measurements of (a) girdle band without PDDA and exposed to TiO_2 nanoparticles (control 1) and (b) girdle band functionalised with PDDA and TiO_2 nanoparticles. Ti is only present in the sample fully functionalised.

The refractive index sensing measurements were carried out in three different positions of a functionalised girdle band previously attached to the glass cover slip and five different concentrations of glucose were dropped: $4\,mg\,ml^{-1}$ (n= 1.3335), $23\,mg\,ml^{-1}$ (n= 1.3354), $48\,mg\,ml^{-1}$ (n= 1.3379), $100\,mg\,ml^{-1}$ (n= 1.3431) and $269\,mg\,ml^{-1}$ (n= 1.36) [188]. After each experiment, the sample was thoroughly rinsed before performing another measurement. To exchange the different solutions of glucose, they were removed by capillarity using a filter paper.

The results are summarised in Figure 5.13. In all the spots measured it can

be seen a linear response with the increase of refractive index of the medium. Point 2 and 3 show a very similar behaviour when different concentrations of glucose are dropped over them. Indeed, the sensitivity of these two regions are very similar: 529.51 nm RIU^{-1} in peak 2 and 468.6 nm RIU^{-1} in peak 3.

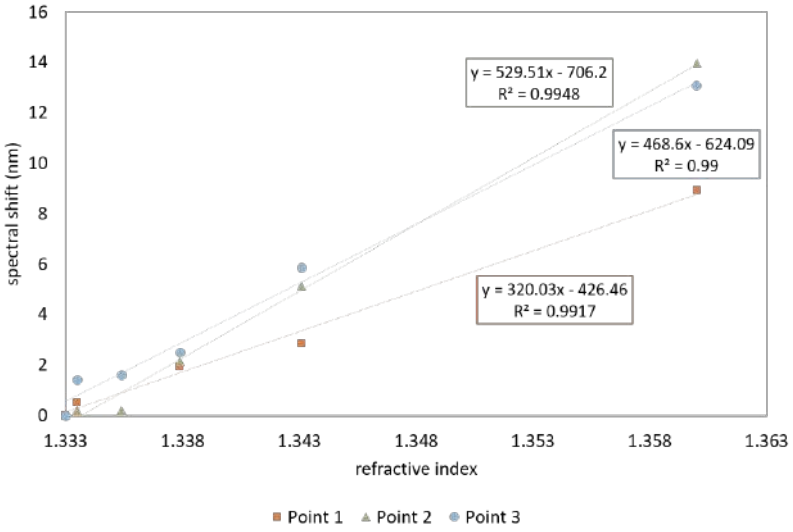

Figure 5.13. Results of three glucose sensing experiments performed at three different points of the same functionalised girdle band. The linear fitting of the data is also shown.

These sensitivity values shown by diatoms exoskeleton are better than those shown by more-complex-to-fabricate ring resonators [190, 191]. Even the lower sensitivity shown by the girdle band in point 1, 320.03 nm RIU^{-1}, is higher than that shown by ring resonators. However, it is evident that the response of the three points is different. This is attributed to several factors. Firstly, to structural differences between different regions of the girdle band. The height of the girdle band is not constant along the structure –it is shorter as you are closer to the opened gap–, it is currently not known whether the thickness is constant along the whole structure and defects can be found along it, i.e. absence of pores. In addition, the girdle band can bend and thereby may cause a slight variation in the pore-to-pore distance in this type of experiment, where the optical response is measured over a small spot in z-direction. These factors affect the optical response but also the surface-to-volume ratio, being the latter especially important for sensing purposes. A smaller thickness or number of pores means a lower surface-to-volume ratio and hence, a smaller sensitivity of the structure at that point. Secondly, girdle bands can be slightly tilted when they are fixed to the surface, meaning a worse coupling of light to them and a worse optical response that could hinder the detection. It is important to remark that the quality factor of the reflectance peak can vary and the wider it is, the

lower sensitivity can be achieved in the measuring.

5.5 Conclusions

In this chapter, it has been demonstrated for the first time the utility of the girdle bands of *C. granii* to carry out optical sensing based on their optical response.

Firstly, it was demonstrated the possibility to chemically attach to the girdle bands surface TiO_2 nanoparticles via a self-assembled monolayer of polyelectrolytes. To the best of our knowledge, this is the first time that frustules are functionalised following this strategy. Most of the approaches are based on organosilane molecules [192] or require long and laborious steps [193]. However, here it was demonstrated an easy, fast and valid functionalisation protocol. Although the attachment of TiO_2 nanoparticles to the surface of the girdle bands was mainly carried out to check if a change in the refractive index of the structure provokes a change in its optical response, the resulting TiO_2-covered girdle band could be employed for photocatalysis purposes [194, 195], for example. Additionally, the girdle band covered by the polyelectrolyte results in a very versatile surface for the adsorption of other sort of molecules, such as biomolecules, opening the application field of girdle bands to biosensing [196], for example.

Secondly, it was also reported the change in the spectral position of the reflectance peak according to changes in the refractive index of the surrounding medium. In some points of the girdle band, high sensitivity values were obtained, even better than those showed by other artificial photonic structures such as ring resonators. Therefore, using girdle bands as optical transducers not only improves the performance of the final device, but also the way of producing it. Diatoms are highly available in nature and they can be cultured in the lab, obtaining very reproducible sPhC ready to be used in photonic applications. Therefore, expensive, complex and low reproducible nanofabrication techniques are avoided. Additionally, there is a vast variety of diatoms whose optical response could vary depending on their periodical structure, giving rise to a wide range of photonic structures. Additionally, one girdle band can give rise to several sensors, since a surface as small as $4\,\mu m^2$ is needed to be interrogated using the microscaterometry optical setup employed in this work.

Finally, this is the first time that the girdle band is isolated for sensing purposes. All the published research works that use diatoms for the development of biosensors work with the whole structure of the frustule or the valve. One good motivation to work only with the girdle band is the fact that they show an optical response in the visible range, reducing costs related to the interrogation system.

Regarding the limitations of the work, the attachment of the girdle band to the glass cover surface is a relatively slow process that could be replaced by another method in the future. Additionally, a fluidic chamber could be assembled over the girdle band, simplifying the detection process and ensuring

reproducibility given the potential variation in central reflectance peaks by local structural inequalities, as demonstrated in this work.

Chapter 6

Conclusions and future work

6.1 Conclusions

This Thesis in mainly focused on the study of some potential porous materials for the development of optical transducers that, once properly biofunctionalised, would allow the development of label-free optical biosensors. For such aim, their optical response was studied and then, biofunctionalisation and biodetection protocols were developed for those with a higher potential. Very different materials were proposed but always having in mind one goal: simplifying the fabrication of the optical transducer whilst maintaining a good optical response and a porous morphology that would increase the surface-to-volume ratio and hence, the sensitivity of the sensor. Well established materials for the development of biosensors were studied, such as porous silicon (pSi), but also materials previously used for biosensing purposes whose morphology had not been deeply studied to create optical transducers, such as the electrospun polymeric nanofibres, materials ready to buy that would avoid long and complex fabrication steps in the laboratory, such as the track-etched membranes (TEMs), and natural and abundant materials that can be easily found and whose features overcome the ones of some artificial materials, such as the biosilica exoskeletons of diatoms.

Regarding pSi, it was proposed because of its already demonstrated potential by other research groups. Firstly, the optimisation of the electrochemical etching was carried out to obtain big enough pores by varying the composition of the electrolyte adding DMF, what results in pores of up to 30 nm. Then, it was studied the hydrosilylation and thermal oxidation of the samples to stabilise them in aqueous solutions and endow their surface with new chemical functionalities for the following covalent attachment of the bioreceptor. Regarding the latter, thrombin binding aptamer (TBA) was chosen because of its easy and cheap synthesis and its high affinity to thrombin, a key protein involved in the coagulation cascade. The detection of 27 nM thrombin was demonstrated using pSi, but a low and noisy signal was obtained despite applying two different signal processing. However, a slightly better result was seen using the hydrosilylated samples followed by the anchoring of the TBA by using EDC/NHS. To study how efficient the covalent attachment of TBA was, FTIR-ATR measurements and real-time optical tracking of each of the steps of the biofunctionalisation protocol were carried out. By means of optical measurements all the biofunctionalisation steps were successfully followed, but using FTIR-ATR the characteristic peaks of TBA were not found, indicating that the density of bioreceptors was low and could be limiting the sensitivity of the biosensor. According to previously published studies, small pore diameters and big thicknesses of the pSi layer compromise

the diffusion of the solutions inside the pores and hence, the biofunctionalisation and biodetection processes. Considering that other groups working on pSi-based biosensing use samples with pores of at least 50 nm of diameter and we could only achieve pores of 30 nm, it was hypothesised that our main limiting factor for using pSi in biosensing was the pore diameter.

The sensitivity limitation due to the small pore diameter was confirmed with 1D PhC corrugated waveguides. Using the same bioreceptor –TBA– and biofunctionalisation protocol –silanisation with APTES–, the continuous and specific biodetection of thrombin concentrations ranging from 270 pM to 27 nM was reported. This range of detection is lower than that typically shown by traditionally employed analysis systems for the monitoring of thrombin generation. Moreover, the binding thrombin-TBA could be followed in real time without labels. Although other biosensors have been demonstrated to detect lower concentrations, they required the use of labels and long incubation times. The fact that a bulk material shows a better sensing performance than a porous material such as pSi –widely employed for biosensing because of its reported high sensitivity– demonstrates that not only the porous structure but also a good optimisation of it must be carried out to exploit the potential of porous materials. Additionally, factors such as the hydrodynamic diameter of the molecules to be flowed or the chemical treatment applied to the surface might have a great influence in the final performance of the biosensor.

Considering the biosensing limitations observed in pSi due to the limited pore diameter, nanofibres (NFs) layers synthesised by electrospinning were proposed as an alternative. This synthesis approach showed two advantages: it was easier and safer than the electrochemical etching employed for pSi fabrication if a large area of samples wants to be synthesised and the porosity of the resulting structure was higher (around 90 %). Firstly, the fabrication of these NFs layers was optimised by using different concentrations of polyamide 6 (PA6) and salts, being the solution of 6 wt% PA6 and 5 wt% pyridine salt the best one to produce NFs with a diameter of 22 nm to 40 nm. This small diameter strongly conditions the optical response of the NFs, which was demonstrated to be a FP cavity response, thereby demonstrating the utility of NFs layers as an optical transducer for the first time, to the best of our knowledge. However, in aqueous media, the as-prepared NFs layers showed an unstable optical behaviour, i.e. a constant shift of the spectrum towards longer wavelengths, because of the swelling of the structure. Considering the ultimate use of NFs layers in biosensing purposes –in which aqueous media are employed– this issue must be addressed to avoid mistaking the swelling with the biodetection events. To such aim, the cross-linking or fusion of the contact points between NFs was studied. Chemical dissolution of the polymer, covalent linking and a thermal treatment were applied, being the latter the one that gave better results. Indeed, the spectral drift in aqueous solution was reduced from $\sim$150 pm min^{-1} to $\sim$8 pm min^{-1}. With this quasi-static behaviour in aqueous solution, in-flow biofunctionalisation and biodetection experiments were carried out with the NFs layers. Although the main aim of the NFs was using them for the biodetection of ricin in the OPTONANOSENS project, a biological warfare agent simulant (BWAS) was initially employed: BSA. In real-time and

without requiring any amplification or labelling of the molecules implied, the biofunctionalisation steps –with antibodies via recombinant protein A/G– were tracked. Then, the biodetection of 10 µg ml^{-1} BSA was also demonstrated, as well as the specificity of such recognition. Therefore, for the first time as far as we know, also the utility of electrospun NFs for biosensing purposes based on their optical response was demonstrated. However, the low Q-factor shown by the reflectance peaks limited the sensitivity of the final biosensor, despite the high porosity achieved. Therefore, depending on the final application, a compromise between the sensitivity and the low-cost of the fabrication and the experimental setup –measurements were carried out in the visible range avoiding the use of expensive lasers– must be achieved.

In order to simplify even more the fabrication of the porous optical transducer, a commercial polycarbonate TEM was proposed as a valid candidate. Initially, the main advantage of these membranes, in addition to their easy availability, was the possibility of making liquids flow through the structure –since they are typically employed in filtration purposes–, what was expected to increase the sensitivity. Surrounded by air the membrane showed a FP cavity response, however it was necessary to covalently bind the polycarbonate TEM to a silicon surface by APTES-mediated silanisation to obtain a clearly defined reflectance response with a peak-to-peak amplitude of 0.044 a.u.. In this way, the signal was good enough to perform real-time sensing measurements, but the liquids will not longer be able to go through the structure, losing one of the initial advantages of this material. To test the possibility of performing sensing assays with the TEMs, different solutions of ethanol were dropped and a sensitivity of ∼56 nm RIU^{-1} was obtained, demonstrating the potential of TEMs to be employed in sensing experiments. However, considering it is a porous material, the obtained sensitivity value was low and might be explained by the low porosity of the samples (∼0.4 %) and their low reflectance. Moreover, for biosensing purposes where aqueous-based buffers are usually employed, these TEMs are not expected to be good candidates. Because of the low refractive index contrast between the membrane and the aqueous solutions, the spectrum is expected to almost completely disappear. On the other hand, for applications in which a high sensitivity is not required and the contrast between the TEMs and the solution to analyse is high, TEMs could be good candidates for the development of cheap and easy-to-manufacture optical sensors.

Finally, as the easiest-to-obtain porous structure for the development of optical biosensors, diatoms were proposed. Unlike the rest of the proposed porous structures, this is a natural one and thus, no fabrication steps are required –not even from a commercial company. Diatoms have been previously used for the development of biosensors, but never based on their optical response. Another novelty of this work using diatoms is the use of the isolated girdle band as a sPhC for sensing purposes, not the whole frustule or the valve as previously done by other research groups. The main advantage of using the girdle band is that a very well conserved periodic pattern has been described between strains and different specimens of the same species, which predicts a very preserved optical response as well, as demonstrated in this work. After characterising their optical

response, the aim was demonstrating the potential of girdle bands as optical sensors. Firstly, it was reported the correct functionalisation of the surface of the girdle bands with cationic polyelectrolytes and TiO_2 nanoparticles and how this modification of the effective refractive index of the silica walls changes the spectral position of the reflectance peak –shifting it towards longer wavelengths. Then, the optical response of such functionalised girdle bands when the refractive index of the medium changes was explored by using aqueous solutions with different concentrations of glucose. As a result, a progressive shift of the reflectance spectrum towards longer wavelengths was reported as the refractive index of the medium increased. Sensitivity values of up to $\sim$530 nm RIU^{-1} were obtained, although variability in the sensitivity depending on the area of the girdle band analysed was observed, probably because of irregularities in its morphology and its position relative to the light source. Therefore, it was demonstrated the suitability of the girdle band of the diatom frustule to develop optical sensors based on their sPhC optical response. The high availability of this structures in nature and the low cost and rapid production in controlled conditions, paves the way for the easy development of new optical transducers with outstanding working parameters. Additionally, these results show how perfect nature is and encourage to look for inspiration in it for the development of new and more optimised technologies.

According to the results presented in this Thesis, it can be concluded that not only the use of a porous material but also its morphology and its optical response condition the final performance of the resulting optical transducer during (bio)sensing assays. Additionally, also a compromise must be achieved between how easy and reproducible is the fabrication process of the material, how simple and cost-affordable is the optical setup for measurements and the final sensitivity shown by the device according to the final application. In our opinion, for the development of a label-free optical biosensor NFs layers and girdle bands of diatom frustules seem to be the ones with the most potential. However, due to lack of time a deeper research using them for biosensing purposes could not be done.

6.2 Future work

Many different adaptations and experiments have been already started but not concluded or left for the future. Future work concerns new proposals to try different porous materials and the extension of the already studied ones in new bioassays with application in the biomedical field.

Regarding pSi, the diameter of the pores was the limiting factor of the samples fabricated in the course of this Thesis to use them for biosensing purposes. Therefore, we are working on increasing the diameter of such pores. However, such small diameter could be beneficial for other kind of assays in which the porous substrate can be combined with the so-called molecular gates. In this approach, bioreceptors are covering the pores, not inside them, and the pores are filled with small molecules or particles. When the biorecognition

occurs, the bioreceptors change their conformation and release to the medium the content of the pores. This provokes a decrease of the effective refractive index of the porous substrate that can be used for sensing purposes. In our case, particles with a high refractive index, such as TiO_2 nanoparticles employed for the functionalisation of girdle bands, are planned to be used to fill the pores to amplify the biodetection signal. Some tests were made in this respect, but their optimisation is still ongoing.

The second studied material was the electrospun NFs layers. As explained in Chapter 3, the final goal of OPTONANOSENS project was detecting ricin in real samples. It is already demonstrated the suitability of NFs layers for biosensing purposes and a valid and versatile biofunctionalisation protocol using recombinant protein A/G and antibodies was developed, although optimisations are still being studied. The next step is replacing anti-BSA antibodies by anti-ricin antibodies to perform the biodetection experiments of ricin. These experiments must be carried out in collaboration with INTA-Campus "La Marañosa" because their laboratories allow the manipulation of biological agents from risk group 2. Since the optical setup must be taken from NTC-UPV to INTA-Campus "La Marañosa", the Covid restrictions forced the suspension of these assays but they are expected to be resumed in a near future.

Concerning the commercial polycarbonate TEMs, some tests were performed placing the membrane directly in contact with an optical fibre and using the resulting complex as a probe to perform measurements directly inside liquids. Although some results have been obtained yet, the assemble of the optical probe and the TEM must be optimised to avoid movements of the latter during the measurements. Additionally, optimisations of the optical response of these structures are being studied. One approach is the evaporation of a layer of gold over the structure as previously done with the NFs layers.

The last studied porous material was the girdle band of the diatoms. The demonstration of its potential as optical transducers based on their sPhC optical response paves the way for the development of optical biosensors at a low cost and with a highly preserved performance. For this reason, new experiments in which bioreceptors are attached to the surface of girdle bands to carry out biosensing experiments are planned. Additionally, the assemble of a flow chamber over the structures would allow the continuous and real-time detection of refractive index changes or the presence of a certain analyte in the medium.

In parallel with the study of such porous materials, the study of bacterial nanocellulose as a suitable porous material was also carried out. Following the same reasoning applied for diatoms, this porous material is naturally produced by bacteria, which would avoid the use of any fabrication technique. Additionally, this material shows outstanding features such as a high hydrophilicity and a high mechanical strength, among others [197]. However, such high hydrophilicity provokes the swelling of the structure and hence, could hinder optical sensing experiments. Therefore, the characterisation of its optical response and the optimisation of a protocol to stabilise its structure must be done, as it was done with NFs layers. Depending on the results obtained once carried out those steps, the utility of bacterial nanocellulose for the development of optical (bio)sensors

based on their optical response will be studied.

Author Scientific Contributions

Journal articles

P. Martínez-Pérez, S. Ponce-Alcántara, N. Murillo, A. Pérez-Márquez, J. Maudes, I. Peraile, L. González-López, M. Gil-García, P. Lorenzo-Lozano, and J. García-Rupérez, "Label-Free Optical Biosensing Using Low-Cost Electrospun Polymeric Nanofibers," *Chemosensors*, vol. 8, no. 4, pp. 119, 2020. DOI: 10.3390/chemosensors8040119.

P. Martínez-Pérez, M. Gómez-Gómez, T. Angelova, A. Griol, J. Hurtado, L. Bellieres, and J. García-Rupérez, "Continuous Detection of Increasing Concentrations of Thrombin Employing a Label-Free Photonic Crystal Aptasensor," *Micromachines*, vol. 11, no. 5, pp. 464, 2020. DOI: 10.3390/mi11050464.

P. Martínez-Pérez and J. García-Rupérez, "Commercial polycarbonate track-etched membrane as substrate for low-cost optical sensors," *Beilstein J. Nanotechnol.*, vol. 10, pp. 677-683, 2019. DOI: 10.3762/bjnano.10.67.

S. Ponce-Alcántara, **P. Martínez-Pérez**, A. Pérez-Márquez, J. Maudes, N. Murillo, and J. García-Rupérez, "Stabilization of Polymeric Nanofibers Layers for Use as Real-Time and In-Flow Photonic Sensors," *Sensors*, vol. 19, pp. 3847, 2019. DOI: 10.3390/s19183847.

J. Sabek, **P. Martínez-Pérez** and J. García-Rupérez, "Computational binding study of cardiac troponin I antibody towards cardiac versus skeletal troponin I," *Comput. Biol. Chem.*, vol. 80, pp. 147-151, 2019. DOI: 10.1016/j.compbiolchem.2019.04.002.

D. Martín-Sánchez, S. Ponce-Alcántara, **P. Martínez-Pérez** and J. García-Rupérez, "Macropore Formation and Pore Morphology Characterization of Heavily Doped p-Type Porous Silicon," *J. Electrochem. Soc.*, vol. 166, no. 2, pp. B9-B12, 2019. DOI: 10.1149/2.0051902jes.

Conference Proceedings

P. Martínez-Pérez, S. Ponce-Alcántara, N. Murillo, A. Pérez-Márquez, J. Maudes, I. Peraile, L. González-López, M. Gil-García, P. Lorenzo-Lozano, and J. García-Rupérez, "Low-cost electrospun nanofibers for label-free and real-time optical biodetection purposes," in *Proc. SPIE 11658, Nanoscale*

Imaging, Sensing, and Actuation for Biomedical Applications XVIII, online, March 2021, pp. 116580E. DOI: 10.1117/12.2576527.

P. Martínez-Pérez, M. Gómez-Gómez, L. Torrijos-Morán, T. Angelova, A. Griol, J. Hurtado, L. Bellieres, and J. García-Rupérez, "1D Periodic Corrugated Waveguides for Real-Time Detection of Increasing Concentrations of Thrombin," in *OSA Advanced Photonics Congress (AP) 2020 (IPR, NP, NOMA, Networks, PVLED, PSC, SPPCom, SOF)*, online, L. Caspani, A. Tauke-Pedretti, F. Leo, and B. Yang, Eds., July 2020.

P. Martínez-Pérez and J. García-Rupérez, "Commercial Polycarbonate Filtration Membranes as Optical Sensors," presented at the 41st Photonics and Electromagnetics Research Symposium (PIERS 2019), Rome, Italy, June 17-20, 2019.

J. García-Rupérez, L. Torrijos-Morán, M. Gómez-Gómez, **P. Martínez-Pérez**, and S. Ponce-Alcántara, "High performance photonic biosensors based on periodic configurations," in *Proceedings of the SPIE 11689, Integrated Optics: Devices, Materials, and Technologies XXV*, online, March 2021, pp. 1168907. DOI: 10.1117/12.2576401.

L. Torrijos-Morán, **P. Martínez-Pérez**, and J. García-Rupérez, "Real-time functionalization and biosensing in subwavelength grating bimodal waveguides," presented at the *22nd European Conference on Integrated Optics (ECIO 2020)*, Paris, France, June 23-25, 2020.

P. Martínez-Pérez and J. García-Rupérez, "Commercial Polycarbonate Track-Etched Membranes as Optical Chemical Sensors," in *Proc. 5th International Electronic Conference on Sensors and Applications (ECSA-5)*, online, November 15-30, 2018. DOI: 10.3390/ecsa-5-05716.

J. Sabek, **P. Martínez-Pérez** and J. García-Rupérez, "Theoretical and computational study of the affinity of cardiac versus skeletal troponin I towards cardiac troponin I antibody," *Proc. 5th International Electronic Conference on Sensors and Applications (ECSA-5)*, online, November 15-30, 2018. DOI: 10.3390/ecsa-5-05719.

J. Sabek, J., **P. Martínez-Pérez** and J. García-Rupérez, "Theoretical and computational study of the affinity of cardiac versus skeletal troponin I towards cardiac troponin I antibody," presented at *XII International Workshop on Sensors and Molecular Recognition*, Burjassot, Valencia, Spain, July 5-6, 2018.

J. García-Rupérez, S. Ponce-Alcántara, D. Ortiz de Zárate, R. Caroselli, F. Prats, A. Ruiz-Tórtola, D. Martín-Sánchez, and **P. Martínez-Pérez**, "Nanophotonic sensing technology for high sensitivity analysis of water resources," in *Proc. HydroSenSoft 2017*, Madrid, Spain, February 28 - March 3, 2017, pp.297-299.

Research stay

Natural and Artificial Photonic Structures and Devices (NAPS) group. International Iberian Nanotechnology Laboratory, Braga (Portugal) 18^{th} January 2021 - 25th April 2021

List of Figures

List of Tables

Bibliography

[1] C. Karunakaran, R. Rajkumar, and K. Bhargava, "Introduction to Biosensors," *Biosens. Bioelectron.* Elsevier, 2015, pp. 1–68. DOI: 10.1016/B978-0-12-803100-1.00001-3.

[2] L. C. Clark, "Monitor and control of blood and tissue oxygen tensions," *Am. Soc. Artif. Intern. Organs*, vol. 2, no. 1, pp. 41–48, 1956. DOI: 10.1016/S0096-5588(20)30126-4.

[3] L. C. Clark and C. Lyons, "Electrode systems for continuous monitoring in cardiovascular surgery," *Ann. N. Y. Acad. Sci.*, vol. 102, no. 1, pp. 29–45, 1962. DOI: 10.1111/j.1749-6632.1962.tb13623.x.

[4] J. D. Newman and A. P. F. Turner, "Historical Perspective of Biosensor and Biochip Development," *Handb. Biosens. Biochips*, Chichester, UK: John Wiley & Sons, Ltd, 2008. DOI: 10.1002/9780470061565.hbb002.

[5] C. Griesche and A. J. Baeumner, "Biosensors to support sustainable agriculture and food safety," *TrAC Trends Anal. Chem.*, vol. 128, p. 115 906, 2020. DOI: 10.1016/j.trac.2020.115906.

[6] M. Pohanka, "Biosensors commercial off the shelf in biological warfare attack," *Commer. Biosens. Their Appl.* Elsevier, 2020, pp. 287–300. DOI: 10.1016/B978-0-12-818592-6.00011-6.

[7] C. Justino, A. Duarte, and T. Rocha-Santos, "Recent Progress in Biosensors for Environmental Monitoring: A Review," *Sensors*, vol. 17, no. 12, p. 2918, 2017. DOI: 10.3390/s17122918.

[8] N. Bhalla, P. Jolly, N. Formisano, and P. Estrela, "Introduction to biosensors," *Essays Biochem.*, vol. 60, no. 1, pp. 1–8, 2016. DOI: 10.1042/EBC20150001.

[9] H. H. Nguyen, S. H. Lee, U. J. Lee, C. D. Fermin, and M. Kim, "Immobilized enzymes in biosensor applications," *Materials (Basel).*, vol. 12, no. 1, 2019. DOI: 10.3390/ma12010121.

[10] B. Chatterjee, S. J. Das, A. Anand, and T. K. Sharma, "Nanozymes and aptamer-based biosensing," *Mater. Sci. Energy Technol.*, vol. 3, pp. 127–135, 2020. DOI: 10.1016/j.mset.2019.08.007.

[11] C. Wang, D. Jin, Y. Yu, L. Tang, Y. Sun, Z. Sun, and G.-J. Zhang, "A Dual Antibody-modified Nanochannel Biosensor for Capture and Identification of Exosomes," *Sensors Actuators B Chem.*, vol. 314, p. 128 056, 2020. DOI: 10.1016/j.snb.2020.128056.

[12] D. Çimen, N. Bereli, S. Günaydın, and A. Denizli, "Detection of cardiac troponin-I by optic biosensors with immobilized anti-cardiac troponin-I monoclonal antibody," *Talanta*, vol. 219, p. 121 259, 2020. DOI: 10.1016/j.talanta.2020.121259.

[13] Y. Hillman, J. Gershberg, D. Lustiger, D. Even, D. Braverman, Y. Dror, I. Ashur, S. Vernick, N. Sal-Man, and Y. Wine, "Monoclonal Antibody-Based Biosensor for Point-of-Care Detection of Type III Secretion System Expressing Pathogens," *Anal. Chem.*, vol. 93, no. 2, pp. 928–935, 2021. DOI: 10.1021/acs.analchem.0c03621.

[14] S. Minchin and J. Lodge, "Understanding biochemistry: Structure and function of nucleic acids," *Essays Biochem.*, vol. 63, no. 4, pp. 433–456, 2019. DOI: 10.1042/EBC20180038.

[15] K. V, "DNA Biosensors-A Review," *J. Bioeng. Biomed. Sci.*, vol. 07, no. 02, 2017. DOI: 10.4172/2155-9538.1000222.

[16] Y. Zhang, B. S. Lai, and M. Juhas, "Recent advances in aptamer discovery and applications," *Molecules*, vol. 24, no. 5, 2019. DOI: 10.3390/molecules24050941.

[17] N. Komarova and A. Kuznetsov, "Inside the Black Box: What Makes SELEX Better?" *Molecules*, vol. 24, no. 19, p. 3598, 2019. DOI: 10.3390/molecules24193598.

[18] S.-G. Woo, S.-J. Moon, S. K. Kim, T. H. Kim, H. S. Lim, G.-H. Yeon, B. H. Sung, C.-H. Lee, S.-G. Lee, J. H. Hwang, and D.-H. Lee, "A designed whole-cell biosensor for live diagnosis of gut inflammation through nitrate sensing," *Biosens. Bioelectron.*, vol. 168, p. 112 523, 2020. DOI: 10.1016/j.bios.2020.112523.

[19] F. A. Arris, A. M. Benoudjit, F. Sanober, and W. W. A. Wan Salim, "Characterization of electrochemical transducers for biosensor applications," *Multifaceted Protoc. Biotechnol.* Springer Singapore, 2019, pp. 119–137. DOI: 10.1007/978-981-13-2257-0_11.

[20] J. L. Hammond, N. Formisano, P. Estrela, S. Carrara, and J. Tkac, "Electrochemical biosensors and nanobiosensors," *Essays Biochem.*, vol. 60, no. 1, pp. 69–80, 2016. DOI: 10.1042/EBC20150008.

[21] A. Shons, F. Dorman, and J. Najarian, "An immunospecific microbalance," *J. Biomed. Mater. Res.*, vol. 6, no. 6, pp. 565–570, 1972. DOI: 10.1002/jbm.820060608.

[22] M. Pohanka, "The piezoelectric biosensors: Principles and applications, a review," *Int. J. Electrochem. Sci.*, vol. 12, no. 1, pp. 496–506, 2017. DOI: 10.20964/2017.01.44.

[23] B. Danielsson and K. Mosbach, "Enzyme Thermistors," *Methods Enzymol.*, vol. 137, no. C, pp. 181–197, 1988. DOI: 10.1016/0076-6879(88)37018-7.

[24] Y. Zhang and S. Tadigadapa, "Calorimetric biosensors with integrated microfluidic channels," *Biosens. Bioelectron.*, vol. 19, no. 12, pp. 1733–1743, 2004. DOI: 10.1016/j.bios.2004.01.009.

[25] X. Liu, S. Cheng, H. Liu, S. Hu, D. Zhang, and H. Ning, "A survey on gas sensing technology," *Sensors (Switzerland)*, vol. 12, no. 7, pp. 9635–9665, 2012. DOI: 10.3390/s120709635.

[26] C. Chen and J. Wang, "Optical biosensors: An exhaustive and comprehensive review," *Analyst*, vol. 145, no. 5, pp. 1605–1628, 2020. DOI: 10.1039/c9an01998g.

[27] G. Zanchetta, R. Lanfranco, F. Giavazzi, T. Bellini, and M. Buscaglia, "Emerging applications of label-free optical biosensors," *Nanophotonics*, vol. 6, no. 4, pp. 627–645, 2017. DOI: 10.1515/nanoph-2016-0158.

[28] R. Peltomaa, B. Glahn-Martínez, E. Benito-Peña, and M. Moreno-Bondi, "Optical Biosensors for Label-Free Detection of Small Molecules," *Sensors*, vol. 18, no. 12, p. 4126, 2018. DOI: 10.3390/s18124126.

[29] A. M. Shrivastav, U. Cvelbar, and I. Abdulhalim, "A comprehensive review on plasmonic-based biosensors used in viral diagnostics," *Commun. Biol.*, vol. 4, no. 1, p. 70, 2021. DOI: 10.1038/s42003-020-01615-8.

[30] M. Chen, D. Liu, X. Du, K. H. Lo, S. Wang, B. Zhou, and H. Pan, "2D materials: Excellent substrates for surface-enhanced Raman scattering (SERS) in chemical sensing and biosensing," *TrAC Trends Anal. Chem.*, vol. 130, p. 115 983, 2020. DOI: 10.1016/j.trac.2020.115983.

[31] D. Rho, C. Breaux, and S. Kim, "Label-Free Optical Resonator-Based Biosensors," *Sensors*, vol. 20, no. 20, p. 5901, 2020. DOI: 10.3390/s20205901.

[32] D. Duval and L. M. Lechuga, "Optical Waveguide Biosensors," *Photonics*, vol. 4, Wiley, 2015, pp. 323–365. DOI: 10.1002/9781119011804.ch8.

[33] W. Wang, "A Review of Optical Waveguide Biosensor Especially in Diamond Waveguide," *2020 Int. Conf. Artif. Intell. Electromechanical Autom.*, IEEE, 2020, pp. 189–192. DOI: 10.1109/AIEA51086.2020.00047.

[34] H. Inan, M. Poyraz, F. Inci, M. A. Lifson, M. Baday, B. T. Cunningham, and U. Demirci, "Photonic crystals: emerging biosensors and their promise for point-of-care applications," *Chem. Soc. Rev.*, vol. 46, no. 2, pp. 366–388, 2017. DOI: 10.1039/C6CS00206D.

[35] R. Chhasatia, M. J. Sweetman, F. J. Harding, M. Waibel, T. Kay, H. Thomas, T. Loudovaris, and N. H. Voelcker, "Non-invasive, in vitro analysis of islet insulin production enabled by an optical porous silicon biosensor," *Biosens. Bioelectron.*, vol. 91, no. September 2016, pp. 515–522, 2017. DOI: 10.1016/j.bios.2017.01.004.

[36] R. Chhasatia, M. J. Sweetman, B. Prieto-Simon, and N. H. Voelcker, "Performance optimisation of porous silicon rugate filter biosensor for the detection of insulin," *Sensors Actuators B Chem.*, vol. 273, pp. 1313–1322, 2018. DOI: 10.1016/j.snb.2018.07.021.

[37] S. Zhuo, M. Xun, M. Li, X. Kong, R. Shao, T. Zheng, D. Pan, J. Li, and Q. Li, "Rapid and label-free optical assay of S-layer protein with high sensitivity using TiO2-coated porous silicon-based microfluidic biosensor," *Sensors Actuators B Chem.*, vol. 321, p. 128 524, 2020. DOI: 10.1016/j.snb.2020.128524.

[38] M. Yaghoubi, F. Rahimi, B. Negahdari, A. H. Rezayan, and A. Shafiekhani, "A lectin-coupled porous silicon-based biosensor: label-free optical detection of bacteria in a real-time mode," *Sci. Rep.*, vol. 10, no. 1, p. 16 017, 2020. DOI: 10.1038/s41598-020-72457-x.

[39] N. H. Maniya and D. N. Srivastava, "Fabrication of porous silicon based label-free optical biosensor for heat shock protein 70 detection," *Mater. Sci. Semicond. Process.*, vol. 115, p. 105 126, 2020. DOI: 10.1016/j.mssp.2020.105126.

[40] Y. Zhao, G. Gaur, S. T. Retterer, P. E. Laibinis, and S. M. Weiss, "Flow-through porous silicon membranes for real-time label-free biosensing," *Anal. Chem.*, vol. 88, no. 22, pp. 10 940–10 948, 2016. DOI: 10.1021/acs.analchem.6b02521.

[41] G. A. Rodriguez, S. Hu, and S. M. Weiss, "Porous silicon ring resonator for compact, high sensitivity biosensing applications," *Opt. Express*, vol. 23, no. 6, p. 7111, 2015. DOI: 10.1364/OE.23.007111.

[42] G. A. Rodriguez, D. Aurelio, M. Liscidini, and S. M. Weiss, "Bloch surface wave ring resonator based on porous silicon," *Appl. Phys. Lett.*, vol. 115, no. 1, p. 011 101, 2019. DOI: 10.1063/1.5093435.

[43] T. H. Talukdar, G. D. Allen, I. Kravchenko, and J. D. Ryckman, "Single-mode porous silicon waveguide interferometers with unity confinement factors for ultra-sensitive surface adlayer sensing," *Opt. Express*, vol. 27, no. 16, p. 22 485, 2019. DOI: 10.1364/OE.27.022485.

[44] P. Azuelos, P. Girault, N. Lorrain, Y. Dumeige, L. Bodiou, L. Poffo, M. Guendouz, M. Thual, and J. Charrier, "Optimization of porous silicon waveguide design for micro-ring resonator sensing applications," *J. Opt.*, vol. 20, no. 8, p. 085 301, 2018. DOI: 10.1088/2040-8986/aad01b.

[45] N. Abu-Thabit and E. Ratemi, "Hybrid Porous Silicon Biosensors Using Plasmonic and Fluorescent Nanomaterials: A Mini Review," *Front. Chem.*, vol. 8, p. 454, 2020. DOI: 10.3389/fchem.2020.00454.

[46] L. Pla, S. Santiago-Felipe, M. Á. Tormo-Mas, J. Pemán, F. Sancenón, E. Aznar, and R. Martínez-Máñez, "Aptamer-Capped nanoporous anodic alumina for Staphylococcus aureus detection," *Sensors Actuators B Chem.*, vol. 320, p. 128 281, 2020. DOI: 10.1016/j.snb.2020.128281.

[47] L. Pol, L. K. Acosta, J. Ferré-Borrull, and L. F. Marsal, "Aptamer-Based Nanoporous Anodic Alumina Interferometric Biosensor for Real-Time Thrombin Detection," *Sensors*, vol. 19, no. 20, p. 4543, 2019. DOI: 10.3390/s19204543.

[48] P. Kapruwan, L. K. Acosta, J. Ferré-Borrull, and L. F. Marsal, "Optical Platform to Analyze a Model Drug-Loading and Releasing Profile Based on Nanoporous Anodic Alumina Gradient Index Filters," *Nanomaterials*, vol. 11, no. 3, p. 730, 2021. DOI: 10.3390/nano11030730.

[49] R. Zegadi, N. Lorrain, L. Bodiou, M. Guendouz, L. Ziet, and J. Charrier, "Enhanced mid-infrared gas absorption spectroscopic detection using chalcogenide or porous germanium waveguides," *J. Opt.*, vol. 23, no. 3, p. 035 102, 2021. DOI: 10.1088/2040-8986/abdf69.

[50] N. Sandhyarani, "Surface modification methods for electrochemical biosensors," *Electrochem. Biosens.* Elsevier, 2019, pp. 45–75. DOI: 10.1016/B978-0-12-816491-4.00003-6.

[51] M. Oliverio, S. Perotto, G. C. Messina, L. Lovato, and F. De Angelis, "Chemical Functionalization of Plasmonic Surface Biosensors: A Tutorial Review on Issues, Strategies, and Costs," *ACS Appl. Mater. Interfaces*, vol. 9, no. 35, pp. 29 394–29 411, 2017. DOI: 10.1021/acsami.7b01583.

[52] G. T. Hermanson, "The Reactions of Bioconjugation," *Bioconjugate Tech.* Elsevier, 2013, pp. 229–258. DOI: 10.1016/B978-0-12-382239-0.00003-0.

[53] P. Vukusic and J. R. Sambles, "Photonic structures in biology," *Nature*, vol. 424, no. 6950, pp. 852–855, 2003. DOI: 10.1038/nature01941.

[54] A. Uhlir, "Electrolytic Shaping of Germanium and Silicon," *Bell Syst. Tech. J.*, vol. 35, no. 2, pp. 333–347, 1956. DOI: 10.1002/j.1538-7305.1956.tb02385.x.

[55] Y. Watanabe, Y. Arita, T. Yokoyama, and Y. Igarashi, "Formation and Properties of Porous Silicon and Its Application," *J. Electrochem. Soc.*, vol. 122, no. 10, pp. 1351–1355, 1975. DOI: 10.1149/1.2134015.

[56] L. T. Canham, "Silicon quantum wire array fabrication by electrochemical and chemical dissolution of wafers," *Appl. Phys. Lett.*, vol. 57, no. 10, pp. 1046–1048, 1990. DOI: 10.1063/1.103561.

[57] V. Lehmann and U. Gösele, "Porous silicon formation: A quantum wire effect," *Appl. Phys. Lett.*, vol. 58, no. 8, pp. 856–858, 1991. DOI: 10.1063/1.104512.

[58] O. Bisi, S. Ossicini, and L. Pavesi, *Porous silicon: A quantum sponge structure for silicon based optoelectronics*, 2000. DOI: 10.1016/S0167-5729(99)00012-6.

[59] M. Sailor, J. Heinrich, and J. Lauerhaas, "Luminescent porous silicon: Synthesis, chemistry, and applications," *Stud. Surf. Sci. Catal.* C, vol. 103, Elsevier, 1997, pp. 209–235. DOI: 10.1016/S0167-2991(97)81104-4.

[60] M. J. Sailor, *Porous Silicon in Practice: Preparation, Characterization and Applications*. Weinheim, Germany: Wiley-VCH Verlag GmbH & Co. KGaA, 2012. DOI: 10.1002/9783527641901.

[61] J. Ding, J. Zhang, J. Li, D. Li, C. Xiao, H. Xiao, H. Yang, X. Zhuang, and X. Chen, "Electrospun polymer biomaterials," *Prog. Polym. Sci.*, vol. 90, pp. 1–34, 2019. DOI: 10.1016/j.progpolymsci.2019.01.002.

[62] V. S. Lin, "A Porous Silicon-Based Optical Interferometric Biosensor," *Science (80-.).*, vol. 278, no. 5339, pp. 840–843, 1997. DOI: 10.1126/science.278.5339.840.

[63] S. Mariani, L. M. Strambini, and G. Barillaro, "Femtomole Detection of Proteins Using a Label-Free Nanostructured Porous Silicon Interferometer for Perspective Ultrasensitive Biosensing," *Anal. Chem.*, vol. 88, no. 17, pp. 8502–8509, 2016. DOI: 10.1021/acs.analchem.6b01228.

[64] K. Urmann, J.-G. Walter, T. Scheper, and E. Segal, "Label-Free Optical Biosensors Based on Aptamer-Functionalized Porous Silicon Scaffolds," *Anal. Chem.*, vol. 87, no. 3, pp. 1999–2006, 2015. DOI: 10.1021/ac504487g.

[65] T. Tieu, M. Alba, R. Elnathan, A. Cifuentes-Rius, and N. H. Voelcker, "Advances in Porous Silicon-Based Nanomaterials for Diagnostic and Therapeutic Applications," *Adv. Ther.*, vol. 2, no. 1, p. 1 800 095, 2019. DOI: 10.1002/adtp.201800095.

[66] B. Deng, Y. Lin, C. Wang, F. Li, Z. Wang, H. Zhang, X.-F. Li, and X. C. Le, "Aptamer binding assays for proteins: The thrombin example—A review," *Anal. Chim. Acta*, vol. 837, pp. 1–15, 2014. DOI: 10.1016/j.aca.2014.04.055.

[67] J. T. Crawley, S. Zanardelli, C. K. Chion, and D. A. Lane, "The central role of thrombin in hemostasis," *J. Thromb. Haemost.*, vol. 5, no. SUPPL. 1, pp. 95–101, 2007. DOI: 10.1111/j.1538-7836.2007.02500.x.

[68] K. G. Mann, K. Brummel, and S. Butenas, "What is all that thrombin for?" *J. Thromb. Haemost.*, vol. 1, no. 7, pp. 1504–1514, 2003. DOI: 10.1046/j.1538-7836.2003.00298.x.

[69] A. S. Wolberg and R. A. Campbell, "Thrombin generation, fibrin clot formation and hemostasis," *Transfus. Apher. Sci.*, vol. 38, no. 1, pp. 15–23, 2008. DOI: 10.1016/j.transci.2007.12.005.

[70] K. E. Brummel, S. G. Paradis, S. Butenas, and K. G. Mann, "Thrombin functions during tissue factor-induced blood coagulation," *Blood*, vol. 100, no. 1, pp. 148–152, 2002. DOI: 10.1182/blood.V100.1.148.

[71] M. F. Hockin, K. C. Jones, S. J. Everse, and K. G. Mann, "A model for the stoichiometric regulation of blood coagulation," *J. Biol. Chem.*, vol. 277, no. 21, pp. 18 322–18 333, 2002. DOI: 10.1074/jbc.M201173200.

[72] C. M. Danforth, T. Orfeo, S. J. Everse, K. G. Mann, and K. E. Brummel-Ziedins, "Defining the boundaries of normal thrombin generation: Investigations into hemostasis," *PLoS One*, vol. 7, no. 2, P. J. Lenting, Ed., e30385, 2012. DOI: 10.1371/journal.pone.0030385.

[73] H. ten Cate and H. C. Hemker, "Thrombin Generation and Atherothrombosis: What Does the Evidence Indicate?" *J. Am. Heart Assoc.*, vol. 5, no. 8, 2016. DOI: 10.1161/JAHA.116.003553.

[74] D. Tripathy, A. Sanchez, X. Yin, J. Luo, J. Martinez, and P. Grammas, "Thrombin, a mediator of cerebrovascular inflammation in AD and hypoxia," *Front. Aging Neurosci.*, vol. 5, no. MAY, p. 19, 2013. DOI: 10.3389/fnagi.2013.00019.

[75] M. Z. Wojtukiewicz, D. Hempel, E. Sierko, S. C. Tucker, and K. V. Honn, "Thrombin—Unique coagulation system protein with multifaceted impacts on cancer and metastasis," *Cancer Metastasis Rev.*, vol. 35, no. 2, pp. 213–233, 2016. DOI: 10.1007/s10555-016-9626-0.

[76] A. S. Remiker and J. S. Palumbo, "Mechanisms coupling thrombin to metastasis and tumorigenesis," *Thromb. Res.*, vol. 164, S29–S33, 2018. DOI: 10.1016/j.thromres.2017.12.020.

[77] R. C. F. Duarte, C. N. Ferreira, D. R. A. Rios, H. J. dos Reis, and M. d. G. Carvalho, "Thrombin generation assays for global evaluation of the hemostatic system: perspectives and limitations," *Rev. Bras. Hematol. Hemoter.*, vol. 39, no. 3, pp. 259–265, 2017. DOI: 10.1016/j.bjhh.2017.03.009.

[78] J. Kintigh, P. Monagle, and V. Ignjatovic, "A review of commercially available thrombin generation assays," *Res. Pract. Thromb. Haemost.*, vol. 2, no. 1, pp. 42–48, 2018. DOI: 10.1002/rth2.12048.

[79] M. Mohammadi Aria, A. Erten, and O. Yalcin, "Technology Advancements in Blood Coagulation Measurements for Point-of-Care Diagnostic Testing," *Front. Bioeng. Biotechnol.*, vol. 7, p. 395, 2019. DOI: 10.3389/fbioe.2019.00395.

[80] X. Chen, T. Li, X. Tu, and L. Luo, "Label-free fluorescent aptasensor for thrombin detection based on exonuclease I assisted target recycling and SYBR Green I aided signal amplification," *Sensors Actuators, B Chem.*, vol. 265, pp. 98–103, 2018. DOI: 10.1016/j.snb.2018.02.099.

[81] H. Cho, B. R. Baker, S. Wachsmann-Hogiu, C. V. Pagba, T. A. Laurence, S. M. Lane, L. P. Lee, and J. B. Tok, "Aptamer-Based SERRS Sensor for Thrombin Detection," *Nano Lett.*, vol. 8, no. 12, pp. 4386–4390, 2008. DOI: 10.1021/nl802245w.

[82] I. Russo Krauss, A. Merlino, C. Giancola, A. Randazzo, L. Mazzarella, and F. Sica, "Thrombin–aptamer recognition: a revealed ambiguity," *Nucleic Acids Res.*, vol. 39, no. 17, pp. 7858–7867, 2011. DOI: 10.1093/nar/gkr522.

[83] A. T. Ponce and K. L. Hong, "A Mini-Review: Clinical Development and Potential of Aptamers for Thrombotic Events Treatment and Monitoring," *Biomedicines*, vol. 7, no. 3, p. 55, 2019. DOI: 10.3390/biomedicines7030055.

[84] J. Zhang, R. R. O. Loo, and J. A. Loo, "Structural Characterization of a Thrombin-Aptamer Complex by High Resolution Native Top-Down Mass Spectrometry," *J. Am. Soc. Mass Spectrom.*, vol. 28, no. 9, pp. 1815–1822, 2017. DOI: 10.1007/s13361-017-1751-7.

[85] M. J. Sailor, "Fundamentals of Porous Silicon Preparation," *Porous Silicon Pract.* Weinheim, Germany: Wiley-VCH Verlag GmbH & Co. KGaA, 2012, pp. 1–42. DOI: 10.1002/9783527641901.ch1.

[86] V. C. Diculescu, A.-M. Chiorcea-Paquim, R. Eritja, and A. M. Oliveira-Brett, "Thrombin-Binding Aptamer Quadruplex Formation: AFM and Voltammetric Characterization," *J. Nucleic Acids*, vol. 2010, pp. 1–8, 2010. DOI: 10.4061/2010/841932.

[87] O. V. Kim, Z. Xu, E. D. Rosen, and M. S. Alber, "Fibrin Networks Regulate Protein Transport during Thrombus Development," *PLoS Comput. Biol.*, vol. 9, no. 6, A. D. McCulloch, Ed., e1003095, 2013. DOI: 10.1371/journal.pcbi.1003095.

[88] T. Urata, K. Fukami, T. Sakka, and Y. H. Ogata, "Pore formation in p-type silicon in solutions containing different types of alcohol," *Nanoscale Res. Lett.*, vol. 7, no. 1, p. 329, 2012. DOI: 10.1186/1556-276X-7-329.

[89] D. Martín-Sánchez, S. Ponce-Alcántara, P. Martínez-Pérez, and J. García-Rupérez, "Macropore Formation and Pore Morphology Characterization of Heavily Doped p-Type Porous Silicon," *J. Electrochem. Soc.*, vol. 166, no. 2, B9–B12, 2019. DOI: 10.1149/2.0051902jes.

[90] A. Loni, "Porous Silicon Formation by Anodization," *Handb. Porous Silicon*, Springer International Publishing, 2014, pp. 1–12. DOI: 10.1007/978-3-319-04508-5_2-1.

[91] M. R. Jimenéz-Vivanco, G. García, J. Carrillo, V. Agarwal, T. Díaz-Becerril, R. Doti, J. Faubert, and J. E. Lugo, "Porous Si-SiO2 based UV Microcavities," *Sci. Rep.*, vol. 10, no. 1, 2020. DOI: 10.1038/s41598-020-59001-7.

[92] C. Lai, X. Li, C. Liu, X. Guo, Z. Xiang, B. Xie, and L. Zou, "Improvement in gravimetric measurement for determining the porosity and thickness of porous silicon using an optimized solution," *Mater. Sci. Semicond. Process.*, vol. 26, no. 1, pp. 501–505, 2014. DOI: 10.1016/j.mssp.2014.05.046.

[93] F. A. Harraz, K. Kamada, K. Kobayashi, T. Sakka, and Y. H. Ogata, "Random Macropore Formation in p-Type Silicon in HF-Containing Organic Solutions," *J. Electrochem. Soc.*, vol. 152, no. 4, p. C213, 2005. DOI: 10.1149/1.1864292.

[94] D. N. Kumar, N. Pinker, and G. Shtenberg, "Inflammatory biomarker detection in milk using label-free porous SiO2 interferometer," *Talanta*, vol. 220, p. 121 439, 2020. DOI: 10.1016/j.talanta.2020.121439.

[95] I. Freidman and G. Shtenberg, "Porous Silicon Fabry–Pérot Interferometer Highly Sensitive Detection of Mycotoxins in Field Crops," *Opt. Sensors Sens. Congr. (ES, FTS, HISE, Sensors) (2019), Pap. STu2D.6*, The Optical Society, 2019, STu2D.6. DOI: 10.1364/sensors.2019.stu2d.6.

[96] H. Zhang, J. Lv, and Z. Jia, "Detection of ammonia-oxidizing bacteria (AOB) using a porous silicon optical biosensor based on a multilayered double bragg mirror structure," *Sensors (Switzerland)*, vol. 18, no. 1, p. 105, 2018. DOI: 10.3390/s18010105.

[97] R. Caroselli, S. Ponce-Alcántara, F. P. Quilez, D. M. Sánchez, L. T. Morán, A. G. Barres, L. Bellieres, H. Bandarenka, K. Girel, V. Bondarenko, and J. García-Rupérez, "Experimental study of the sensitivity of a porous silicon ring resonator sensor using continuous in-flow measurements," *Opt. Express*, vol. 25, no. 25, p. 31 651, 2017. DOI: 10.1364/oe.25.031651.

[98] R. Zhou, Z. Jia, X. Lv, and X. Huang, "The enhanced sensitivity of a porous silicon microcavity biosensor based on an angular spectrum using CdSe/ZnS quantum dots," *Sensors (Switzerland)*, vol. 19, no. 22, p. 4872, 2019. DOI: 10.3390/s19224872.

[99] M. J. Sailor, "Chemical Reactivity and Surface Chemistry of Porous Silicon," *Handb. Porous Silicon*, Springer International Publishing, 2017, pp. 1–20. DOI: 10.1007/978-3-319-04508-5_37-2.

[100] N. H. Maniya, "Recent advances in porous silicon based optical biosensors," *Rev. Adv. Mater. Sci.*, vol. 53, no. 1, pp. 49–73, 2018. DOI: 10.1515/rams-2018-0004.

[101] L. A. Huck, M. Hu, and J. M. Buriak, "Silicon-carbon bond formation on porous silicon," *Handb. Porous Silicon Second Ed.* Vol. 2-2, Springer International Publishing, 2018, pp. 1003–1014. DOI: 10.1007/978-3-319-71381-6_70.

[102] T. Jalkanen, E. Mäkilä, T. Sakka, J. Salonen, and Y. H. Ogata, "Thermally promoted addition of undecylenic acid on thermally hydrocarbonized porous silicon optical reflectors," *Nanoscale Res. Lett.*, vol. 7, no. 1, p. 311, 2012. DOI: 10.1186/1556-276X-7-311.

[103] R. Boukherroub, J. T. C. Wojtyk, D. D. M. Wayner, and D. J. Lockwood, "Thermal Hydrosilylation of Undecylenic Acid with Porous Silicon," *J. Electrochem. Soc.*, vol. 149, no. 2, H59, 2002. DOI: 10.1149/1.1432679.

[104] A. E. Pap, K. Kordás, G. Tóth, J. Levoska, A. Uusimäki, J. Vähäkangas, S. Leppävuori, and T. F. George, "Thermal oxidation of porous silicon: Study on structure," *Appl. Phys. Lett.*, vol. 86, no. 4, p. 041 501, 2005. DOI: 10.1063/1.1853519.

[105] A. A. El-Gamal, S. M. Ibrahim, and M. Amin, "Impact of thermal oxidation on the structural and optical properties of porous silicon microcavity," *Nanomater. Nanotechnol.*, vol. 7, 2017. DOI: 10.1177/1847980417735702.

[106] R. Cisneros, H. Pfeiffer, and C. Wang, "Oxygen absorption in free-standing porous silicon: A structural, optical and kinetic analysis," *Nanoscale Res. Lett.*, vol. 5, no. 4, pp. 686–691, 2010. DOI: 10.1007/s11671-010-9532-2.

[107] S. Mariani, L. Pino, L. M. Strambini, L. Tedeschi, and G. Barillaro, "10 000-Fold Improvement in Protein Detection Using Nanostructured Porous Silicon Interferometric Aptasensors," *ACS Sensors*, vol. 1, no. 12, pp. 1471–1479, 2016. DOI: 10.1021/acssensors.6b00634.

[108] M. Terracciano, L. De Stefano, N. Borbone, J. Politi, G. Oliviero, F. Nici, M. Casalino, G. Piccialli, P. Dardano, M. Varra, and I. Rea, "Solid phase synthesis of a thrombin binding aptamer on macroporous silica for label free optical quantification of thrombin," *RSC Adv.*, vol. 6, no. 90, pp. 86 762–86 769, 2016. DOI: 10.1039/C6RA18401D.

[109] B. Jalali and S. Fathpour, "Silicon photonics," *J. Light. Technol.*, vol. 24, no. 12, pp. 4600–4615, 2006. DOI: 10.1109/JLT.2006.885782.

[110] X. Chen, C. Li, and H. K. Tsang, "Device engineering for silicon photonics," *NPG Asia Mater.*, vol. 3, no. 1, pp. 34–40, 2011. DOI: 10.1038/asiamat.2010.194.

[111] S. Alt, "Photonic Integrated Circuit (PIC) Device Structures: Background, Fabrication Ecosystem, Relevance to Space Systems Applications, and Discussion of Related Radiation Effects," *Nasa*, 2016.

[112] Á. Ruiz-Tórtola, F. Prats-Quílez, D. González-Lucas, M.-J. Bañuls, Á. Maquieira, G. Wheeler, T. Dalmay, A. Griol, J. Hurtado, H. Bohlmann, R. Götzen, and J. García-Rupérez, "Experimental study of the evanescent-wave photonic sensors response in presence of molecular beacon conformational changes," *J. Biophotonics*, vol. 11, no. 10, e201800030, 2018. DOI: 10.1002/jbio.201800030.

[113] Á. Ruiz-Tórtola, F. Prats-Quílez, D. González-Lucas, M.-J. Bañuls, Á. Maquieira, G. Wheeler, T. Dalmay, A. Griol, J. Hurtado, and J. García-Rupérez, "High sensitivity and label-free oligonucleotides detection using photonic bandgap sensing structures biofunctionalized with molecular beacon probes," *Biomed. Opt. Express*, vol. 9, no. 4, p. 1717, 2018. DOI: 10.1364/BOE.9.001717.

[114] P. Schuck and H. Zhao, "The role of mass transport limitation and surface heterogeneity in the biophysical characterization of macromolecular binding processes by SPR biosensing.," *Methods Mol. Biol.*, vol. 627, pp. 15–54, 2010. DOI: 10.1007/978-1-60761-670-2_2.

[115] V. R. Manfrinato, L. Zhang, D. Su, H. Duan, R. G. Hobbs, E. A. Stach, and K. K. Berggren, "Resolution limits of electron-beam lithography toward the atomic scale," *Nano Lett.*, vol. 13, no. 4, pp. 1555–1558, 2013. DOI: 10.1021/nl304715p.

[116] Á. Ruiz-Tórtola, F. Prats-Quílez, D. González-Lucas, M.-J. Bañuls, Á. Maquieira, G. Wheeler, T. Dalmay, A. Griol, J. Hurtado, and J. García-Rupérez, "High sensitivity and label-free oligonucleotides detection using photonic bandgap sensing structures biofunctionalized with molecular beacon probes," *Biomed. Opt. Express*, vol. 9, no. 4, p. 1717, 2018. DOI: 10.1364/BOE.9.001717.

[117] I. Petrova, V. Konopsky, I. Nabiev, and A. Sukhanova, "Label-Free Flow Multiplex Biosensing via Photonic Crystal Surface Mode Detection," *Sci. Rep.*, vol. 9, no. 1, pp. 1–9, 2019. DOI: 10.1038/s41598-019-45166-3.

[118] A. Düzgün, A. Maroto, T. Mairal, C. O'Sullivan, and F. X. Rius, "Solid-contact potentiometric aptasensor based on aptamer functionalized carbon nanotubes for the direct determination of proteins," *Analyst*, vol. 135, no. 5, pp. 1037–1041, 2010. DOI: 10.1039/b926958d.

[119] A. Bekmurzayeva, K. Dukenbayev, M. Shaimerdenova, I. Bekniyazov, T. Ayupova, M. Sypabekova, C. Molardi, and D. Tosi, "Etched fiber bragg grating biosensor functionalized with aptamers for detection of thrombin," *Sensors (Switzerland)*, vol. 18, no. 12, 2018. DOI: 10.3390/s18124298.

[120] L. Coelho, J. M. Marques Martins de Almeida, J. L. Santos, P. A. da Silva Jorge, M. C. L. Martins, D. Viegas, and R. B. Queirós, "Aptamer-based fiber sensor for thrombin detection," *J. Biomed. Opt.*, vol. 21, no. 8, p. 087 005, 2016. DOI: 10.1117/1.jbo.21.8.087005.

[121] S. Arshavsky Graham, E. Boyko, R. Salama, and E. Segal, "Mass Transfer Limitations of Porous Silicon-Based Biosensors for Protein Detection," *ACS Sensors*, vol. 5, no. 10, pp. 3058–3069, 2020. DOI: 10.1021/acssensors.0c00670.

[122] N. Reta, A. Michelmore, C. P. Saint, B. Prieto-Simon, and N. H. Voelcker, "Label-Free Bacterial Toxin Detection in Water Supplies Using Porous Silicon Nanochannel Sensors," *ACS Sensors*, vol. 4, no. 6, pp. 1515–1523, 2019. DOI: 10.1021/acssensors.8b01670.

[123] J. Matulevicius, L. Kliucininkas, D. Martuzevicius, E. Krugly, M. Tichonovas, and J. Baltrusaitis, "Design and Characterization of Electrospun Polyamide Nanofiber Media for Air Filtration Applications," *J. Nanomater.*, vol. 2014, pp. 1–13, 2014. DOI: 10.1155/2014/859656.

[124] L. Wei, R. Sun, C. Liu, J. Xiong, and X. Qin, "Mass production of nanofibers from needleless electrospinning by a novel annular spinneret," *Mater. Des.*, vol. 179, p. 107 885, 2019. DOI: 10.1016/j.matdes.2019.107885.

[125] W.-E. Teo, R. Inai, and S. Ramakrishna, "Technological advances in electrospinning of nanofibers," *Sci. Technol. Adv. Mater.*, vol. 12, no. 1, p. 013 002, 2011. DOI: 10.1088/1468-6996/12/1/013002.

[126] Kenry and C. T. Lim, "Nanofiber technology: current status and emerging developments," *Prog. Polym. Sci.*, vol. 70, pp. 1–17, 2017. DOI: 10.1016/j.progpolymsci.2017.03.002.

[127] A. M. Al-Enizi, M. M. Zagho, and A. A. Elzatahry, "Polymer-based electrospun nanofibers for biomedical applications," *Nanomaterials*, vol. 8, no. 4, p. 259, 2018. DOI: 10.3390/nano8040259.

[128] J. S. Bonso, G. D. Kalaw, and J. P. Ferraris, "High surface area carbon nanofibers derived from electrospun PIM-1 for energy storage applications," *J. Mater. Chem. A*, vol. 2, no. 2, pp. 418–424, 2014. DOI: 10.1039/c3ta13779a.

[129] M. Najafi and M. W. Frey, "Electrospun nanofibers for chemical separation," *Nanomaterials*, vol. 10, no. 5, p. 982, 2020. DOI: 10.3390/nano10050982.

[130] S. Sundera Murthe, M. S. Mohamed Saheed, V. Perumal, M. S. Mohamed Saheed, and N. M. Mohamed, "Electrospun Nanofibers for Biosensing Applications," *Nanobiosensors Biomol. Target.* Elsevier, 2019, pp. 253–267. DOI: 10.1016/B978-0-12-813900-4.00011-7.

[131] A. Senthamizhan, B. Balusamy, and T. Uyar, "Recent progress on designing electrospun nanofibers for colorimetric biosensing applications," *Curr. Opin. Biomed. Eng.*, vol. 13, pp. 1–8, 2020. DOI: 10.1016/j.cobme.2019.08.002.

[132] A. Stafiniak, B. Boratyński, A. Baranowska-Korczyc, A. Szyszka, M. Ramiczek-Krasowska, J. Pramowska, K. Fronc, D. Elbaum, R. Paszkiewicz, and M. Tłaczała, "A novel electrospun ZnO nanofibers biosensor fabrication," *Sensors Actuators, B Chem.*, vol. 160, no. 1, pp. 1413–1418, 2011. DOI: 10.1016/j.snb.2011.09.087.

[133] K. Sawicka, P. Gouma, and S. Simon, "Electrospun biocomposite nanofibers for urea biosensing," *Sensors Actuators, B Chem.*, vol. 108, Elsevier, 2005, pp. 585–588. DOI: 10.1016/j.snb.2004.12.013.

[134] M. Williams and D. C. Sizemore, *Biologic, Chemical, and Radiation Terrorism Review*. StatPearls Publishing, 2019.

[135] G. J. Moran, D. A. Talan, and F. M. Abrahamian, "Biological Terrorism," *Infect. Dis. Clin. North Am.*, vol. 22, no. 1, pp. 145–187, 2008. DOI: 10.1016/j.idc.2007.12.003.

[136] O. Cenciarelli, "Use of Non-Pathogenic Biological Agents as Biological Warfare Simulants for the Development of a Stand-Off Detection System," *J. Microb. Biochem. Technol.*, vol. 06, no. 07, pp. 375–380, 2014. DOI: 10.4172/1948-5948.1000172.

[137] *Refractive Index of Polymers by Index « scientificpolymer.com.*

[138] S. R. Dhakate, B. Singla, M. Uppal, and R. B. Mathur, "Effect of processing parameters on morphology and thermal properties of electrospun polycarbonate nanofibers," *Adv. Mater. Lett.*, vol. 1, no. 3, pp. 200–204, 2010. DOI: 10.5185/amlett.2010.8148.

[139] T. Nitanan, P. Opanasopit, P. Akkaramongkolporn, T. Rojanarata, T. Ngawhirunpat, and P. Supaphol, "Effects of processing parameters on morphology of electrospun polystyrene nanofibers," *Korean J. Chem. Eng.*, vol. 29, no. 2, pp. 173–181, 2012. DOI: 10.1007/s11814-011-0167-5.

[140] P. Heikkilä and A. Harlin, "Parameter study of electrospinning of polyamide-6," *Eur. Polym. J.*, vol. 44, no. 10, pp. 3067–3079, 2008. DOI: 10.1016/j.eurpolymj.2008.06.032.

[141] H. Fong, I. Chun, and D. H. Reneker, "Beaded nanofibers formed during electrospinning," *Polymer (Guildf).*, vol. 40, no. 16, pp. 4585–4592, 1999. DOI: 10.1016/S0032-3861(99)00068-3.

[142] H. Li, C. Zhu, J. Xue, Q. Ke, and Y. Xia, "Enhancing the Mechanical Properties of Electrospun Nanofiber Mats through Controllable Welding at the Cross Points," *Macromol. Rapid Commun.*, vol. 38, no. 9, p. 1 600 723, 2017. DOI: 10.1002/marc.201600723.

[143] A. Tomasini and H. H. León-Santiesteban, "Nylon uses in biotechnology," *Biocomposites Des. Mech. Perform.* Elsevier Inc., 2015, pp. 319–346. DOI: 10.1016/B978-1-78242-373-7.00006-8.

[144] C. Silva, C. J. Silva, A. Zille, G. M. Guebitz, and A. Cavaco-Paulo, "Laccase immobilization on enzymatically functionalized polyamide 6,6 fibres," *Enzyme Microb. Technol.*, vol. 41, no. 6-7, pp. 867–875, 2007. DOI: 10.1016/j.enzmictec.2007.07.010.

[145] R. Gopal, S. Kaur, Z. Ma, C. Chan, S. Ramakrishna, and T. Matsuura, "Electrospun nanofibrous filtration membrane," *J. Memb. Sci.*, vol. 281, no. 1-2, pp. 581–586, 2006. DOI: 10.1016/j.memsci.2006.04.026.

[146] H. Na, Y. Zhao, C. Zhao, C. Zhao, and X. Yuan, "Effect of hot-press on electrospun poly(vinylidene fluoride) membranes," *Polym. Eng. Sci.*, vol. 48, no. 5, pp. 934–940, 2008. DOI: 10.1002/pen.21039.

[147] A. L. Viet, "Niobium Pentoxide Polymorphs By Electrospinning for Energy Conversion and Storage," Ph.D. dissertation, 2010, pp. 1–143.

[148] S. Sharma, H. Byrne, and R. J. O'Kennedy, "Antibodies and antibody-derived analytical biosensors," *Essays Biochem.*, vol. 60, no. 1, pp. 9–18, 2016. DOI: 10.1042/EBC20150002.

[149] W. Choe, T. A. Durgannavar, and S. J. Chung, "Fc-binding ligands of immunoglobulin G: An overview of high affinity proteins and peptides," *Materials (Basel).*, vol. 9, no. 12, 2016. DOI: 10.3390/ma9120994.

[150] I. Peraile, P. Lorenzo-Lozano, N. Murillo, J. Maudes, G. Rozas, L. González-López, J. C. Cabria, and M. Gil-García, "Biofunctionalization of nylon nanofibers to be used in immunobiosensor for biological warfare agents detecting.," *Glob. Prog. Appl. Microbiol. a Multidiscip. approach.* Badajoz: Formatex Research Center, 2018, pp. 18–22.

[151] P. Martínez-Pérez, M. Gómez-Gómez, T. Angelova, A. Griol, J. Hurtado, L. Bellieres, and J. García-Rupérez, "Continuous Detection of Increasing Concentrations of Thrombin Employing a Label-Free Photonic Crystal Aptasensor," *Micromachines*, vol. 11, no. 5, p. 464, 2020. DOI: 10.3390/mi11050464.

[152] C. S. Law, S. Y. Lim, A. D. Abell, N. H. Voelcker, and A. Santos, "Nanoporous Anodic Alumina Photonic Crystals for Optical Chemo- and Biosensing: Fundamentals, Advances, and Perspectives," *Nanomaterials*, vol. 8, no. 10, p. 788, 2018. DOI: 10.3390/nano8100788.

[153] M. M. Varma, "Polymer thin film structures for ultra-low cost biosensing," *Optik (Stuttg).*, vol. 123, no. 15, pp. 1400–1403, 2012. DOI: 10.1016/j.ijleo.2011.08.025.

[154] L. Ali, M. U. Mohammed, M. Khan, A. H. B. Yousuf, and M. H. Chowdhury, "High-Quality Optical Ring Resonator-Based Biosensor for Cancer Detection," *IEEE Sens. J.*, vol. 20, no. 4, pp. 1867–1875, 2020. DOI: 10.1109/JSEN.2019.2950664.

[155] N. A. Mohammed, M. M. Hamed, A. A. Khalaf, A. Alsayyari, and S. El-Rabaie, "High-sensitivity ultra-quality factor and remarkable compact blood components biomedical sensor based on nanocavity coupled photonic crystal," *Results Phys.*, vol. 14, p. 102 478, 2019. DOI: 10.1016/j.rinp.2019.102478.

[156] P. Apel, "Track etching technique in membrane technology," *Radiat. Meas.*, vol. 34, Pergamon, 2001, pp. 559–566. DOI: 10.1016/S1350-4487(01)00228-1.

[157] N. G. Sultanova, S. N. Kasarova, and I. D. Nikolov, "Characterization of optical properties of optical polymers," *Opt. Quantum Electron.*, vol. 45, no. 3, pp. 221–232, 2013. DOI: 10.1007/s11082-012-9616-6.

[158] R. H. Wilson, K. P. Nadeau, F. B. Jaworski, B. J. Tromberg, and A. J. Durkin, "Review of short-wave infrared spectroscopy and imaging methods for biological tissue characterization," *J. Biomed. Opt.*, vol. 20, no. 3, p. 030 901, 2015. DOI: 10.1117/1.jbo.20.3.030901.

[159] K. Aran, L. A. Sasso, N. Kamdar, and J. D. Zahn, "Irreversible, direct bonding of nanoporous polymer membranes to PDMS or glass microdevices," *Lab Chip*, vol. 10, no. 5, pp. 548–552, 2010. DOI: 10.1039/b924816a. arXiv: 15334406.

[160] J. García-Rupérez, V. Toccafondo, M. J. Bañuls, J. G. Castelló, A. Griol, S. Peransi-Llopis, and Á. Maquieira, "Label-free antibody detection using band edge fringes in SOI planar photonic crystal waveguides in the slow-light regime," *Opt. Express*, vol. 18, no. 23, p. 24 276, 2010. DOI: 10.1364/OE.18.024276.

[161] E. Sani and A. Dell'Oro, "Spectral optical constants of ethanol and isopropanol from ultraviolet to far infrared," *Opt. Mater. (Amst).*, vol. 60, pp. 137–141, 2016. DOI: 10.1016/j.optmat.2016.06.041.

[162] C. H. Ooi, E. Bormashenko, A. V. Nguyen, G. M. Evans, D. V. Dao, and N.-T. Nguyen, "Evaporation of Ethanol–Water Binary Mixture Sessile Liquid Marbles," *Langmuir*, vol. 32, no. 24, pp. 6097–6104, 2016. DOI: 10.1021/acs.langmuir.6b01272.

[163] S. Ponce-Alcántara, D. Martín-Sánchez, A. Pérez-Márquez, J. Maudes, N. Murillo, and J. García-Rupérez, "Optical sensors based on polymeric nanofibers layers created by electrospinning," *Opt. Mater. Express*, vol. 8, no. 10, p. 3163, 2018. DOI: 10.1364/OME.8.003163.

[164] Jin Liu, Xi Zhou, Zhi Qiao, Jianhao Zhang, Chenzhao Zhang, Tuowen Xiang, Lingling Shui, Yaocheng Shi, and Liu Liu, "Integrated Optical Chemical Sensor Based on an SOI Ring Resonator Using Phase-Interrogation," *IEEE Photonics J.*, vol. 6, no. 5, pp. 1–7, 2014. DOI: 10.1109/JPHOT.2014.2352973.

[165] E. Kosobrodova, R. T. Jones, A. Kondyurin, W. Chrzanowski, P. J. Pigram, D. R. Mckenzie, and M. M. Bilek, "Orientation and conformation of anti-CD34 antibody immobilised on untreated and plasma treated polycarbonate," *Acta Biomater.*, vol. 19, pp. 128–137, 2015. DOI: 10.1016/j.actbio.2015.02.027.

[166] R. Paoli, M. Bulwan, O. Castaño, E. Engel, J. C. Rodriguez-Cabello, A. Homs-Corbera, and J. Samitier, "Layer-by-layer modification effects on a nanopore's inner surface of polycarbonate track-etched membranes," *RSC Adv.*, vol. 10, no. 59, pp. 35 930–35 940, 2020. DOI: 10.1039/D0RA05322H.

[167] A. Falciatore, M. Jaubert, J.-P. Bouly, B. Bailleul, and T. Mock, "Diatom Molecular Research Comes of Age: Model Species for Studying Phytoplankton Biology and Diversity," *Plant Cell*, vol. 32, no. 3, pp. 547–572, 2020. DOI: 10.1105/tpc.19.00158.

[168] S. Fan and J. D. Joannopoulos, "Analysis of guided resonances in photonic crystal slabs," *Phys. Rev. B*, vol. 65, no. 23, p. 235 112, 2002. DOI: 10.1103/PhysRevB.65.235112.

[169] V. I. Krivenkov, "Guided modes in photonic crystal fibers," *Dokl. Phys.*, vol. 48, no. 8, pp. 414–417, 2003. DOI: 10.1134/1.1606754.

[170] T. Fuhrmann, S. Landwehr, M. El Rharbi-Kucki, and M. Sumper, "Diatoms as living photonic crystals," *Appl. Phys. B*, vol. 78, no. 3-4, pp. 257–260, 2004. DOI: 10.1007/s00340-004-1419-4.

[171] J. Romann, J.-C. Valmalette, M. S. Chauton, G. Tranell, M.-A. Einarsrud, and O. Vadstein, "Wavelength and orientation dependent capture of light by diatom frustule nanostructures.," *Sci. Rep.*, vol. 5, no. 1, p. 17 403, 2015. DOI: 10.1038/srep17403.

[172] E. De Tommasi, "Light Manipulation by Single Cells: The Case of Diatoms," *J. Spectrosc.*, vol. 2016, pp. 1–13, 2016. DOI: 10.1155/2016/2490128.

[173] J. W. Goessling, W. P. Wardley, and M. Lopez-Garcia, "Highly Reproducible, Bio-Based Slab Photonic Crystals Grown by Diatoms," *Adv. Sci.*, vol. 7, no. 10, p. 1 903 726, 2020. DOI: 10.1002/advs.201903726.

[174] J. W. Goessling, A. A. Santiago González, V. S. Paul Raj, M. P. Ashworth, S. R. Manning, and M. Lopez-Garcia, "Biosilica slab photonic crystals as an alternative to cleanroom nanofabrication?" *Faraday Discuss.*, vol. 223, no. 0, pp. 261–277, 2020. DOI: 10.1039/D0FD00031K.

[175] S. R. Cicco, D. Vona, G. Leone, E. De Giglio, M. A. Bonifacio, S. Cometa, S. Fiore, F. Palumbo, R. Ragni, and G. M. Farinola, "In vivo functionalization of diatom biosilica with sodium alendronate as osteoactive material," *Mater. Sci. Eng. C*, vol. 104, p. 109 897, 2019. DOI: 10.1016/j.msec.2019.109897.

[176] J. Delasoie, P. Schiel, S. Vojnovic, J. Nikodinovic-Runic, and F. Zobi, "Photoactivatable Surface-Functionalized Diatom Microalgae for Colorectal Cancer Targeted Delivery and Enhanced Cytotoxicity of Anticancer Complexes," *Pharmaceutics*, vol. 12, no. 5, p. 480, 2020. DOI: 10.3390/pharmaceutics12050480.

[177] Y. Lang, F. del Monte, L. Collins, B. J. Rodriguez, K. Thompson, P. Dockery, D. P. Finn, and A. Pandit, "Functionalization of the living diatom Thalassiosira weissflogii with thiol moieties.," *Nat. Commun.*, vol. 4, p. 2683, 2013. DOI: 10.1038/ncomms3683.

[178] F. Ren, J. Campbell, X. Wang, G. L. Rorrer, and A. X. Wang, "Enhancing surface plasmon resonances of metallic nanoparticles by diatom biosilica," *Opt. Express*, vol. 21, no. 13, p. 15 308, 2013. DOI: 10.1364/OE.21.015308.

[179] A. Amoda, L. Borkiewicz, A. Rivero-Müller, and P. Alam, "Sintered nanoporous biosilica diatom frustules as high efficiency cell-growth and bone-mineralisation platforms," *Mater. Today Commun.*, vol. 24, p. 100 923, 2020. DOI: 10.1016/j.mtcomm.2020.100923.

[180] I. Rea and L. De Stefano, "Recent Advances on Diatom-Based Biosensors," *Sensors*, vol. 19, no. 23, p. 5208, 2019. DOI: 10.3390/s19235208.

[181] A. Kamińska, M. Sprynskyy, K. Winkler, and T. Szymborski, "Ultrasensitive SERS immunoassay based on diatom biosilica for detection of interleukins in blood plasma," *Anal. Bioanal. Chem.*, vol. 409, no. 27, pp. 6337–6347, 2017. DOI: 10.1007/s00216-017-0566-5.

[182] K. J. Squire, Y. Zhao, A. Tan, K. Sivashanmugan, J. A. Kraai, G. L. Rorrer, and A. X. Wang, "Photonic crystal-enhanced fluorescence imaging immunoassay for cardiovascular disease biomarker screening with machine learning analysis," *Sensors Actuators B Chem.*, vol. 290, pp. 118–124, 2019. DOI: 10.1016/j.snb.2019.03.102.

[183] M. Qiu, "Effective index method for heterostructure-slab-waveguide-based two-dimensional photonic crystals," *Appl. Phys. Lett.*, vol. 81, no. 7, pp. 1163–1165, 2002. DOI: 10.1063/1.1500774.

[184] R. R. L. Guillard and P. E. Hargraves, "Stichochrysis immobilis is a diatom, not a chrysophyte," *Phycologia*, vol. 32, no. 3, pp. 234–236, 1993. DOI: 10.2216/i0031-8884-32-3-234.1.

[185] H.-P. Boehm, "The Chemistry of Silica. Solubility, Polymerization, Colloid and Surface Properties, and Biochemistry. VonR. K. Iler. John Wiley and Sons, Chichester 1979. XXIV, 886 S., geb. £ 39.50," *Angew. Chemie*, vol. 92, no. 4, pp. 328–328, 1980. DOI: 10.1002/ange.19800920433.

[186] R. E. Hecky, K. Mopper, P. Kilham, and E. T. Degens, "The amino acid and sugar composition of diatom cell-walls," *Mar. Biol.*, vol. 19, no. 4, pp. 323–331, 1973. DOI: 10.1007/BF00348902.

[187] P. Chodanowski and S. Stoll, "Polyelectrolyte adsorption on charged particles: Ionic concentration and particle size effects—A Monte Carlo approach," *J. Chem. Phys.*, vol. 115, no. 10, pp. 4951–4960, 2001. DOI: 10.1063/1.1392357.

[188] L. Lu, W. Yi, and D. L. Zhang, "3ω method for specific heat and thermal conductivity measurements," *Rev. Sci. Instrum.*, vol. 72, no. 7, pp. 2996–3003, 2001. DOI: 10.1063/1.1378340. arXiv: 0202038 [quant-ph].

[189] S. K. Chamoli, S. C. Singh, and C. Guo, "Design of Extremely Sensitive Refractive Index Sensors in Infrared for Blood Glucose Detection," *IEEE Sens. J.*, vol. 20, no. 9, pp. 4628–4634, 2020. DOI: 10.1109/JSEN.2020.2964715.

[190] L. Hasanah, H. S. Nugroho, C. Wulandari, B. Mulyanti, D. D. Berhanuddin, M. H. Haron, P. S. Menon, A. R. Md Zain, I. Hamidah, K. Khairurrijal, and R. Mamat, "Enhanced Sensitivity of Microring Resonator-Based Sensors Using the Finite Difference Time Domain Method to Detect Glucose Levels for Diabetes Monitoring," *Appl. Sci.*, vol. 10, no. 12, p. 4191, 2020. DOI: 10.3390/app10124191.

[191] R. R. Singh, S. Kumari, A. Gautam, and V. Priye, "Glucose Sensing Using Slot Waveguide-Based SOI Ring Resonator," *IEEE J. Sel. Top. Quantum Electron.*, vol. 25, no. 1, pp. 1–8, 2019. DOI: 10.1109/JSTQE.2018.2879022.

[192] M. Terracciano, L. De Stefano, and I. Rea, "Diatoms Green Nanotechnology for Biosilica-Based Drug Delivery Systems," *Pharmaceutics*, vol. 10, no. 4, p. 242, 2018. DOI: 10.3390/pharmaceutics10040242.

[193] V. Onesto, M. Villani, M. L. Coluccio, R. Majewska, A. Alabastri, E. Battista, A. Schirato, D. Calestani, N. Coppedé, M. Cesarelli, F. Amato, E. Di Fabrizio, and F. Gentile, "Silica diatom shells tailored with Au nanoparticles enable sensitive analysis of molecules for biological, safety and environment applications," *Nanoscale Res. Lett.*, vol. 13, no. 1, p. 94, 2018. DOI: 10.1186/s11671-018-2507-4.

[194] J. Ouwehand, E. Van Eynde, E. De Canck, S. Lenaerts, A. Verberckmoes, and P. Van Der Voort, "Titania-functionalized diatom frustules as photocatalyst for indoor air purification," *Appl. Catal. B Environ.*, vol. 226, pp. 303–310, 2018. DOI: 10.1016/j.apcatb.2017.12.063.

[195] Y. Lang, F. D. Monte, B. J. Rodriguez, P. Dockery, D. P. Finn, and A. Pandit, "Integration of TiO2 into the diatom Thalassiosira weissflogii during frustule synthesis," *Sci. Rep.*, vol. 3, no. 1, p. 3205, 2013. DOI: 10.1038/srep03205.

[196] S. Mariani, V. Robbiano, L. M. Strambini, A. Debrassi, G. Egri, L. Dähne, and G. Barillaro, "Layer-by-layer biofunctionalization of nanostructured porous silicon for high-sensitivity and high-selectivity label-free affinity biosensing," *Nat. Commun.*, vol. 9, no. 1, p. 5256, 2018. DOI: 10.1038/s41467-018-07723-8.

[197] C. Sharma and N. K. Bhardwaj, "Bacterial nanocellulose: Present status, biomedical applications and future perspectives," *Mater. Sci. Eng. C*, vol. 104, p. 109 963, 2019. DOI: 10.1016/j.msec.2019.109963.